2015

Nuclear Structure of 26Si and 32Cl for Astrophysics

Liudmyla Afanasieva
Louisiana State University and Agricultural and Mechanical College

NUCLEAR STRUCTURE OF ^{26}SI AND ^{32}CL FOR ASTROPHYSICS

A Dissertation

Submitted to the Graduate Faculty of the
Louisiana State University and
Agricultural and Mechanical College
in partial fulfillment of the
requirements for the degree of
Doctor of Philosophy

in

The Department of Physics and Astronomy

by
Liudmyla Afanasieva
B.S., Kharkiv National University, 2009
M.S., Louisiana State University, 2014
May 2016

ACKNOWLEDGEMENTS

I would like to thank my graduate advisor Dr. Jeffery Blackmon and all our collaborators at Louisiana State University, Argonne National Laboratory, and Florida State University for help and support in research that was done as a part of my Ph.D. work.

TABLE OF CONTENTS

ABSTRACT

We studied the nuclear structure of two isotopes, ^{26}Si and ^{32}Cl, important for understanding stellar explosions like novae and Type I X-ray bursts. The ^{31}S(p, γ)^{32}Cl reaction rate influences the enrichment of sulfur observed in some nova ejecta, but the uncertainty in the rate spans as much as an order of magnitude and arises from uncertainties in the properties of resonances corresponding to excited states in ^{32}Cl.

We populated states in ^{32}Cl via the ^{10}B(^{24}Mg,2n)^{32}Cl reaction using the Argonne Tandem-Linac Accelerator System (ATLAS), with a 75 MeV beam of ^{24}Mg bombarding a 200 μ g/cm^2 ^{10}B target. Gamma rays emitted from recoiling heavy nuclei were detected by Gammasphere, and the Argonne Fragment Mass Analyzer (FMA) was used to separate heavy ions. We built the level scheme for ^{32}Cl from gamma-gamma coincidences, determining energies for 6 states, including 2 levels at E_x = 1738.1 (6) and 2130.5 (10) keV that correspond to the most important resonances in the ^{31}S(p, γ)^{32}Cl reaction at E_{cm} = 156.3(7) and 549.9(8) keV. With the resonance energies established, the single uncertainty dominating the ^{31}S(p, γ)^{32}Cl reaction rate is the strength of the 549.9 keV resonance.

The ^{22}Mg(α ,p)^{25}Al reaction plays an important role in type I X-ray bursts. We studied the structure of states in ^{26}Si corresponding to potential resonances in the ^{22}Mg(α ,p)^{25}Al reaction by measuring ^{25}Al+p elastic scattering at the John D. Fox Superconducting Accelerator Laboratory at Florida State University. A secondary ^{25}Al radioactive ion beam at 102.5 MeV bombarded a 2.05 mg/cm^2 polypropylene target. Scattered protons were detected using an array of silicon strip detectors, and the heavy ions were detected in a gas ionization chamber.

The center-of-mass energy for each event was reconstructed from the measured energy and angle of the protons, and the differential cross section for ^{25}Al+p scattering was determined

for center of mass energies of 2.7-4.0 MeV. We observe one strong s-wave resonance at a resonance energy of about 2.8 MeV, below the alpha particle threshold in ^{26}Si. While no strong resonances are conclusively observed at higher energies, there may be indications for weaker resonances in the excitation energy range between 8.5-9.5 MeV.

CHAPTER 1. INTRODUCTION

Stellar explosions like novae and supernovae eject ashes into the interstellar medium that later can serve as building blocks to form new stars, planets, and life. However, relatively little is known about rare events like stellar explosions, their nucleosynthesis, and how the products of their activities enrich the interstellar medium and affect the conditions leading to the creation of new stars and planets. Understanding Galactic nucleosynthesis would do much to help us understand the evolution and the fate of the Universe, and the clarification of these matters is one of the most compelling questions. Indeed, a National Academy of Sciences study concluded that this is one of the main goals of fundamental physics for the next decade [Bla11]. Due to the nature of the problems it is now clear that fundamental questions of life and matter will be answered in part by nuclear astrophysicists.

Stars contain giant thermonuclear reactors in their cores powered by nuclear fusion, and these nuclear reactions generate the tremendous energy in our Sun and other stars that results in their luminosity. Nuclear reactions are also responsible for the synthesis of the elements in our Galaxy and beyond. Thermonuclear reactions involving hydrogen and helium create heavier elements, with carbon, oxygen, and iron being the most ubiquitous. Our Sun and other similar low-mass stars evolve slowly due to the relatively low pressures and temperatures that result in a small rate for nuclear reactions, and the stars burn consistently and undisrupted for billions of years. Stars having a mass of about few times that of our Sun fuse the hydrogen and helium in their cores to form carbon, oxygen and in some cases neon, and expel their outer envelopes and cool slowly to end as white dwarfs, compact dense stars composed of C, O, Ne, supported by the degeneracy of electrons. White dwarfs usually have a diameter of a planet and a mass of about 0.6-1.4 solar masses.

Most stars in our Galaxy occur in binary systems, including systems composed of a still active main sequence star and compact companion such as a white dwarf or a neutron star. Such binary systems are gravitationally bound together, and some follow orbits coming so closely at times that their gravitational interaction can result in the transfer of matter from the larger main sequence star onto the surface of its smaller companion. As the fresh hydrogen-rich fuel accretes onto the surface of the white dwarf or a neutron star and is compressed, nuclear reactions occur that generate energy. Since the pressure is provided by electron degeneracy and is largely independent of temperature, the energy from nuclear reactions increases the temperature, which in turn accelerates the rate of nuclear reactions that have an exponential dependence on the temperature. The result is a thermonuclear runaway, and a violent explosion results.

For a typical white dwarf, with a mass no more than a bit larger 1.4 solar masses, the luminosity can increase as much as a million times, and we call these events nova explosions. Interacting binary systems that result in novae explosions are the most common type of interacting binary in the Milky Way Galaxy that undergoes cataclysmic explosions [Par14]. A much rarer event occurs when the explosion is so violent that the white dwarf is destroyed completely, and a Type Ia supernovae results. The exact progenitor of Type Ia supernovae and their connection to novae is still an open question.

Novae are likely the simplest stellar explosions in binary systems. Nova outbursts have been observed for more than twenty centuries due to their intense light output, producing tremendous energy only surpassed by supernovae and γ ray bursts [Jos06]. Typically, more than thirty events of this type are observed in the Milky Way each year (the second, most frequent type of thermonuclear explosion in the Galaxy after X-ray bursts) [Par14], although many more explosions likely occur but are not detected from space or ground-based observatories because

they are obscured by interstellar dust. The classical novae explosions are expected to recur with periodicity of 10^4-10^5 years [War95]. Yet, so far astrophysical models do not accurately predict the energy produced in novae or the mass ejected in the explosions.

The temperatures achieved during nova outbursts, with Tpeak $\sim (2-3) \times 10^8$ K, are high enough to induce chains of nuclear reactions in the material present in the envelope, suggesting that intermediate-mass isotopes can be potentially produced in these explosions. This raises the question about the probable contribution of novae to the Galactic abundances, which can be roughly evaluated as the product of the following parameters: the number of novae in the Galaxy, the average mass ejected in each nova outburst, and the Galaxy's lifetime. Current observations and theoretical models assume that novae scarcely contribute to the Galaxy's overall metallicity (as compared with other major sources), although they may produce significant amounts of certain nuclear species and inject them into the interstellar medium, particularly ^{13}C, ^{15}N and ^{17}O, with a possible significant contribution to other species, such as ^{7}Li, ^{19}F, or ^{26}Al [Geh98]. An improved understanding of the yields of isotopes from numerical models of novae with Galactic chemical evolution models incorporating binary star systems that take into account the distribution of white dwarf masses in binaries leading to novae and the evolution of the nova rate during the Galaxy's history is needed to understand the contribution of novae to the isotopes in our Galaxy.

In nova explosions, convection (that appears already at the early stages of the thermonuclear runaway, when T $\sim 2.5 \times 10^7$ K, and progressively extends throughout the whole envelope) carries significant amounts of some short-lived species (i.e., ^{13}N, ^{14}O, ^{15}O, ^{17}F) previously synthesized at the base of the envelope away towards its outer, cooler layers, where the temperature is too low to allow proton-capture reactions. These short-lived species decay in

about few minutes and release large amounts of energy that ultimately power the ejection of a significant fraction of the envelope.

Classical nova outbursts on (low-mass) CO white dwarfs are less energetic than novae exploding on ONe white dwarfs. Nuclear reactions on CO white dwarfs do not extend beyond oxygen, while ONe novae can produce elements as heavy as silicon (on ~1.15 solar masses white dwarf) or even perhaps as heavy as Ca on the most massive white dwarfs (m ~1.35 solar masses). Therefore, one may speculate that the presence of significant amounts of intermediate-mass nuclei in the spectra, such as phosphorus, sulfur, chlorine or argon, can potentially reveal the presence of an underlying massive (ONe) white dwarf available for further study [Iyu10].

Our understanding of novae has improved thanks to detailed observations and recording of the nova light curves and spectra, and multidimensional hydrodynamic models. The nuclei generated in novae are believed to produce proton-rich isotopes with $A < 40$, that is, below calcium. Nuclear processing occurring in the region between Si and Ca is primarily driven by leakage from the NeNa-MgAl region, where the main activity enfolds during the initial phases of the thermonuclear runaway. The main reaction that allows the heavier species to be produced (i.e., beyond P) is $^{30}P(p,\gamma)^{31}S$, after which either $^{31}S(p,\gamma)^{32}Cl(\beta+)^{32}S$, or $^{31}S(\beta+)^{31}P(p,\gamma)^{32}S$ follow [Jos05]. Therefore, study of the uncertainty of $^{30}P(p,\gamma)$ reaction for the temperatures of novae explosions is quite important as there are larger uncertainties in the rate due to unknown properties of resonances.

It is speculated that a subclass of novae are progenitors of Type Ia supernovae, the most violent explosions in the visible space. Understanding novae is a first step towards understanding Type Ia supernovae that are a dominant contributor to elements in the region of the periodic table near iron. Taking all this into account, it becomes clear that more experimental data shedding

light onto nuclear reactions other than ^{30}P(p,γ) that happen in novae explosions are sorely needed.

Unlike novae, X-ray bursts have been discovered only recently. Though similar in nature, X-ray bursts output a major fraction of their energy in form of X-rays that are absorbed in the Earth's atmosphere and can only be observed from space. In these systems, a main sequence star is bound to a neutron star, that is commonly formed in a Type II supernovae, but can also result from a so-called "accretion induced collapse" of a white dwarf. Neutron stars are even more compact objects than the white dwarfs, with diameters of about 20-30 km and masses of no more than about two solar masses. Like in a nova explosion, the X-ray burst is powered by a thermonuclear runaway ignited by fresh fuel being accreted from a main sequence star onto a degenerate companion star. After the explosion the system returns to the equilibrium state until the next explosion occurs. Thus, the process in such systems unfolds in cycles [Wre14]. While there are less than 200 systems that undergo X-ray bursts known, the explosions recur with periodicity typically of several hours to several days. With a neutron star as the underlying compact object where the explosion takes place, temperatures and densities in the accreted envelope reach at least an order of magnitude greater than in a typical nova outburst. As a result, because these processes power the bursts, detailed nucleosynthesis studies require the use of hundreds of isotopes (up to the SnSbTe cycle [Sch01]) and thousands of nuclear reactions. The main reaction flow moves far away from the valley of stability, and even merges with the proton drip-line beyond A=38 [Sch99]. A large simulation with a complete nuclear reaction network (up to 1300 isotopes) has been recently performed [Woo04]. Contrary to nova outbursts, convection has been shown not to play a critical role in the progress of the thermonuclear runaway in X-ray burst models [Jos06].

Novae, X-ray bursts and Type Ia supernovae are all thermonuclear explosions. A tremendous amount of energy is released in each of them: 10^{39} erg for a typical X-ray bursts, 10^{45} erg for classical novae, and 10^{51} erg for Type Ta supernovae. While in a Type Ta supernovae event the material of the whole companion star is ejected, in novae and X-ray bursts the explosion only involves the accreted envelope of the degenerate star. In the novae the envelope of the star is ejected, while in an X-ray burst it isn't. To understand the underlying nuclear physics that drives these explosions, studies of nuclear processes in stars are needed using particle accelerators and ion beams interacting with target nuclei. Often the elements created in stellar explosions are unstable, and some are found far from the valley of stability. Thus, the quest for greater understanding of the properties of nuclear reaction chains powering stellar explosions calls for studying short-lived radioactive nuclei.

The problem with such isotopes, of course, is that they don't exist on Earth as a common material since such "exotic" nuclei are unstable, so as the first step such material has to be produced using sophisticated experimental techniques. The production rate for the exotic nuclei in an accelerator is usually lower than those for the stable ones, and the cross sections of the reactions of interest are small, therefore, the statistics of the experiment can be fairly limited. Also, the more "exotic" these nuclei are, the shorter their half-lives. Therefore, not only do the nuclei have to be produced right during the experiment, the desired measurement must be performed with these radioactive ions before they decay, necessitating that the created radioactive nuclei be used immediately. In addition to this, if one wants to directly study astrophysically important reactions, the energies of the beams used in the experiment should be quite low to adequately reflect the processes naturally occurring in many stars, even in the most extreme stellar explosions. And even in cases when the radioactive species of interest are

produced in sufficient amounts using intense beams in the favorable energy range, the experimenter faces another obstacle: in the subsequent data analysis it is important to select only the reacted nuclei of interest. Therefore, experimental methods are needed to distinguish the desired reaction channels from the background. This problem is often compounded in measurements with radioactive beams since the beam may contain stable contaminants that can be even more intense than the isotope of interest. Therefore, cleanly selecting channels of interest is of essence. This is commonly done in hardware, applying detectors and electronics in various configurations, and in data analysis software, where the contaminants can be eliminated by selecting specific particles based on the understanding of their properties and behavior. These challenges are being constantly addressed by experimenters at dedicated laboratories facilities throughout the world.

This specific work in this thesis comprises measurements of the structure of two short-lived isotopes that are important for understanding thermonuclear stellar explosions. An experiment at Argonne National Laboratory (ANL) studied the structure of ^{32}Cl that is important for the ^{31}S(p,γ)^{32}Cl reaction, which plays a significant role in nova explosions. An experiment at the John D. Fox Superconducting Accelerator Laboratory at Florida State University studied the states in a compound nucleus ^{26}Si that are important for understanding the ^{22}Mg(α,p)^{25}Al reaction that is important for energy production in X-ray bursts.

CHAPTER 2. ^{32}CL MOTIVATION

The $^{31}S(p,\gamma)^{32}Cl$ reaction provides the dominant break-out path from the SiP cycle in classical novae and is important for understanding enrichments of sulfur observed in some nova ejecta. The time scales of novae are influenced by the duration of reaction cycles closed by (p,α) reactions, with break out via (p,γ) reactions competing with β-decays, see Figure 2.1. The SiP cycle is one such cycle, which is of particular interest for understanding novae such as Nova Her 1991 that are observed to exhibit high sulfur abundances [Wil 94, Mat93].

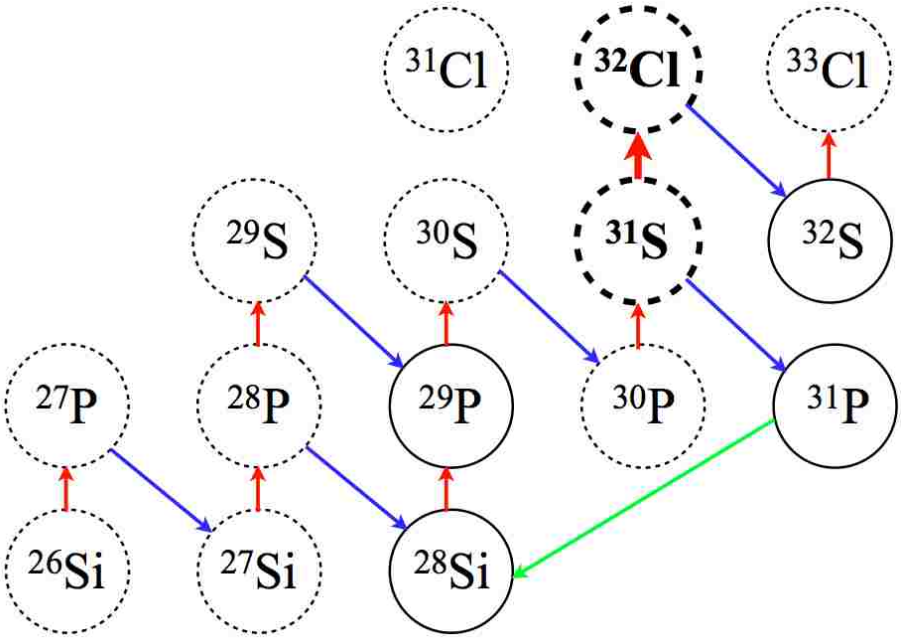

Figure 2.1. A portion of the Chart of Nuclides around ^{31}S showing the SiP cycle [Mat11b].

The uncertainty in the $^{31}S(p,\gamma)^{32}Cl$ reaction rate spans as much as an order of magnitude and arises from uncertainties in the properties of resonances (resonance energies and resonance strengths) corresponding to excited states in ^{32}Cl just above the proton threshold. [Jea89] In particular, the rate of the $^{31}S(p,\gamma)^{32}Cl$ reaction at nova temperatures is expected to be dominated

by 3 low energy resonances at E_{cm} = 157, 549 and 628 keV, corresponding to states in the compound nucleus ^{32}Cl at E_x = 1738, 2131 and 2209 keV, respectively. Although, another resonance corresponding to a state at 2283 keV could contribute at the highest nova temperatures and could be important depending on the uncertain resonance properties.

Information on the resonance states in ^{32}Cl of interest for astrophysics comes almost exclusively from the ^{32}S(^{3}He,t)^{32}Cl reaction, which is one of the strongest direct reaction channels for producing ^{32}Cl with a stable beam and target. As a result, a number of experimental studies used the charge-exchange ^{32}S(^{3}He,t)^{32}Cl reaction in order to study levels of interest. However, there remain substantial uncertainties. For example, the two most precise recent measurements of this reaction differ by about 4 keV on average for the resonance energies [Mat11,Wre12].

One study of the ^{32}S(^{3}He,t)^{32}Cl reaction, done by Matos *et al.* [Mat11], populated ^{32}Cl levels and measured triton magnetic rigidities to determine excitation energies in ^{32}Cl. A 30-MeV ^{3}He^{2+} beam from the Extended Stretched TransUranium (ESTU) Tandem Van de Graaff accelerator at the Wright Nuclear Structure Laboratory (WNSL) at Yale University was used to bombard ZnS targets with thicknesses of 240 μg/cm^2 and 350 μg/cm^2 both on 5 μg/cm^2 carbon substrates. Data were also taken with a 300 μg/cm^2 Si target for calibration and a 900 μg/cm^2 Zn target for background subtraction.

Reaction products were separated using the Enge split-pole spectrograph at the WNSL set at scattering angles of 3°, 5°, 10° and 20°. The position of beam particles was measured at the focal plane of the spectrograph using a position-sensitive ionization drift chamber filled with 150 Torr of isobutane gas backed by plastic scintillator. Tritons were identified using relative energy

loss (ΔE vs. E) from the ionization chamber and the scintillator. Sample spectra showing the ^{32}Cl levels populated in this measurement are shown in Figure 2.2.

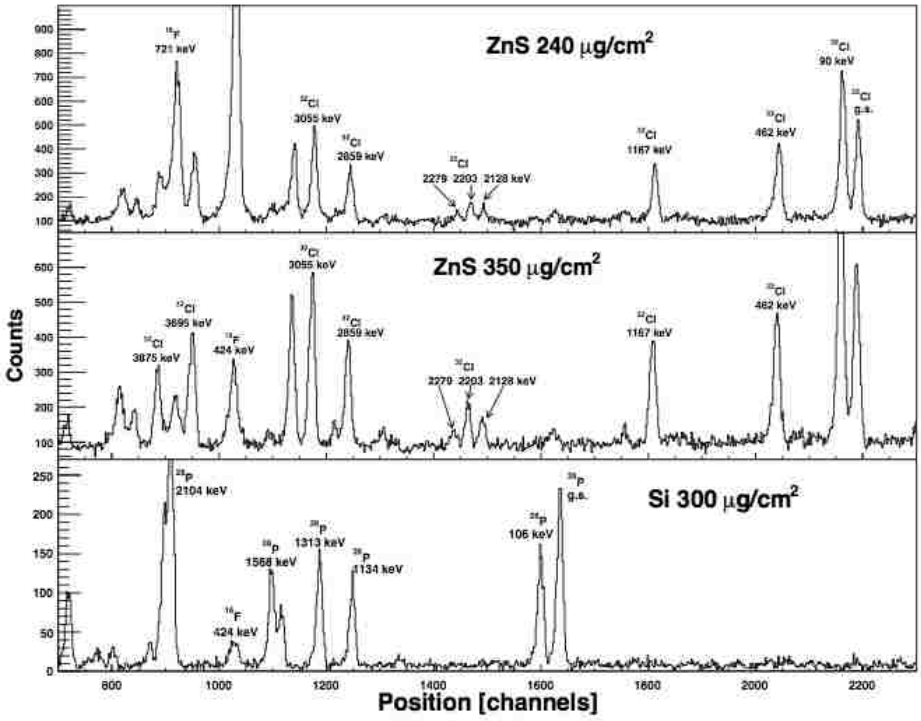

Figure 2.2. Triton position spectra from the ^{32}S(^{3}He,t)^{32}Cl reaction studied at the Wright Nuclear Structure Laboratory (WNSL) [Mat11]. The three spectra show measurements done with three different targets, 240 μ g/cm^2 ZnS, 350 μ g/cm^2 ZnS and a 300 μ g/cm^2 Si target.

A different study of the ^{32}S(^{3}He,t)^{32}Cl reaction performed at the Tandem accelerator laboratory in Munich used a 400-enA, 32-MeV ^{3}He^{2+} beam to bombard thin targets of ^{32}S [Wre10]. Tritons produced in the (^{3}He,*t*) reaction were momentum-analyzed using the Q3D magnetic spectrograph and detected at the focal plane of the spectrograph [Wir00, Fae09]. Data were collected with the spectrograph placed at 10° and 20° with respect to the incident beam. Peaks in the focal-plane position spectra corresponding to known levels in the nuclei ^{20}Na, ^{24}Al, ^{28}P and ^{36}K were used for momentum calibration of the focal plane of the separator for each of

the measurements at the corresponding angles. A single ^{32}Cl peak was then used together with the fits to determine the mass of ^{32}Cl. This procedure led to mass measurements of ^{20}Na, ^{24}Al, ^{28}P, and ^{32}Cl with precisions of 1.1 or 1.2 keV.

Excitation energies in ^{32}Cl were determined by fitting each triton peak with a Gaussian function. This work found that the ^{32}Cl excitation energies were in good agreement with the (^{3}He,*t*) measurements of Ref. [Vou94] and the (^{3}He,*t*) measurements of Ref. [Lef97]. The data obtained were systematically higher than the ones obtained in another (^{3}He,*t*) study [Jea89] by about 10 keV.

In yet another study [Wre12], the energy for one level in ^{32}Cl has been determined by high-resolution gamma-ray spectroscopy studies of ^{32}Ar β^{+} decay. States at higher excitation energies in ^{32}Cl are likely to decay predominantly by proton emission, so it may be difficult to measure them through gamma-ray emission. However, the γ-ray feeding of the level near 2.2 MeV was used to constrain its excitation energy instead. In this case the excitation energy in ^{32}Cl levels can be calculated by taking the difference between the precisely measured excitation energy of 5046.3(4) keV for the lowest T=2 level of the Cl nucleus and the 2836(1)-keV energy of the γ ray transition deexciting it, observed in ^{32}Ar-decay experiment. The same γ ray from a different experiment was measured to be 2838(1) keV. Subtracting these energies from the excitation energy of the T = 2 level gives us E = 2210.3(11) keV and E = 2208.3(11) keV. This value is in agreement with that of β-decay from Ref. [Bha08]. It was argued that these results may indicate a systematic error in the energies of Ref. [Mat11]. The excitation energies reported in [Mat11] were systematically low compared to [Wre12], which could result from the fact that the lowest excitation energies were strongly influenced by internal ^{32}Cl calibration points and

that the calibration gradually became more dependent on external calibration points towards higher energies.

However, the 2209-keV state corresponds to the only resonance in the $^{31}S(p,\gamma)^{32}Cl$ reaction to have its energy constrained directly via gamma-ray spectroscopy. The two most important resonances at lower energy have not yet been precisely constrained through gamma rays. The purpose of this experiment was to determine excitation energies for these states in ^{32}Cl nucleus with high precision through gamma-ray spectroscopy.

CHAPTER 3. ^{32}CL EXPERIMENT

The experimental approach we used closely followed one applied in several previous studies [Sew07, Lot 08] to study neutron-deficient nuclei. A heavy ion beam from the Argonne Tandem Linac Accelerator System (ATLAS) bombards a fixed target, and short-lived nuclei are produced by–fusion-evaporation reactions. This approach is particularly efficient for producing nuclei in highly-excited states. During a fusion-evaporation reaction, two nuclei (one of which is a projectile and the other one a target) are brought close to each other with energy sufficient to penetrate the Coulomb barrier of each nucleus. The two nuclei fuse, and a highly-excited compound system results. Production of neutron-deficient nuclei is favored since the reacting stable light nuclei have a lower N/Z ratio compared to the heavy stable nuclei. Furthermore, it is typically more energetically favorable for the excited system to release its excessive energy through the evaporation of nucleons and in particular neutrons, making the resulting nucleus even more neutron-deficient. Only once the excitation energy of the system is reduced to close to the particle threshold does the emission of gamma rays compete with the emission of particles.

In this particular case, a beam of ^{24}Mg from ATLAS at 75 MeV with a current of about 10 pnA bombarded a 200 μg/cm^2 ^{10}B target to produce states in ^{32}Cl via the ^{10}B(^{24}Mg,2n)^{32}Cl reaction channel, with only neutrons evaporating from the compound nucleus. Prompt γ rays emitted from excited states were detected by a highly-efficient germanium detector array, Gammasphere. The reaction channel of interest is tagged by separating residual heavy nuclei in the Argonne Fragment Mass Analyzer and detecting them at the focal plane using selective heavy ion detectors. The ^{32}Cl recoils were selected by the FMA in coincidence with the γ rays. Gammasphere is a 12-ton third-generation gamma-ray detector, see Figure 3.1, built to study the complex structure and behavior of nuclei by fusing lighter nuclei into heavier ones and observing

gamma rays emitted when the new nuclei decay. Gammasphere consists of a pair of six-foot-tall detector hemispheres covering nearly 4π. The detector design is a 122 element polyhedron of 110 hexagon and 12 pentagon faces [Bea96]. Each detector is a crystal of high-purity germanium ~ 72 mm diameter and ~ 84 mm long, the largest germanium crystal that are currently possible to produce commercially, and have relative efficiencies of ~ 78% [Bea96] that are measured in comparison with 3 inch by 3 inch NaI crystals. The most important properties of this gamma-ray detector array are: high efficiency in detecting incident gamma rays, high energy resolution, high ratio of full-energy to partial-energy events, and a capability to localize individual gamma rays and reduce the probability of two gamma-ray being detected in one detector simultaneously being recorded as coming from the same event.

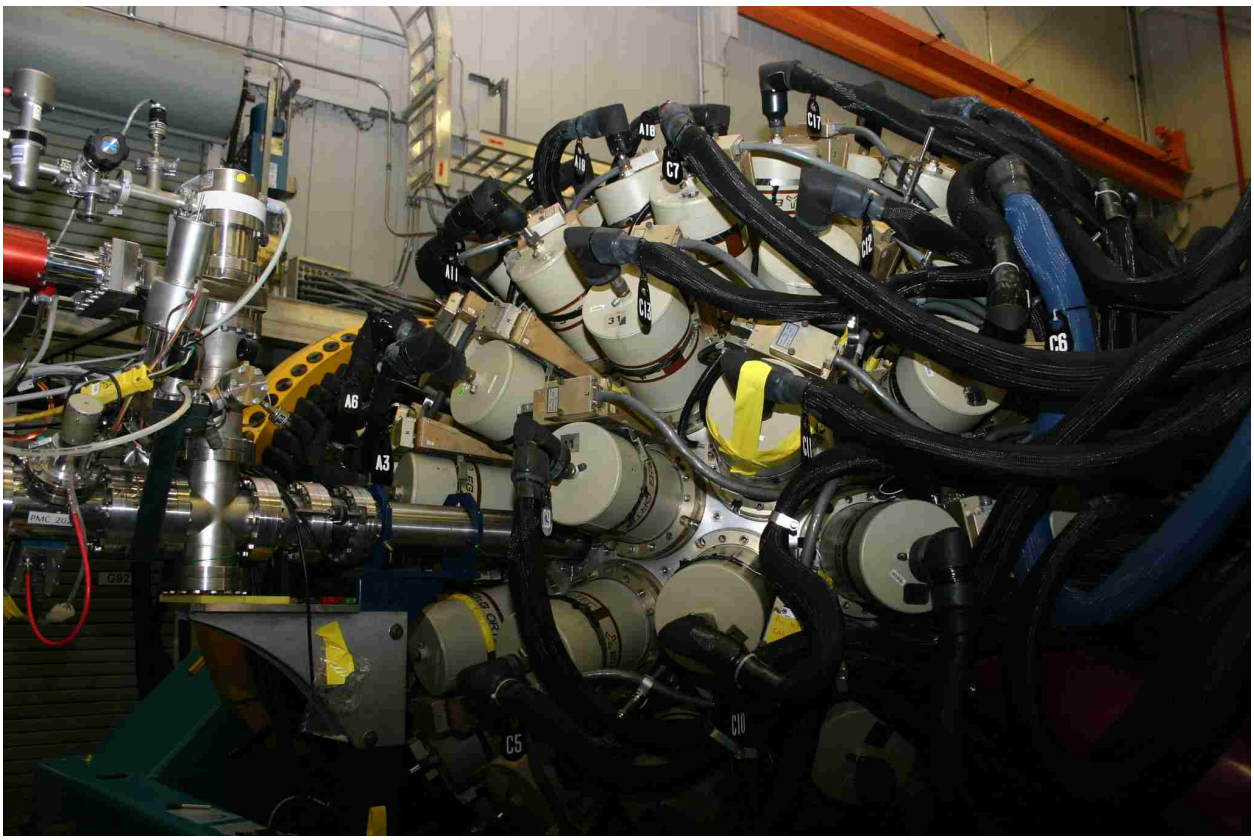

Figure 3.1. Gammasphere at the beamline, Argonne National Laboratory, United States.

When struck by gamma rays, energetic electrons from Compton scattering and the photoelectric effect produce significant ionization that is collected on a central anode and processed by electronics to create the signal proportional to the energy deposited. The sequence of pulses from the 100 detectors surrounding the target provides information about the gammas being emitted as nuclei fuse and cool. The detectors placed perpendicular to the beam axis and therefore most sensitive to the Doppler broadening of their signals are segmented. The assembled device for our experiment contained 98 germanium gamma-ray detectors all pointing at the Gammasphere's center, where new nuclei are created when the ATLAS beam strikes a target.

In order to detect all the energy deposited in an event of interest and to obtain a better ratio of total-energy events to partial-energy events (the so-called peak-to-total ratio), each of the Ge detectors are backed up by bismuth germanate (BGO) scintillator detectors that detect γ rays Compton-scattered out of the Ge detectors. When signals are observed in the BGO detectors in coincidence with the Ge detectors, the partial-energy traces left in the Ge detector are electronically suppressed. For a 1.3 MeV gamma ray this method gives an improvement of the peak-to-total ratio from about 0.25 for the bare crystal to about 0.6 when suppressed. It allows important events of interest to be distinguished in the case of high-coincidence rates and high background noise. To optimize the performance of the BGO detectors with the Ge detectors, an off-centre coupling is used between the Ge detector, the liquid nitrogen Dewar and pre-amplifier electronics [Bea96].

For our experiment, the Gammasphere was used in combination with the Fragment Mass Analyzer (FMA). The FMA is a triple-focusing recoil mass spectrometer, 8 m in length, which is used to separate nuclear reaction products from the primary heavy ion beam and disperses them by mass/charge ratio at its focal plane. The main ion-optical elements of the spectrometer are two

electric dipoles (ED1-ED2) and a magnetic dipole. The electric dipoles are symmetrically placed before and after the magnetic dipole (MD), see Figure 3.2. The elements are positioned in such a manner that the position-energy dispersion and the angle-energy dispersion of the beam get mutually compensated and cancel. Thus, different energies are focused to the same position. However, mass-to-charge dispersion remains, and the device functions as a mass spectrometer. Canceling of the energy dispersion can be achieved by other methods, for example, using Wien filters or a single electrostatic element with a magnetic dipole, but the combination of two electric dipoles and a magnetic dipole has some advantages over other configurations. In particular, wider mass-to-charge ratio acceptance and energy acceptance of the nuclei can be achieved, the rejection of the primary beam may be better with better resolution achieved.

Often additional devices such as quadrupole singlets or sextupoles are utilized in mass spectrometers as well in order to accomplish better geometric focusing and to provide second-order corrections. In the FMA, four additional quadrupoles are being used (Q1, Q2, Q3, and Q4), all the configuration of all elements being Q1-Q2-ED1-MD-ED2-Q3-Q4, see Figure 3.2[Dav05].

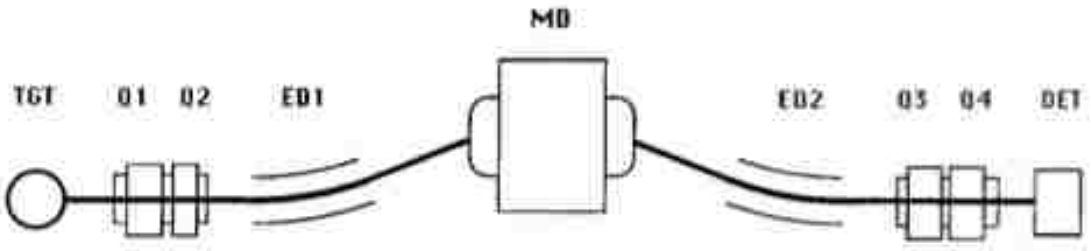

Figure 3.2. The outline of the Fragment Mass Analyzer, showing the electric and magnetic elements of the spectrometer, arranged in a symmetric configuration. TGT=target, DET=detector [Dav92].

The FMA has a solid angle acceptance of 8 msr, an energy acceptance of ±20% around the central energy, and a mass/charge acceptance of about 7% around the central mass. The settings of the electric and magnetic elements of the FMA were configured in this experiment so that only nuclei with M/Q ≈ 2.46 (e.g. A=32 and Q=13+) reached the focal plane through the mass slits.

A vast number of experiments can be potentially performed with the FMA, and other types of detectors are used at the FMA focal plane in order to improve particles detection and their separation from the background. Among the types of detectors used with the FMA are: a Parallel Grid Avalanche Counters (PGAC), see Figure 3.3, Standard Ion Chambers (IC), a Double-sided Silicon Strip Detectors (DSSD), Micro Channel Plates (MCPs) and Ion Chambers (IC). To improve the flexibility, many types and combinations of detectors can be used in

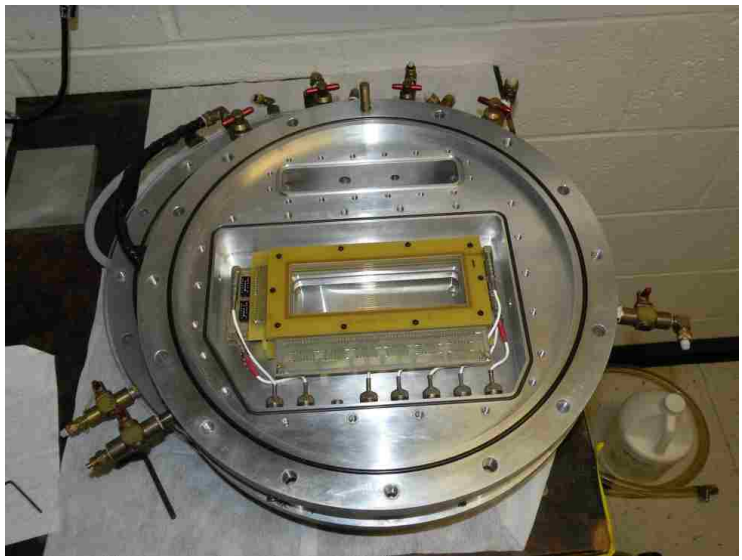

Figure 3.3. PGAC from private correspondence with Dr. Seweryniak.

conjunction with each other. Thus, modularity is important to achieve the goal of most experiments, which is to lower the minimum limit for the cross-section that is to be observed.

This information can improve the sensitivity for many FMA experiments by at least one order of magnitude.

In our experiments we used a PGAC and an IC. The merits of parallel-grids avalanche counters as transmission timing detectors have been well documented [Ste81] and include: good timing, tunable efficiency for discrimination purposes, high count rate capability, resistance to radiation damage and rugged construction [Fab83, Pre85]. The PGAC developed for the use with the FMA was produced by chemically milling sheets of 35 micrometers of copper.

The operating principles of avalanche counters can be found in the literature [Rae64] and are summarized as follows. PGACs are proportional counters with parallel electrode grids put into an ion chamber filled with a low pressure (typically 2-50 Torr) gas with good quenching properties, such as isobutane. Ionizing charged particles traversing the avalanche counter generate ions in the gas that are multiplied by electric field (typically about -400 V mm^{-1}) applied to the grids of the counter. A fast signal (t_{rise} <1.5 ns) is generated and may later be exploited for timing application, as does the pulse height information.

The PGAC described here was developed as a transmission start counter for use in a mass identification telescope to be employed at forward angles. [Smi90] It sits at the back of the FMA and is 5 cm tall and 15 cm wide. For our experiment the particles passed through the PGAC, and it provided information about their position, i.e. their x and y coordinates, as well as information about their energy.

The cathode voltage of the PGAC was set to about -200 Volts, which is a typical operating voltage for experiments with PGAC, and the anode voltage was about +350-400 Volts. The PGAC window in this measurement was Mylar with thickness of 0.8 microns. The PGAC was filled with isobutane and kept at 3 Torr. Distance between PGAC planes was 3.2 mm.

Positions of particles in the PGAC were derived from delay line readouts off the ends of the x wire plane (right and left position of the particle with respect to the beam direction) and the y plane (up and down positions). A time-to-digital converter (TDC) records the anode signal, which is a start, and stops are provided by the four right, left, up and down delay line signals. The x coordinate of the particle was obtained from right and left readouts and the y coordinate comes from the up and down signals. The position resolution of the PGAC is about 1.2 mm. Energy loss of ions passing through the PGAC was obtained using the cathode signal.

The horizontal delay line was 120 ns long, the maximum length of the x spectrum was 120 ns. at 0.1ns per channel, which is a standard setup for a PGAC TDC. With this we see a maximum range of 1200 channels, but the software compresses x by a factor of 4 and it is displayed over 512 channels. So the maximum range of the x spectrum is 300 channels. One sees all the channels with a source, but a smaller range is displayed with in-beam data as a result of the acceptance limitations of the FMA. The vertical delay line is 40 ns.

After passing through the PGAC, ions were stopped in the ionization chamber (IC) filled with isobutane at 13 Torr. The ion chamber (IC) adds high-resolution total and relative energy loss information about the ions crossing the focal plane of the FMA, information that can be critical in isolating rare events. The IC utilized in this experiment was divided into 3 segments (5, 5 and 20 cm long, respectively) to facilitate particle identification by relative energy loss *(*ΔE*)* and total energy *(E)* measurements. All three sections of the ΔE signals can be linked inside the vacuum chamber using jumpers between each of the ΔE signals.

CHAPTER 4. ^{32}CL RESULTS

Since the primary goal of this experiment was to extract precise energies for the states of interest, good energy calibration of the Gammasphere detectors was required. To achieve this, we collected spectra for each germanium detector using a series of standard gamma calibration sources (^{243}Am, ^{152}Eu, ^{182}Ta and ^{56}Co) located at the target position. One example of such a spectrum is shown in Figure 4.1. The peak areas and positions were extracted (and background subtracted) using the RadWare software package [RAD96]. From the well-known energies and intensities of these sources, the energy and relative efficiency as a function of gamma-ray energy was determined.

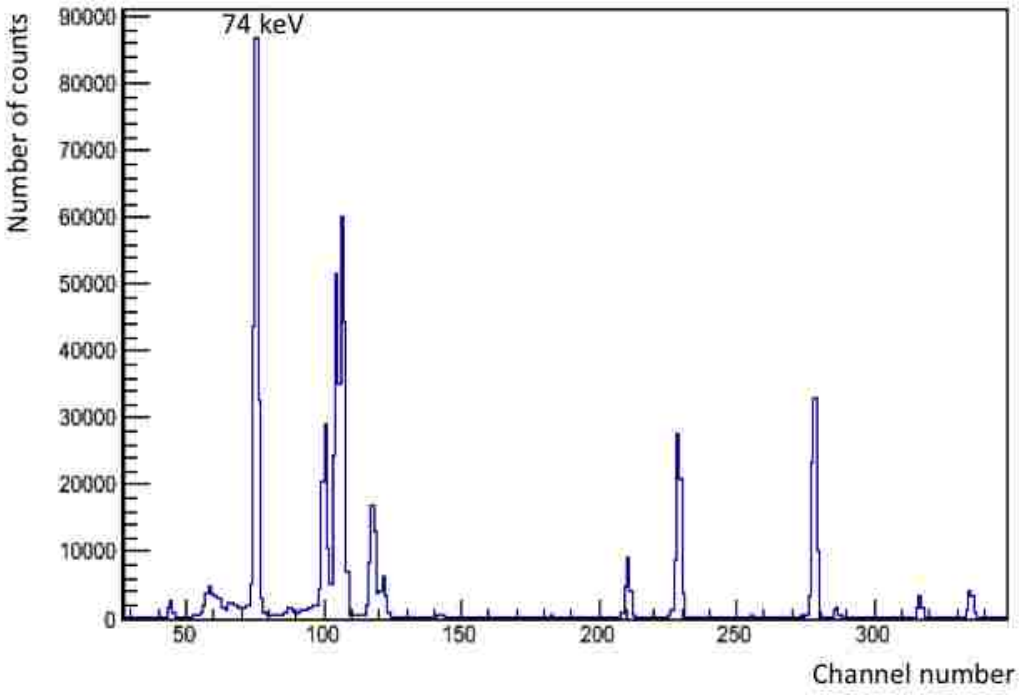

Figure 4.1. An ^{243}Am calibration spectrum for one of the Gammasphere detectors. The strongest peak in this isotope is 74 keV. It is fitted by the RadWare software to extract calibration information. The rest of the peaks are background lines.

In addition, to achieve good resolution, Doppler correction (with ion velocity of v/c = 0.0564 corresponding to the average velocity of ^{32}Cl recoils selected by the FMA) was applied to each detector based upon the angle of the detector. With these calibrations, the excitation energies for levels in ^{32}Cl could then determined to better than 1 keV accuracy (see below).

Mass 32 ions are selected by their position in the PGAC. Well-separated groups corresponding to Mg, Al, Si, P, S and Cl recoil ions were identified by the relative energy loss in the ionization chamber, as illustrated in Figure 4.2.

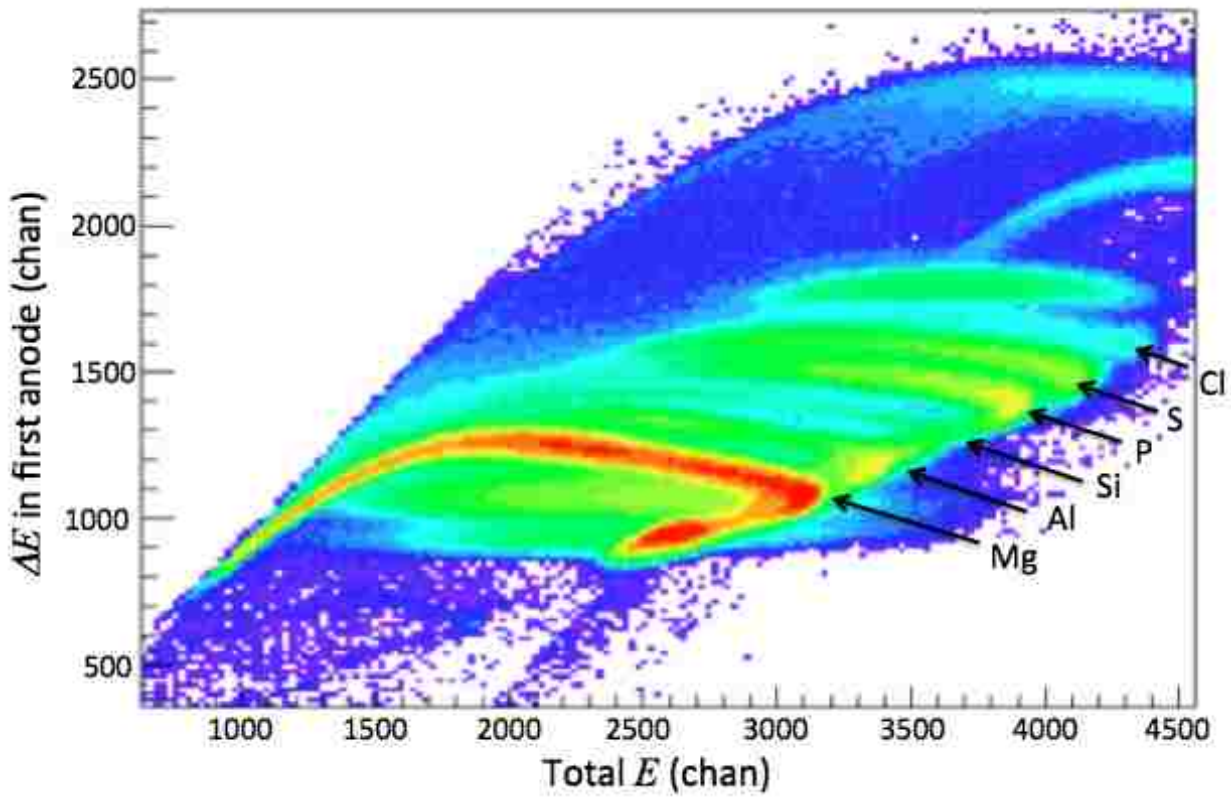

Figure 4.2. $\Delta E - E$ data from the ionization chamber. The chamber is segmented into three parts, for this experiment it was filled with isobutane at 13 Torr.

We gated on the group corresponding to Cl ions, aiming to study recoil-γ and recoil-γγ coincidences to determine the level structure of ^{32}Cl. The rest of the analysis concentrated on the nuclei selected within this Cl gate.

A ^{32}Cl 1D energy spectrum is shown in Figure 4.3. The spectrum was generated using RadWare software and shows a single γ-ray 1D ^{32}Cl spectrum within the FMA Cl gate, thus, contaminants from other isotopes in the spectrum are partially eliminated.

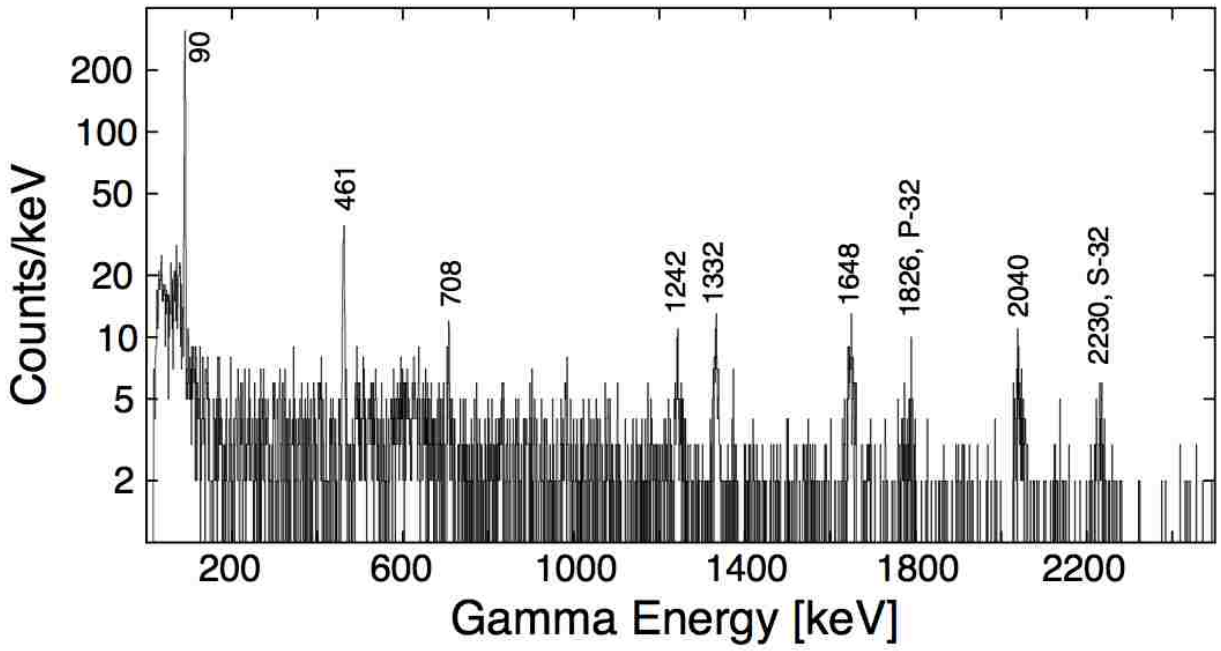

Figure 4.3. 1D gamma-ray energy spectrum of the ^{32}Cl nucleus.

As the next step of the data analysis, a γ−γ matrix was built, see Figure 4.4. This matrix makes use of gamma-gamma coincidences, and it is was built by plotting γ rays that are emitted in coincidence with other γ rays. With this method we can distinguish cascades of γ transitions going from one level of the nucleus to the next. Here we gate on the ~90 keV level since it's a transition from the first-excited state to the ground state in the ^{32}Cl nucleus, through which many

of the upper levels decay in a cascade. It is also the strongest transition observed in this experiment. We also attempted to gate on the other gamma transitions, but the statistics was too low to establish the coincidences reliably. Using the γ–γ matrix gated on the 90 keV level we built the ^{32}Cl levels decay scheme shown in Figure 4.5.

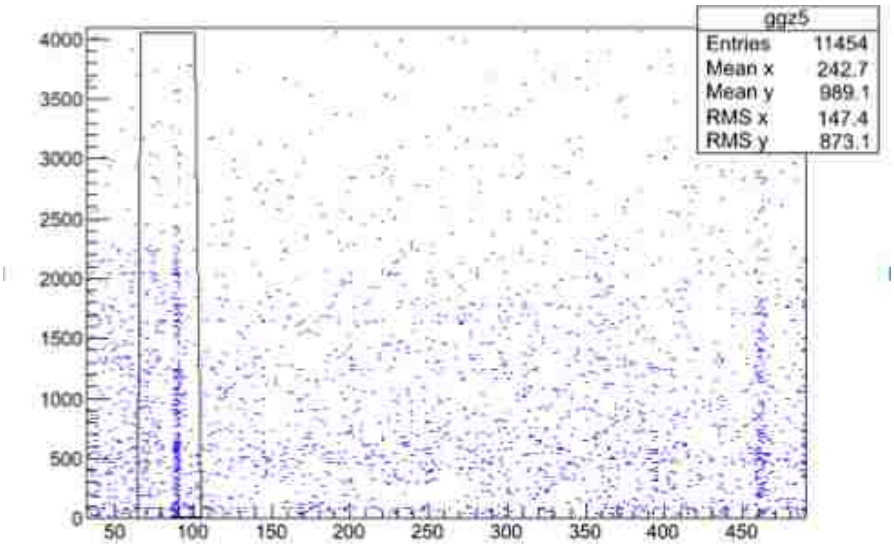

Figure 4.4. Gamma-gamma matrix showing gate around 89.6 keV level that higher levels predominantly decay through.

In addition, since the ion species aren't separated perfectly by the FMA, the contaminants from the neighboring species enter the Cl spectra. These contaminants were subtracted from the Cl spectra in ROOT in order to establish the contamination rate and the probable coincidences.

We were able to accurately determine energies for two of the most important resonances for the ^{31}S(p,γ)^{32}Cl reaction rate at 1738.1(6) keV and 2130.5(10) keV. The 1738.1(6) keV state was observed to decay to the 89.65(5) keV state, emitting a γ ray of 1648.5(7) keV. The 2130.5(10) keV state decays to the 89.65(5) keV state, emitting a 2040.9 (11) keV γ ray. Our result for the 1738 keV state was 1.4 keV higher than that of [Wre10] (slightly more than a 1σ

difference), but our results for the 2131 keV level are in good agreement. On the other hand, our results are about 4 keV higher than those of [Mat11b] for these two states of astrophysical interest, though we find good agreement for the lower energy bound states. We did not observe the 2209 keV or 2283 keV states in this measurement. While this may indicate a dominance of the proton decay branch over gamma decay, it could also result in part from weak feeding of these states in this particular reaction channel, so no firm conclusions about these states can be drawn from this measurement.

In addition to the unbound states of interest for astrophysics, we observe the decay of the 1168.8(7) keV state by emission of a 708.0(6) keV γ ray cascading through the 460.80(15) keV state. It should be noted that spin-parity assignments in ^{32}Cl are based largely on comparisons with the mirror nucleus ^{32}P, and the 1332.3(6) keV state in ^{32}Cl presumably corresponds to the 1322 keV 2+ state in ^{32}P. In ^{32}P this level decays both by direct decay to the ground state and through by a cascade of gamma rays through the first-excited 2+ state. Mirror symmetry suggests that a similar decay scheme should be observed for this state in ^{32}Cl, and indeed we observe the 1332.3 level of ^{32}Cl decaying both to the ground state and via a 1242.7(9) keV transition to the 89.65 keV state, which has not been observed previously. The relative intensity of decay to the first excited state relative to the ground state branch (1.0:1.5) is in excellent agreement with that observed in the mirror nucleus.

We precisely determined excitation energies through γ-ray spectroscopy for states corresponding to two resonances at 156 and 550 keV that dominate the ^{31}S(p,γ)^{32}Cl reaction rate for temperatures of interest for novae. In Table 4.1, we summarize values for important resonances. Energies of the 156-keV and 550-keV resonances are taken as a weighted average of those from this work and from [Wre10] using the proton separation energy of 1581.3(6) keV,

with uncertainties in the level energy and proton separation energy added in quadrature. Energies for the 628-keV and 702-keV resonances are taken from the previous work of [Wre10,Wre12].

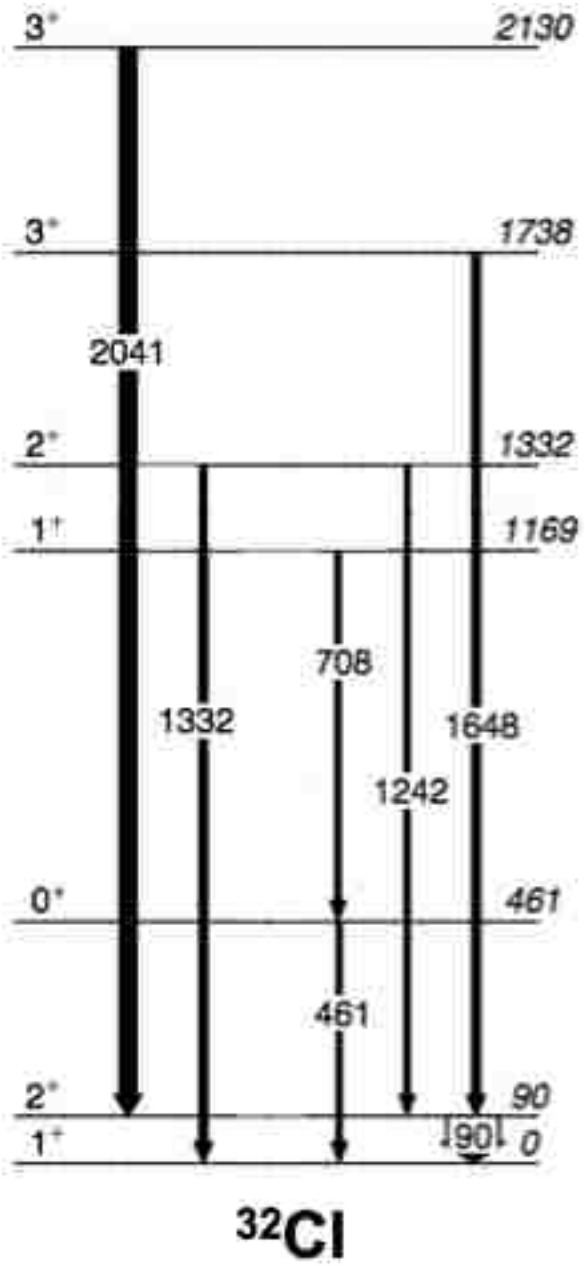

Figure 4.5. Energy level scheme in ^{32}Cl as measured in this experiment.

The $^{31}S(p,\gamma)^{32}Cl$ reaction rate is dominated by the contributions of these resonances. The resonant process only occurs if the energy of the entrance channel matches the energy E_R of the excited state in the compound nucleus. At nova temperatures, T ≈0.1–0.3 GK, the energies are relatively low, and the resonances are generally narrow and well separated. Cross-sections for such resonances are well described as a function of energy by Breit-Wigner approximation in the center of mass system:

$$\sigma(E)=\pi\lambda\!\!\!^{-2}\,\frac{2J+1}{(2J_1+1)(2J_2+1)}(1+\delta_{12})\frac{\Gamma_a\Gamma_b}{(E-E_R)^2+(\Gamma/2)^2},$$

Table 4.1. Previous results from $^{32}S(^3He,t)^{32}Cl$ reaction and from β-decay measurements with high resolution γ-spectroscopy are compared to the excitation energies determined in this measurement. Observed γ-ray energies and relative intensities are given. Most of the spin-parity assignments listed in the table are tentative.

[Mat11]	[Jea89]	[Vou94]	[Wre10]	[Wre12]	[this work]	E_γ[this work]	J^π	I
---	---	---	---	89.1 (1)	89.65 (5)	89.65 (5)	2^+	100 (4)
462 (1)	447 (7)	---	---	461.1 (1)	460.80 (14)	460.8 (1)	0^+	9 (1)
1167 (2)	1157 (5)	---	---	1168.55 (13)	1168.8 (6)	708.0 (5)	1^+	3 (1)
1327 (3)	1326 (5)	1329 (3)	1331.2 (5)	---	1332.3 (6)	1332.3 (6)	2^+	15 (2)
	---	---	---	---	---	1242.7 (9)		10 (1)
1734 (1)	1719 (4)	1735 (3)	1736.7 (6)	---	1738.1 (6)	1648.5 (6)	3^+	24 (3)
2127 (2)	2122 (5)	2129 (3)	2131.1 (4)	---	2130.5 (10)	2040.9 (10)	3^+	33 (3)
2203 (3)	2193 (7)	2213 (3)	2209.5 (5)	2209.3 (11)	---	---	1^+	---
2279 (3)	2270 (5)	2281 (3)	2283.5 (5)	---	---	---	2^+	---

$$\omega = \frac{2J+1}{(2J_1+1)(2J_2+1)}$$

is a statistical factor, where J is the angular momentum of the excited state in the compound nucleus, J_1 is the spin of the projectile, and J_2 is the spin of the target nucleus. The term $(1+\delta_{12})$shows that the cross-section of the reaction increases if the two interacting particles in the entrance channels are identical.

The total energy width of the excited state of the nucleus Γ is calculated as a sum of all energetically allowed decay channels of the nucleus. Such channels are called "open":

$$\Gamma = \Gamma_1 + \Gamma_2 + \cdots$$

The Breit-Wigner treatment is only allowed for the so-called "narrow" resonances, that is, when their total energy width Γ is small comparing to the energy difference between the levels in the excited nucleus. This is a valid assumption in this case, and we will use the Breit-Wigner formalism to evaluate the contributions of these resonances to the reaction rate.

Whether the energy level in a given nucleus can be formed or not, depends on the selection rules, i.e. on the angular momentum and parity conservation. The spins of the particles in the entrance channel (J_1,J_2 ...) and the relative orbital angular momentum l of the nucleus should sum up to the angular momentum J of the state we want to form:

$$J_1 + J_2 + l = J$$

As a result, the stellar reaction rate per particle per pair in presence of a narrow resonance can be written as:

$$\langle \sigma v \rangle = \left(\frac{2\pi}{\mu kT}\right)^{3/2} \hbar^2 (\omega\gamma) exp\left(-\frac{E_R}{kT}\right) f,$$

where T is the temperature in GK, E_R is the energy of resonance in the compound nucleus, μ is the reduced mass in atomic mass units, and $(\omega\gamma)$ is the resonance strength. Electronic screening

in stars is taken into account by introducing the screening factor f. For our experiment the total width consists of partial proton width and partial gamma width. The total reaction rate can be written as:

$$\langle \sigma v \rangle = \sqrt{\frac{8}{\pi\mu}} (kT)^{3/2} \int \sigma E \, exp\left(-\frac{E_R}{kT}\right) dE,$$

As there is no direct experimental information, γ-ray partial widths, Γ_γ, are based upon properties of mirror states in ^{32}P adjusted for the change in energies based upon typical energy scaling for transition strengths [Won98], and are the same as those presented in [Mat11b]. We assume that the transition probabilities are the same for both mirror nuclei. The gamma energy width of a state in the mirror nucleus can be calculated as a sum through all possible final state transitions:

$$\Gamma_\gamma\left(^{32}Cl\right) = \sum_i \frac{E_{\gamma i}^{(\lambda_i+2)}\left(^{32}Cl\right) b_\gamma \hbar \ln(2)}{E_{\gamma i}^{(\lambda_i+2)}\left(^{32}P\right) T_{1/2}\left(^{32}P\right)}$$

where λ is electric or magnetic multipolarity. For the higher energies, the resonance strength becomes insensitive to the proton width as $\Gamma_p \gg \Gamma_\gamma$ and $\frac{\Gamma_p \Gamma_\gamma}{\Gamma} \sim \Gamma_\gamma$.

The proton partial width for the 156-keV resonance was calculated using

$$\Gamma_{\lambda c} = 2\frac{\hbar^2}{M_c a_c^2} P_c C^2 S \theta_{sp}^2,$$

where $\Gamma_{\lambda c}$ is the partial width of the state, M_c is the reduced mass of the system, a_c is the interaction radius, P_c is the penetrability of the Coulomb and centrifugal barrier, C is the isospin Clebsch-Gordon coefficient, S is a single-particle spectroscopic factor, θ_{sp}^2 is dimensionless single-particle reduced widths [Ili97].

We use a single-particle spectroscopic factor of [Ili97] taken from a reanalysis of measurements of the ^{31}P(d,p) reaction [Gas73, Eck89]. However, we find the resonance strength for the 156-keV resonance to be about 50% higher than that recommended in [Mat11b] due to the higher resonance energy found in this work, increasing the ^{31}S(p,γ)^{32}Cl reaction rate for T $\approx$ 0.1-0.25 GK. Level energies and γ ray energies detected in coincidence with ^{32}Cl residues are summarized in Table 4.1.

There is somewhat contradictory evidence regarding the partial widths of the states corresponding to resonances at 550, 628 and 702 keV. The 550-keV resonance dominates the ^{31}S(p,γ)^{32}Cl reaction rate near peak nova temperatures, T $\approx$ 0.25-0.35 GK. With the resonance energy precisely determined, the uncertainty in the ^{31}S(p,γ)^{32}Cl reaction rate in novae now hinges on the strength of this resonance. Gamma branching ratio measurements indicate $\Gamma_p \approx \Gamma_\gamma$ but with large uncertainties (Γ_p/Γ = 50(3'0)%) [Lef97]. However, the mirror to this state is weakly populated in the (d,p) reaction, with a single particle spectroscopic factor of about 0.002 [Eck89], indicating an expected proton partial width of $\Gamma_p \approx$ 0.9 meV, about 9 times smaller than the expected γ width. The proton branching ratio was directly measured by [Mat11b] to be Γ_p/Γ = (7 $\pm$ 4)%, in agreement with expectations from the mirror nucleus.

The 628-keV and 702-keV resonances may contribute to the ^{31}S(p,γ)^{32}Cl rate at the highest ONe nova temperatures (especially if the 550-keV resonance strength is closer to the value suggested from the direct proton-branching ratio measurements of [Mat11b]). Gamma-ray branching ratio measurements for the 628-keV and 702-keV states indicate that the proton branching ratio (Γ_p/Γ) is approximately one [Wre12]. This is supported by neutron spectroscopic factors from the mirror states, which indicate that proton partial widths are expected to be about 25-30 times greater than the γ partial widths for these states. A direct measurement resulted in

Γ_p/Γ = 54(7)% and 66(13)% for the 628-keV and 702-keV states, respectively, indicating a smaller proton width that would decrease the resonance strengths for these two states by about 40%. We recommend adopting a proton partial width that is 4 times larger than the γ width for both these states and adopting an uncertainty that is consistent with both the proton and γ-ray branching ratio measurements. This results in only about a 20% uncertainty in the contribution of these resonances, which likely themselves only make a small contribution at nova temperatures.

We calculate the $^{31}S(p,\gamma)^{32}Cl$ reaction rate using the Breit-Wigner single level formalism described previously using the values from Table 4.2 and with higher energy resonances included using parameters from Ref. [Mat11b]. The reaction rate is plotted in Figure 4.6.

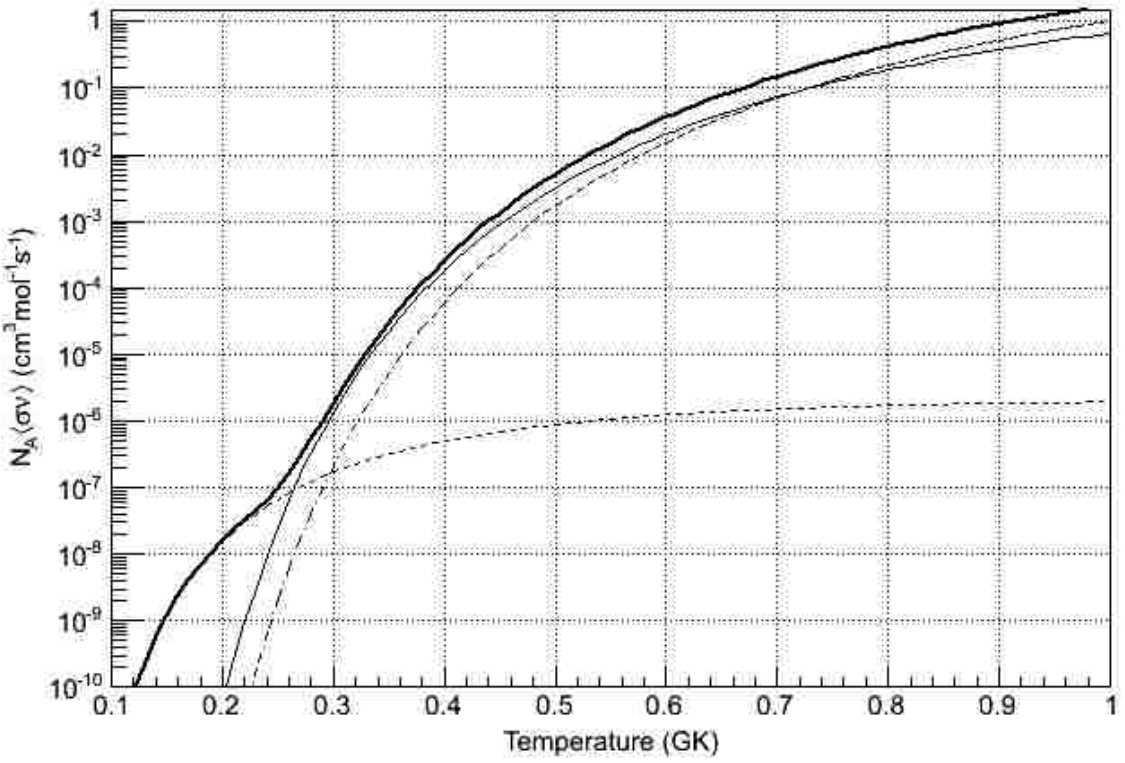

Figure 4.6. Recommended $^{31}S(p, \gamma)^{32}Cl$ reaction rate as a function of the stellar temperature T using ωγ = 1.4 meV for the 550 keV resonance (thick solid line). Contributions to the rate from the 156-keV resonance (dashed line), 550 keV resonance (thin solid line) and all other resonances (dot-dashed line) are also shown.

The individual contributions from the 156-keV and 550-keV resonances are also indicated. However, the uncertainty in the resonance strength of the 550 keV level contributes as much as an order of magnitude uncertainty to the $^{31}S(p,\gamma)^{32}Cl$ reaction rate near peak nova temperatures. This is illustrated in Figure 4.7, where the ratio of the reaction rate is plotted relative to the reference rate from Figure 4.6. The ratio of the rate to the reference rate is plotted (dashed lines) using $\omega\gamma = 7$ meV ($\Gamma_\gamma \approx \Gamma_p$ [Lef97]) and with $\omega\gamma = 0$. Also shown in Figure 4.7 is the ratio of the reference rate to that of [Mat11, Ili10].

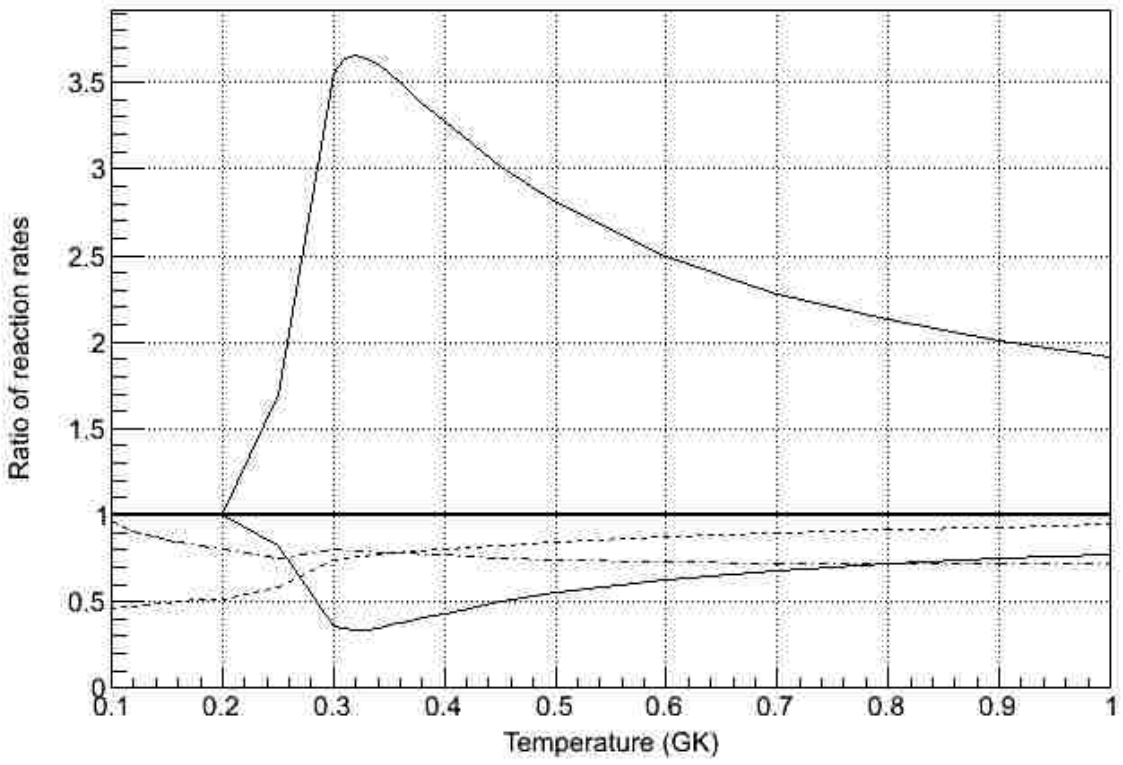

Figure 4.7. Ratio of $^{31}S(p,\gamma)^{32}Cl$ reaction rate from [Ili10] (dashed line) to the recommend rate in this work, and ratio of [Mat11b] to this work (dot-dashed line). Ratio of rates using $\omega\gamma = 7$ meV and $\omega\gamma = 0$ meV for the 550 keV resonance to that using $\omega\gamma = 1.4$ meV as recommended are shown as the upper and lower thin solid lines.

Table 4.2. Properties of states in ^{32}Cl that are important resonances for the ^{31}S(p, γ)^{32}Cl reaction rate in novae. We recommend adopting a mean resonance strength for the 550 keV state consistent with properties of the mirror and that of [Mat11b], but with uncertainties reflecting the relatively loose experimental constraints.

E_x	E_r	J^π	$\Gamma_\square$	Γ_p	$\omega\gamma$	$\sigma(\omega\gamma)$
[keV]	[keV]		[meV]	[meV]	[meV]	[meV]
1737	156.3(7)	(3^+)	1.0	$4.2\text{x}10^{-8}$	$7.4\text{x}10^{-8}$	$1.5\ \text{x}10^{-8}$
2131	549.9(8)	$(3)^+$	8	<8	1.4	<6
2209	628.4(8)	(1^+)	16	>19	10	3
2283	702.4(8)	(2^+)	3.1	>6	3	1

The proton width of the 1737-keV level (156-keV resonance) contributes to uncertainty in the rate at T~ 0.25 GK, and the uncertainty in the γ widths of the levels at Ex > 2200 keV contributes primarily to uncertainties in the rate at T~1 GK. These quantities are constrained only by properties of the mirror system, and the degree of uncertainty that is ascribed to mirror symmetry enters linearly into the reaction rate only at low or high temperatures (having only a small effect in novae). A Monte Carlo analysis of the uncertainty in the rate as presented in [Mat11, Ili10] is not done here since the uncertainties in the reaction rate are entirely determined by uncertainties in the resonance strength of a few levels (determined by properties of mirror levels) whose uncertainty is somewhat subjective and enters linearly into the reaction rate. As illustrated in Figure 4.7, the overall uncertainty for novae is dominantly due to the 550 keV level, and a precise experimental determination of proton or γ branching ratio of the 2131 keV level is the most important target for future experiments.

CHAPTER 5. ^{25}AL MOTIVATION

The higher temperatures reached in X-ray burst explosions result in short time scales for nuclear reactions with reactions occurring on nuclei much further away from stability than in novae, and potentially producing elements as heavy as tin. Nuclear reaction rates determine, which elements will be predominant in the ashes after the explosion that, in turn, influence the later evolution of the system, possibly providing conditions for the occurrence of superbursts. The reaction rates also supply information on the composition of the neutron star crust necessary to understand mechanisms of binary star systems including accretion and mixing mechanisms. The initial nuclear reactions leading to an X-ray burst occur via the hot-CNO cycle of reactions, see Figure 5.1.

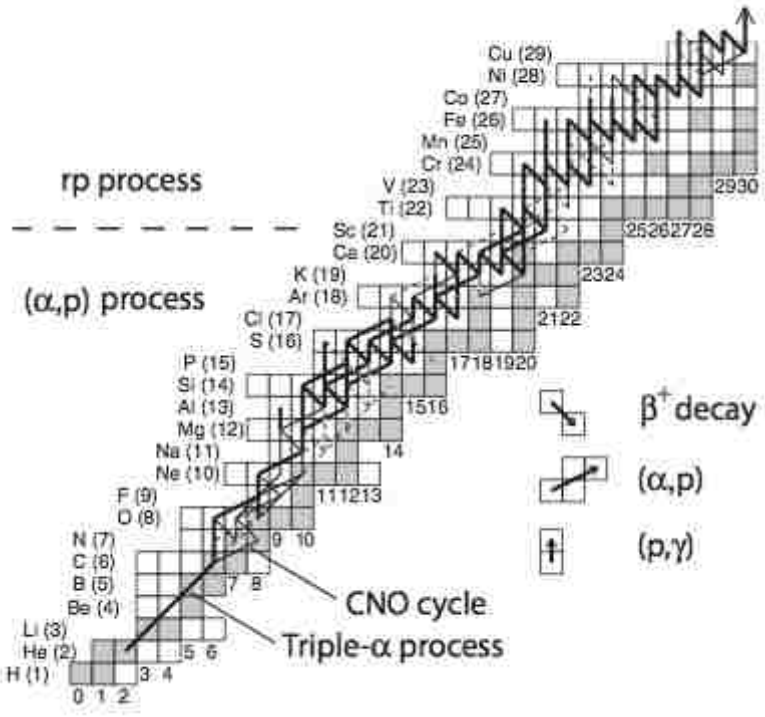

Figure 5.1. The time-integrated reaction flow during the thermonuclear runaway at the surface of an accreting neutron star. [Mat11a]

The energy produced from the hot-CNO cycle increases the temperature until breakout of the hot CNO cycles occurs, which is made more efficient once the triple-alpha process begins making ^{12}C out of three alpha particles. The breakout starts with the $^{15}O(\alpha,\gamma)^{19}Ne$ reaction first, and then, as the temperatures raise, the sequence $^{4}He(2^{4}He,\gamma)^{12}C(2p,\gamma)^{14}O(\alpha,p)^{17}F(p,\gamma)^{18}Ne(\alpha,p)^{21}Na$ starts. This is the beginning of the αp process, a sequence of (α,p)-(p,γ) reactions that produces heavier elements via the $^{21}Na(p,\gamma)^{22}Mg(\alpha,p)^{25}Al(p,\gamma)^{26}Si(\alpha,p)^{29}P(p,\gamma)^{30}S$. . . . sequence [Mat11a].

Many astrophysical models have been built to study the impact of nuclear reactions on the burst properties. Computer simulations of Type I X-ray bursts and the corresponding nucleosynthesis were performed by different groups studying the details of the nuclear processes powering the explosion, see [Woo76, Mar77, Jos77, Lam78]. The scenarios produced by the models heavily depend on the initial conditions, previous histories, i.e. the fact that nuclear composition in the crust depends on the previous accretion in the crust and other factors.

Previous studies show that the nuclear energy production rate in X-ray bursts is significantly affected by a small number of nuclear reactions, many of which are (α,p) reactions, see Figure 5.2.

The αp process is a chain of α-and proton-induced reactions that produces heavier material rapidly, moving from the CNO cycle toward heavier masses in the Ca/Ti region [Mat11a]. This process induces a sharp energy release, leading to a thermonuclear runaway. The energy can be observed using an X-ray burst light curve: the reaction rates of the (α,p) reaction processes influence the shape of the light curve and have a direct effect on its rise time.

Therefore, (α,p) reaction rates on nuclei such as ^{18}Ne, ^{22}Mg, ^{26}Si, ^{30}S and ^{34}Ar are astrophysically important for the thermonuclear runaway. Currently there is very little in the way

Reaction	Models Affected
$^{15}O(\alpha, \gamma)^{19}Ne^{a}$	K04, K04-B1, K04-B6
$^{18}Ne(\alpha, p)^{21}Na^{a}$	K04-B1, K04-B6
$^{22}Mg(\alpha, p)^{25}Al$	F08
$^{23}Al(p, \gamma)^{24}Si$	K04-B1
$^{24}Mg(\alpha, p)^{27}Al^{a}$	K04-B2
$^{26g}Al(p, \gamma)^{27}Si^{a}$	F08
$^{28}Si(\alpha, p)^{31}P^{a}$	K04-B4
$^{30}S(\alpha, p)^{33}Cl$	K04-B4, K04-B5
$^{31}Cl(p, \gamma)^{32}Ar$	K04-B3
$^{32}S(\alpha, p)^{35}Cl$	K04-B2
$^{35}Cl(p, \gamma)^{36}Ar^{a}$	K04-B2
$^{56}Ni(\alpha, p)^{59}Cu$	S01
$^{59}Cu(p, \gamma)^{60}Zn$	S01
$^{65}As(p, \gamma)^{66}Se$	K04, K04-B2, K04-B3
$^{69}Br(p, \gamma)^{70}Kr$	S01
$^{71}Br(p, \gamma)^{72}Kr$	K04-B7
$^{103}Sn(\alpha, p)^{106}Sb$	S01

Figure 5.2. Nuclear reactions affecting productions rates in X-ray burst nucleosynthesis, many of which are (α,p) reactions [Par08].

of experimental constraints on the (α,p) reaction rates, and the rates are mostly based on theoretical models that make use of the Hauser-Feshbach statistical model. Whether the Hauser-Feshbach approach is applicable to in these cases is debatable. The reliability of the statistical model reaction rates depends on the density of resonances in the compound nuclei. Only natural parity states contribute to spin-zero α capture, and whether the density of natural parity states is high enough that reaction rates calculated in the Hauser-Feshbach approach are reliable, especially at lower energies, is questionable. The little amount of experimental information available on (α,p) reactions raises questions about the reliability of Hauser-Feshbach predictions. For example, Deibel *et al.* experimentally measured cross sections for the

$^{33}Cl(p,\alpha_0)^{30}S$ reaction and compared them with the theoretical predictions of the NON-SMOKER code calculations [Rau00, Rau01], see Figure 5.3.

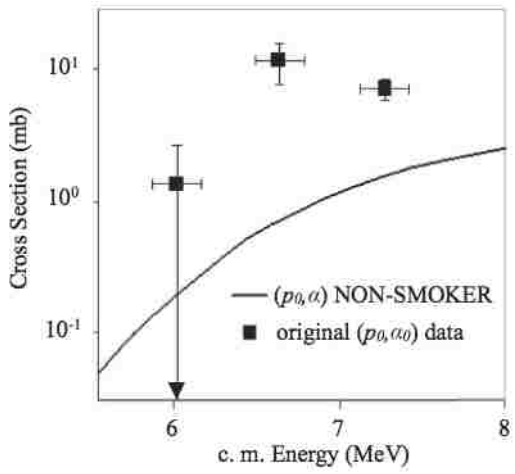

Figure 5.3. Cross section of $^{33}Cl(p_0,\alpha_0)^{30}S$ reaction as a function of the center of mass energy for the experiment (squares) and the NON-SMOKER theoretical calculations[Rau00, Rau01] (solid line). The vertical error bars show the uncertainties in the cross sections, and the horizontal error bars show the uncertainty of the beam in the target (energy spread).

The experimentally determined cross sections for this reaction are approximately a factor of 4-10 greater than those predicted by NON-SMOKER. The theoretical calculations take into account transitions to the excited states in ^{30}S, but those contributions are likely to be rather small in this case, whereas ground-state to ground-state transitions dominate.

Unfortunately, direct measurements of (α,p) reactions are challenging with radioactive ion beams due to the small cross section of the reaction, the low beam energies needed, the required helium target, and the typical low intensity of radioactive beams that are available. Alternatively, indirect approaches can be used to study the properties of states in the compound nucleus that form important resonances.

One of the reactions that has been identified as being particularly important in X-ray bursts is $^{22}Mg(\alpha,p)^{25}Al$, see [Par.08]. Excited states in the compound nucleus ^{26}Si that are above

the alpha threshold are formed as intermediate states in the ^{22}Mg+α->^{26}Si->^{25}Al+p reaction sequence, producing resonances that will dominate the ^{22}Mg(α,p)^{25}Al reaction rate. The ^{22}Mg(α,p)^{25}Al reaction rate was previously based on the assumption of a Hauser-Feshbach rate, but as discussed above, experimental data on the resonance properties are desired to test the assumptions of this model. A number of experiments were focused on studying the nuclear structure and shell-model interpretations of proton-bound states and proton-unbound but α-bound states of the compound ^{26}Si nucleus, and until recently, there has been only extremely limited experimental information available about its levels above the α-emission threshold of 9.164 MeV.

Due to the technical challenges accompanying measurements of (α,p) reactions, indirect approaches to study resonance properties are of great interest. Some of the best information on states at excitation energies that could be important resonances in the ^{22}Mg(a,p)^{25}Al reaction come from a study by [Mat11a] of the ^{28}Si(p,t)^{26}Si reaction studied at the Ring Cyclotron facility of the Research Center for Nuclear Physics (RCNP) at Osaka University, Japan. A 98.7-MeV proton beam from the Ring Cyclotron bombarded a 0.7-mg/cm^2 thick ^{28}Si target of three thin foils in stack. The outgoing tritons were detected by the Grand Raiden spectrometer at three separate angles, −0.3°, 8° and 17° with the fields set in order to study levels of interest in ^{26}S above the alpha threshold. In addition, the ^{12}C and ^{16}O impurities had to be eliminated, so the team used a 1-mg/cm^2 ^{12}C target and a 1-mg/cm^2 Mylar target for background event subtraction. Data obtained in this measurement are shown in Figure 5.4.

The experimental results unequivocally indicate four states above the α-emission threshold, see Figure 5.5. Spins and parities for these four states were tentatively assigned based upon comparisons with the mirror nucleus. Certainly many more resonances exist in this energy

range, and there may be some evidence for additional states in the data. However, in this experiment the statistics was low, the background level from ^{10}C and ^{14}O was high, and therefore unambiguous identification of states was difficult. In addition to this, the measured ^{26}Si spectrum

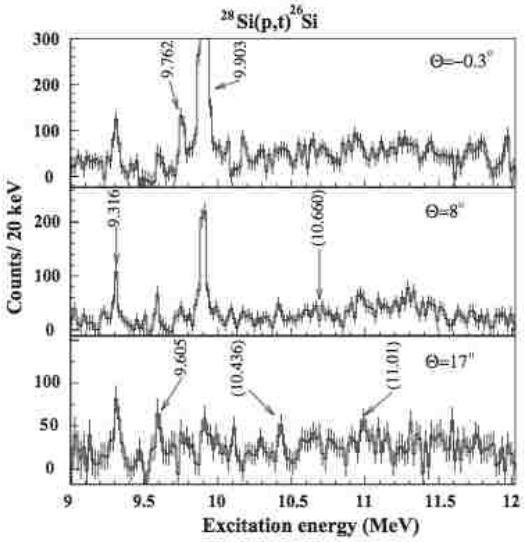

Figure 5.4. The ^{28}Si(p,t)^{26}Si spectra above the α-emission threshold measured at −0.3°, 8° and 17° angles by Grand Raiden spectrometer with the background from ^{12}C and ^{16}O subtracted.

J^π mirror	E_x ^{26}Si (MeV)	E_x ^{26}Mg (MeV)
[4$^-$]	9.316(5)	9.579(3)
[2$^+$]	9.605(10)	9.85652(6)
[5$^-$]	9.762(4)	10.040(2)
[0$^+$]	9.9034(20)	10.159(3)
	[10.436(10)]	
	[10.66(2)]	
	[11.01(3)]	

Figure 5.5. States observed above the α threshold in ^{26}S via the ^{28}S(p,t)^{26}S reaction with spins and parities assigned [Mat11a] are compared to states in ^{26}Mg.

exhibits no stark features, and it was surmised that in ^{26}Si there exist weakly populated natural-parity states of different multipolarities that could not be resolved. The identified energy levels could in fact turn out to a mixture of more than one level, given the fact that the mirror nucleus ^{26}Mg has a relatively high density of levels in this energy region.

One sensitive way to look for resonances in a compound nucleus is proton scattering. This approach has been widely utilized with radioactive ion beams in inverse kinematics and has been proven to be quite successful, for example see [Rui05, Pra14]. One experiment studied states in the nucleus ^{26}Si through elastic proton scattering using a ^{25}Al radioactive ion beam [Che12]. Proton elastic scattering in the corresponding energy range could help clarify which states might correspond to strong resonances in the ^{22}Mg(α,p)^{25}Al reaction.

The experiment was performed in inverse kinematics at the University of Tokyo's Center for Nuclear Science (CNS) Radioactive Ion Beam (CRIB) facility, located at the RIKEN Nishina Center in Wako, Japan. The primary beam of $^{24}Mg^{8+}$ was accelerated to 7.5 MeV/nucleon by the Azimuthally Varying Field (AVF) cyclotron. It bombarded a primary ^{2}H gas target cooled to liquid nitrogen temperatures. The secondary beam of radioactive ^{25}Al was produced via the ^{2}H(^{24}Mg,n)^{25}Al reaction and selected from the primary ^{24}Mg beam using a pair of magnetic dipoles and a Wien filter velocity separator. The resulting beam energy was ~3.4 MeV/nucleon with about 50% purity and an intensity of up to 10^6 pps on the secondary target. In addition, the remaining contaminants were eliminated with two parallel plate avalanche counters (PPACs), which were also used to determine the beam position on the secondary target and the scattering angle of the reaction residues.

Six resonances corresponding to energy levels in ^{26}Si were observed, see Figure 5.6. The protons were detected at laboratory angles of (a) θ_{lab}=0° and (b) θ_{lab}=17°, and the data were fit

using excitation functions of elastically scattered protons in different spin-parity combinations for the six proton resonances using the R-matrix approach, which allowed calculating spins and parities of corresponding resonances, see Figure 5.7. The primary results are summarized in Figure 5.8 [Che12]. However, the primary goal of the experiment was to study levels in ^{26}Si that are relevant for the ^{25}Al(p,γ)^{26}Si reaction that is important for understanding ^{26}Al production in novae, and the incident bombarding energy was too low to populate states in ^{26}Si that are important for the ^{22}Mg(α,p)^{25}Al reaction in X ray bursts.

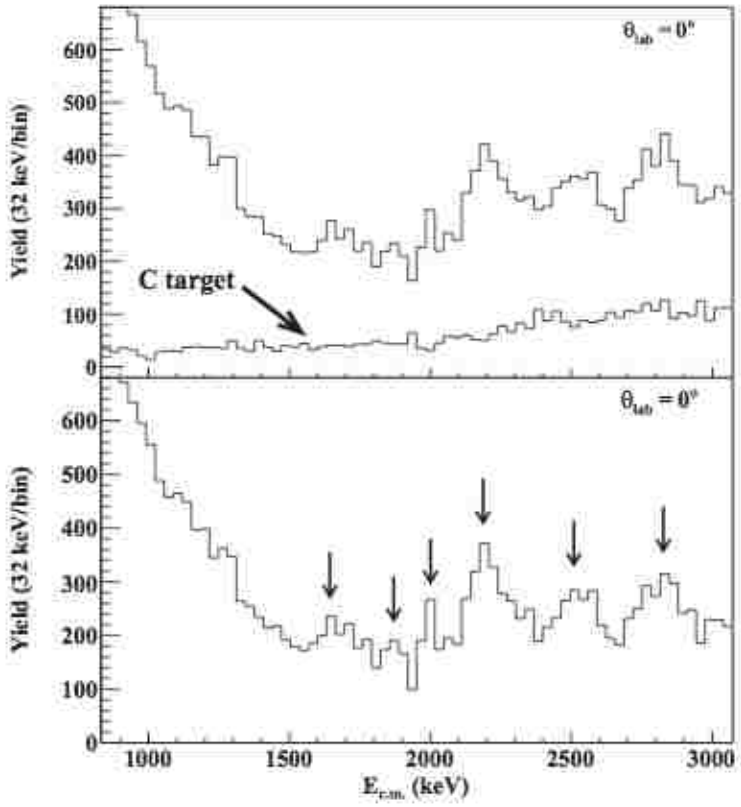

Figure 5.6. Measured ^{26}Si structure with the possible levels indicated from [Che12].

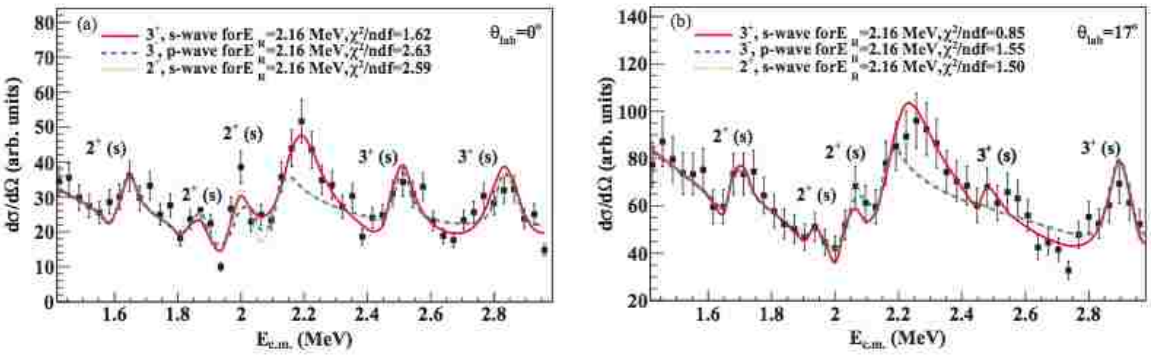

Figure 5.7. R-matrix analysis of the data from [Che12].

This work	(p,t) [20][a]	(p,t) [6]	(p,t) [13][a]	β^+ decay [16][d]	(^{3}He, n) [15][b]	(^{4}He,^{6}He) [19]	(^{3}He, n) [21][a]	(p,t) [22][a]
7.162(14), 2^+	7.157(4), 2^-	7.151(5)	7.160(5)		7.152(4), 2^+	7.161(6)	7.150(30), 2^+	7.150(15)
7.402(40), 2^+	7.439(6), (2^-)	7.4152(23), (4^+)[a]	7.425(7), (2^-)		7.425(4), 0^+	7.429(7)	7.390(30), (0^-)	
7.484(13), 2^+	7.512(8), (2^+)	7.479(12)	7.498(4)	7.501(5), 2^+	7.493(4), 2^-	7.480(20)	7.480(30), 2^+	7.476(20)
				7.606(6)				
		7.522(12), (5^-)[c]						
	7.672(2), 3^-	7.661(12), (2^-)[c]	7.687(22), 3^-		7.694(4), 3^-	7.676(4)		7.695(31)
7.704(13), 3^+		7.701(12)						
	7.875(2), 1^-	7.874(4)	7.900(22), 1^-		7.899(4), 1^-	7.885(4)	7.900(30)	7.902(21)
				7.962(5)				
8.015(14), 3^+								
				8.156(21), 2^-			8.120(30), (2^-)	
		8.222(5), (1^-)[c]						
		8.269(4), (2^-)[c]		8.254(5)				
8.356(12), 3^+								

[a] J^π from a Distorted-Wave-Born-Approximation (DWBA) analysis.
[b] J^π from a Hauser-Feshbach analysis.
[c] J^π from a mirror assignment.
[d] J^π from allowed β^+ decay and comparisons with shell-model calculations.

Figure 5.8. Level energies (MeV) and spin-parities in ^{26}Si from [Che12] work in comparison with those of previous studies.

The goal of our experiment was to extend measurements of the ^{25}Al+p elastic scattering cross section to higher energies than covered by Chen *et al*., to energies above the alpha threshold in ^{26}Si, and into the range covered by ^{28}Si(p,t)^{26}Si [Mat11a]. The most important energy range is E_x = 9 – 10 MeV, where 0^+ and 2^+ resonances, corresponding to *s* and *d* wave alphas respectively, are likely dominate the ^{22}Mg(α,p)^{26}Si reaction rate. These states likely have small proton spectroscopic factors, but ^{25}Al+p elastic scattering is particularly sensitive to 2^+

(and 3^+) states (corresponding to *s* wave protons) as even states with small spectroscopic factors can have significant proton widths due to the high penetrability at these energies.

CHAPTER 6. ^{25}AL EXPERIMENT

We measured the ^{25}Al+p elastic scattering cross section in inverse kinematics at the John D. Fox Superconducting Accelerator Laboratory at Florida State University. A radioactive ^{25}Al ion beam was used to produce the reaction of interest. Radioactive beams became the focus of heightened attention of the nuclear physics community during the past couple of decades and have since been widely used to produce nuclear reactions with unstable isotopes in the laboratory setting. Radioactive beams are more difficult to make and maintain than the stable ones. Often such radioactive beams are made using a stable beam as a primary source and then have to be extracted out of the primary target and reaccelerated towards the second target used for the measurement itself.

The ^{25}Al beam used in this experiment was produced using the Resonating Solenoid Upscale Transmission (RESOLUT) facility, see Figure 6.1, by a different technique, the "inflight" method from the ^{24}Mg(d,n)^{25}Al reaction with a primary ^{24}Mg beam. Negatively-charged MgH_2 ions were produced using a cesium sputter ion source with a MgH_2 cathode. The negative ions are extracted from the source high voltage platform at an energy of 120 keV, then mass separated and injected into an FN Tandem Van de Graaff accelerator that was operated at a terminal voltage of ~ 8.5 MeV for this measurement. Negatively charged ions with the charged state of 1^- are accelerated to the Tandem terminal, where the MgH_2 molecule is dissociated in a carbon stripper foil, and the resulting positively charged ions undergo a second stage of acceleration down the high-energy column of the tandem accelerator. The Tandem analyzing dipole magnet selected positive ions with charge 8^+, producing a beam of $^{24}Mg^{8+}$ ions with an energy of 76 MeV.

A special capability of the Fox Superconducting Accelerator Laboratory is a superconducting linear accelerator (LINAC) located after the Tandem accelerator that can be

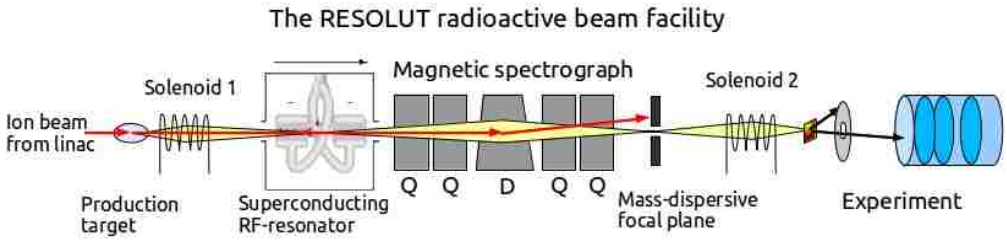

Figure 6.1. Schematic illustration of the Resonating Solenoid Upscale Transmission Facility (RESOLUT) used for radioactive beam production at the Florida State University [FSU15].

used to accelerate ions to substantially higher energies than using the tandem alone. The LINAC consists of a series of 12 independently-phased superconducting resonators operating at 97 MHz inside 3 cryostat tanks cooled to 4.8 K by liquid helium. Resonators used in the LINAC are identical to the split-ring type resonators used by the Argonne Tandem-LINAC Accelerator System (ATLAS). The cavities are made of double-arm pure Niobium drift-tubes inside a copper housing, which is also coated by Niobium on the inside [Roj11]. While the Tandem typically produces beam that is continuous in time (i.e. DC), the LINAC requires a beam with a pulsed structure with narrow time resolution. The acceleration of the particle bunches in the LINAC is achieved by maximizing the RF-frequency effective electric field on the positive beam bunches when they cross the resonator to produce the maximum electric field gradient. In order to shape the beam and achieve good time and spatial resolution, a bunching and chopping system is used. The low energy beam is first bunched by an RF accelerating field before entering the Tandem that creates relatively tight time bunches of particles, though with significant DC background between bunches. The beam is then chopped using an electrostatic deflector in the beginning of

the LINAC that eliminates the particles that come at times between the narrow time bunches, and entering the cryogenic gas cell through a 2.5 μm thick Havar window. The D_2 gas target was kept at 350 Torr and 80 K (cooled to liquid nitrogen temperature to increase the gas density). While the cross section for the (d,n) reaction is favorable, the amount of ^{25}Al produced is still a small fraction of (10^{-4}-10^{-5} times) the incident primary ^{24}Mg beam. The unreacted ^{24}Mg beam and the ^{25}Al exit the gas cell through a second 2.5 μm thick Havar window to create a secondary beam that is analyzed by RESOLUT using a combination of ion optical elements to separate the unreacted ^{24}Mg from the ^{25}Al. RESOLUT contains a set of two superconducting solenoids, dipole and quadrupole magnets, and a superconducting resonator. Its settings were optimized to produce a ^{25}Al beam with maximum possible intensity and purity. Over the course of this experiment, the resulting beam on target consisted of about 10^4 particles per second with about 30% ^{25}Al with the remaining content being ^{24}Mg (70%). While a very high suppression of ^{24}Mg is achieved (several orders of magnitude), no perfect separation of the species is possible as $^{24}Mg^{+12}$ and $^{25}Al^{+13}$ ions have nearly the same charge-to-mass, and some ions will have the same magnetic rigidity.

The mixed beam of ^{24}Mg and ^{25}Al bombarded a polypropylene $(CH_2)_n$ target, see Figure 6.2. In this experiment we used a target with a thickness of 2.05 mg/cm^2. The target ladder had several positions. One was reserved for a collimator used to help focus the beam. The most probable energy for the ^{25}Al beam resulting from the manipulations described above was calculated using energy loss and kinematic functions found in LISE++ software.

The dominant cross section consists of elastic scattering of the incident beam off of the carbon and hydrogen in the target. Given the relatively modest intensity of the radioactive ion

beam, it is important to maximize the detection efficiency. Protons resulting from ^{25}Al scattering on the target were emitted at forward angles and detected by a telescope of two layers of an

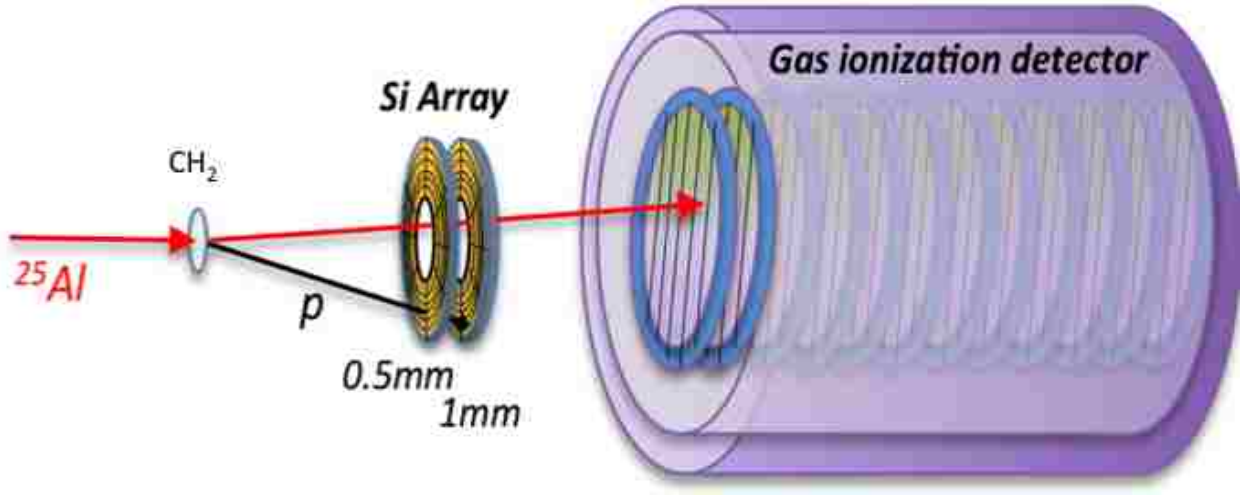

Figure 6.2. Schematics of the setup used in this experiment. The ^{25}Al-^{24}Mg beam is shown with the read arrow. The beam impinges of the polypropylene target (gray), the light particles get detected in the silicon at forward angles, while the heavy reaction products enter the position-sensitive ionization chamber.

annular silicon strip detector, a front detector of Micron Semiconductor Design S2 (500 μm thick) and a back detector of Micron Semiconductor Design S2 (1000 μm thick) as illustrated in Figure 6.3.

The front side (p-junction) of each detector has 48 rings and back (n-junction) has 16 segments. The active inner diameter of an S2 detector is 22 mm and the outer diameter is 70 mm. The second silicon detector was 8 mm behind the first. The rings of the ΔE detector and the segments of the E silicon detector faced the target ladder. The thinner S2 detector was positioned 72 mm from the target, and subtended at angles of $10.7° < \Theta_{lab} < 39.7°$, for this experiment. The back detector was positioned 80 mm from the target. For this experiment the Si detectors were

set up in such a manner that their rings were connected in threes, and the data were collected from three adjacent rings simultaneously.

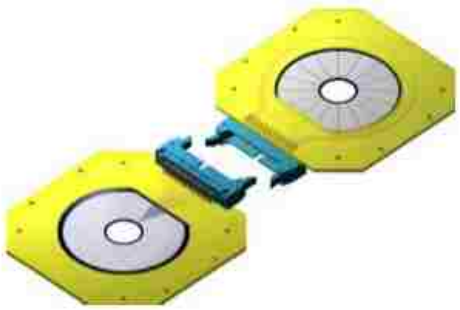

Figure 6.3. A Micron Semiconductors S2 silicon strip detector with its printed circuit board viewed from p-side (front side, rings, bottom) and n-side (back side, segments, top).

Using two layers of detectors is a common experimental technique to allow identification of the atomic number of detected particles by their relative energy loss. The position of the ions registering in the silicon was determined by the ring and segment number where an event was recorded. We reconstruct the lab angle from the measured position in the silicon assuming that all the reactions happen in the target centered on the beam axis. This angle was used in the subsequent data analysis to reconstruct the energy of the reaction particles in the center of mass frame, see Chapter 7. The reaction angle can be determined separately from the position of particles in the two Si detectors. We adopt the angle from the front ΔE detector because protons undergo straggling in the ΔE detector and the position in the second E detector is not as reliable. However, correlations between the positions in the two detectors can be used to help suppress background.

Another challenge was posed by the presence of the stable ^{24}Mg that is the dominant component of the beam. Kinematics of the protons alone is not sufficient to distinguish proton elastic scattering from ^{24}Mg and ^{25}Al. Therefore, heavy ions were detected by a position-

sensitive, gas ionization detector that was designed for fast counting rates (see Figure 6.4) in coincidence with the Si array.

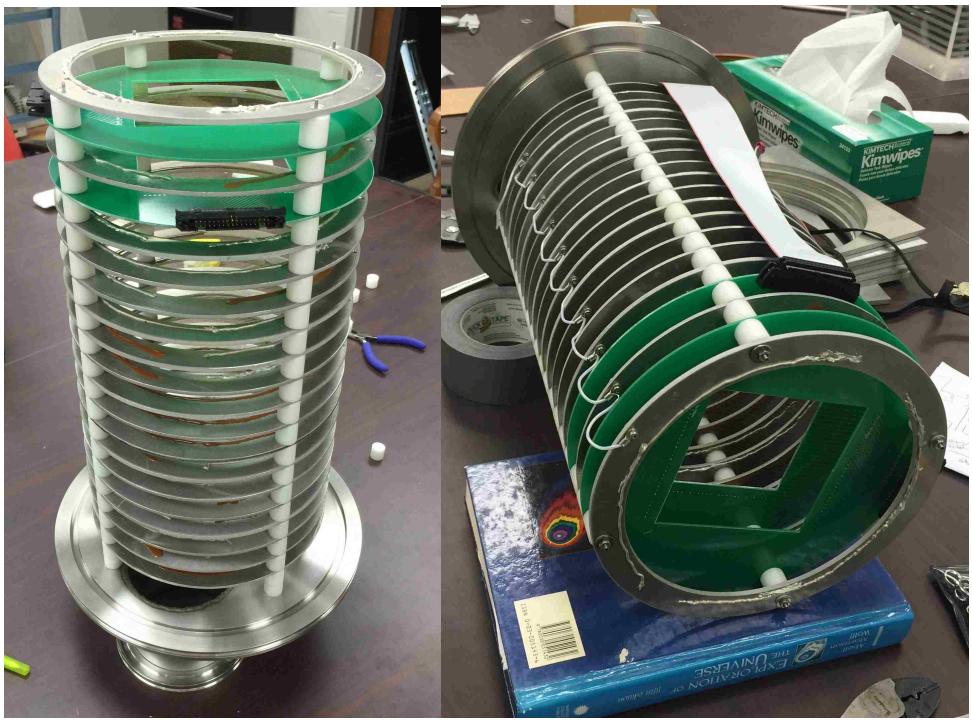

Figure 6.4. Position-sensitive ionization chamber used in the experiment. One can see the tungsten wires.

The ionization detector design is based on the ionization chambers previously constructed at RIKEN [Kim05] and in use at Oak Ridge National Laboratory (ORNL). While the specifications of these detectors somewhat differ, they all are based on alternating cathode (ground) and anode (potential) planes in close (<2 cm apart) proximity to reduce the electron/ion drift length. The cathode/anode plates are gold-plated tungsten wires (19 μm diameter) wound in parallel on an aluminum rings (except for the position-sensitive planes, see below) with a spacing of 2 mm between the wires to achieve 98.8% transmission through each wire plane, with a total efficiency of about 90%, depending on the depth that ions penetrate into the detector. The

planes are mounted in parallel inside the chamber at equal distances from each other and are divided into three separate sections, the *ΔE*, the *E*, and the position-sensitive one, with two separate anode planes that provide position sensitivity. This position-sensitive section is a distinguishing feature of the detector used in this experiment.

In our setup the first two wired anodes in the ion chamber were the position-sensitive planes interspersed with the cathode (ground) planes. These planes were the closest to the Si detector array. The two position sensitive sections consist of electrically isolated conducting wires with a 2 mm spacing that are mounted on a printed circuit board (PCB, See Figure 6.5). Using a PCB allows taking out signals from each wire separately and feeding them into electronics. Wires were read out in groups of two to provide information on the position of the ions. This distinguishes them from the non-position sensitive sections of the ion chamber, where the signals from all wires on a plane are summed. This section gives the x and y positions of the particles of interest, the first plane being the x coordinate of the particles, and the second the y.

The set of planes following the position-sensitive planes was the 5 anode planes interspersed with the ground planes. The 5 planes were wired together and powered to be at the same potential. From these 5 anode planes we extract the ΔE energy loss. The heavy recoils lose the rest of their energy in remaining sections, the furthest from the Si detectors. All anode planes and the position-sensitive grids were at +250 V. The grounded planes wires were all wired together.

The ion chamber was filled with isobutane gas to a pressure of 24 Torr for this experiment.

Signals from the Si detectors were processed first through external LASSA preamplifiers [Dav01] going directly into a HINP ASIC (Application-Specific Integrated Circuit) data

acquisition system. The HINP ASICs were developed and manufactured by Washington University in St. Louis for doing measurements with large arrays of silicon strip detectors.

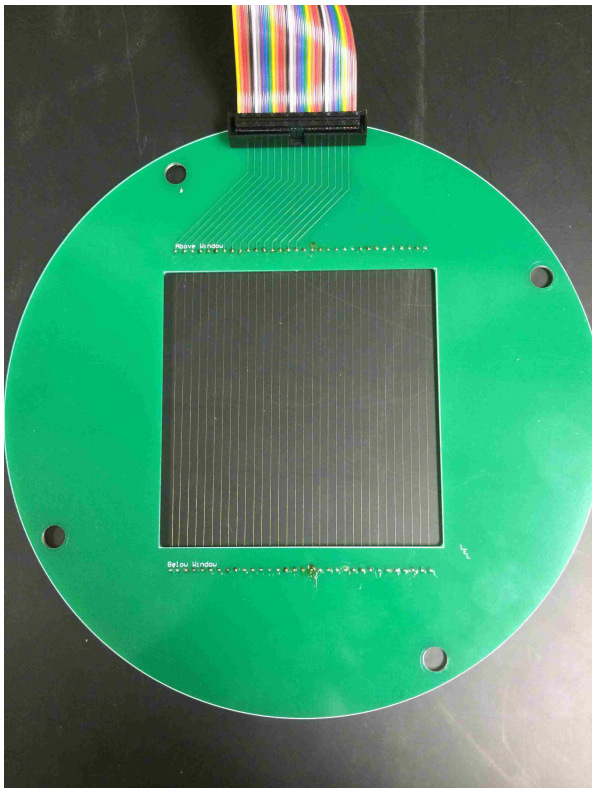

Figure 6.5. Printed circuit board with the ribbon cable that takes out signals from the ionization chamber.

The HINP ASICs have independent shapers and CFDs (constant fraction discriminators) for each strip of the Si detectors, which constitute one channel. Each ASIC chipboard has 32 channels total. The shaper takes a signal from a channel and converts it into a Gaussian, whose height is proportional to the amount of charge/energy deposited by the particle in the detector. The ASIC samples the height of the signal, multiplexes it, and constructs time-multiplexed analogue waveforms with a voltage train that provides a measure of the energy for each channel. The multiplexed signal train goes into an XLM XXV flash digitizer. The ASIC system is highly

cost-effective. Better performance (better resolution and lower thresholds) and greater flexibility are possible using external preamps as was done in this case. However, this also requires preamplifiers that are selected to provide gains that are matched to the dynamic range of particles to be studied.

The ΔE-E IC signals didn't go through the ASIC electronics used for the Si, since the energies the ions deposit in the ion chamber can vary greatly, and conventional shaping electronics allow for additional flexibility in gain adjustment. Thus, the ΔE-E IC signals used the same preamplifiers as the Si detectors, but after the preamplifiers the ΔE-E IC signals are fed into the conventional NIM ORTEC 572 shaping amplifiers and peak-sensing VME ADC (analogue-digital converter), which give more flexibility over the gains than the ASIC. Signals from the position-sensitive planes were sent through 16-channel Mesytec shapers, and then through the VME ADC.

CHAPTER 7. SELECTION OF ^{25}AL+P EVENTS

The experimental data were collected by the NSCLDAQ (National Superconducting Cyclotron Laboratory data acquisition system) developed at Michigan State University. The master trigger for the system was set as a logical "OR" of triggers from all channels in the silicon-strip detectors and a "downscaled" sample of events from the ion chamber storing one in a 1000 events that trigger the ionization chamber. Since our primary goal is to measure protons produced in the ^{25}Al elastic scattering reaction, the primary trigger is set to keep all events with any signal above threshold in the silicon array, which is general set just above the noise threshold. However, ^{24}Mg from the primary beam also impinges on the target and produces elastically scattered protons. Fusion evaporation reactions from both the ^{24}Mg and ^{25}Al produce protons and other background. Therefore, other criteria have to be applied to discriminate protons of interest scattering from ^{25}Al from other events. Figure 7.1 is an energy spectrum of the signals from the 500-micron-thick ΔE versus the total energy, E_{total}, in both silicon detectors (sum of energies detected in the ΔE and E detectors) without any cuts applied.

Given the thickness of the ΔE layer, most particles stop in the first layer, producing a line of slope 1 in the plot where $\Delta E=E_{total}$. At the bombarding energies in this experiment, essentially only hydrogen ions penetrate through the first silicon ΔE detector, and the dominant feature in the middle of Figure 7.1 arises from protons that deposit energy in both detector layers. Most of the other features that do not lie on the $\Delta E=E_{total}$ line arise from noise and random coincidence events that are easily suppressed. Elastically scattered deuterium, which is present in the natural isotopic composition target at the level of 0.1% compared to hydrogen, is also evident as a parallel band with appropriate intensity.

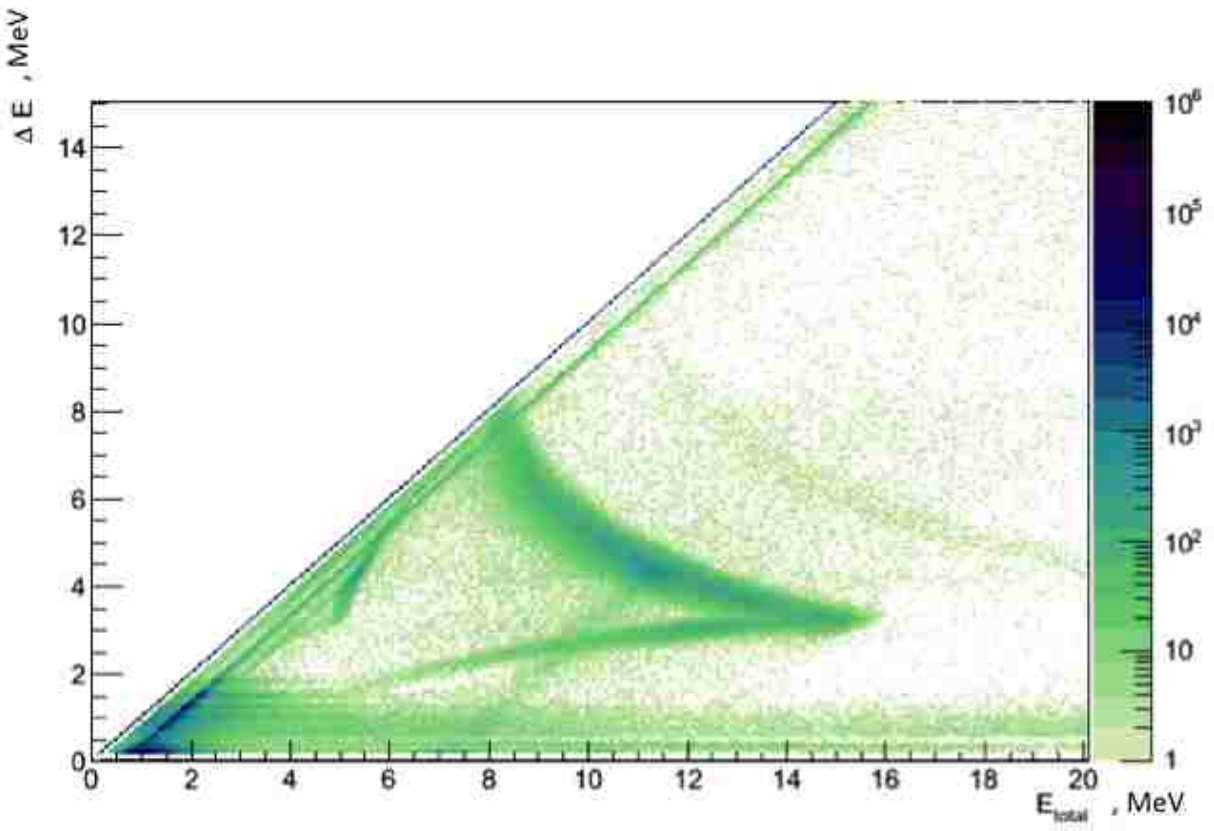

Figure 7.1. Energy recorded in the first ("*ΔE")* layer of silicon detectors vs. the total energy, E_{total}, recorded in both layers, effectively *ΔE+E* with no conditions.

The majority of events originating from noise and random coincidence are filtered by selecting events where only one event is identified in each of the *ΔE* and *E* silicon detectors (by its ring and segment number). Proton elastic scattering events should be characterized by substantial (> 1 MeV) energy deposit in both detectors, and these two events should be correlated to have the same scattering angles in both detectors. A cut was applied to select events where the position in the first silicon detector is correlated with the position in the second silicon detector. As a proton is emitted from the target, it passes through the first Si *ΔE* detector at a certain angle and then into the *E* detector. Since the reaction is occurring at forward angles, and the two detectors are placed close together (8 mm between the detectors), the proton incidence

angle measured in the first and the second detector shouldn't differ by more than a few degrees, characterized by the amount of straggling in the ΔE detector. If we plot θ_1 (the angle in the ΔE detector) vs. θ_2 (the angle in the E detector) as shown in Figure 7.2, we see that most of the events lie at the same laboratory angle in both detectors. If the difference in the incident angles is greater, these two events may be two separate protons arriving into the two detectors in coincidence (e.g. from fusion evaporation), or are protons that did not originate from the target position but come from scattering or reactions upstream, or are perhaps random coincidences. We select events of interest to be the region of $|\theta_1-\theta_2|<5^0$. Figure 7.3 shows the θ_1 vs. θ_2 plot but with events selected that register just one hit in each layer of the silicon and with the $|\theta_1-\theta_2|<5^0$ angular correlation condition applied.

Figure 7.4 shows the silicon ΔE-E plot (similar to Figure 7.1) but with the requirement that only one event is recorded in the ΔE layer and one in the E silicon layer, and that the scattering angles in both detectors is within 5^0. By selecting single hits in both detectors, angular correlated events, and selecting a gate on the proton particle identification band, we can quite cleanly select events containing a single proton in the silicon detectors. The gate that we have applied to select protons from the target is also shown in Figure 7.4.

Several aspects of the silicon-strip detector performance should be noted. The Si detectors are segmented detectors, which means that their surface area is divided into segments that one can use to define position resolution of the incoming particle, but it also means that a small fraction of time protons can hit between the segments with the energy being shared between two adjacent strips. It is known from manufacturer specifications and from previous experience that the area between strips is small. With the detectors subtending small angles, only a very small fraction of the time is energy shared between the segments. The calculated energy

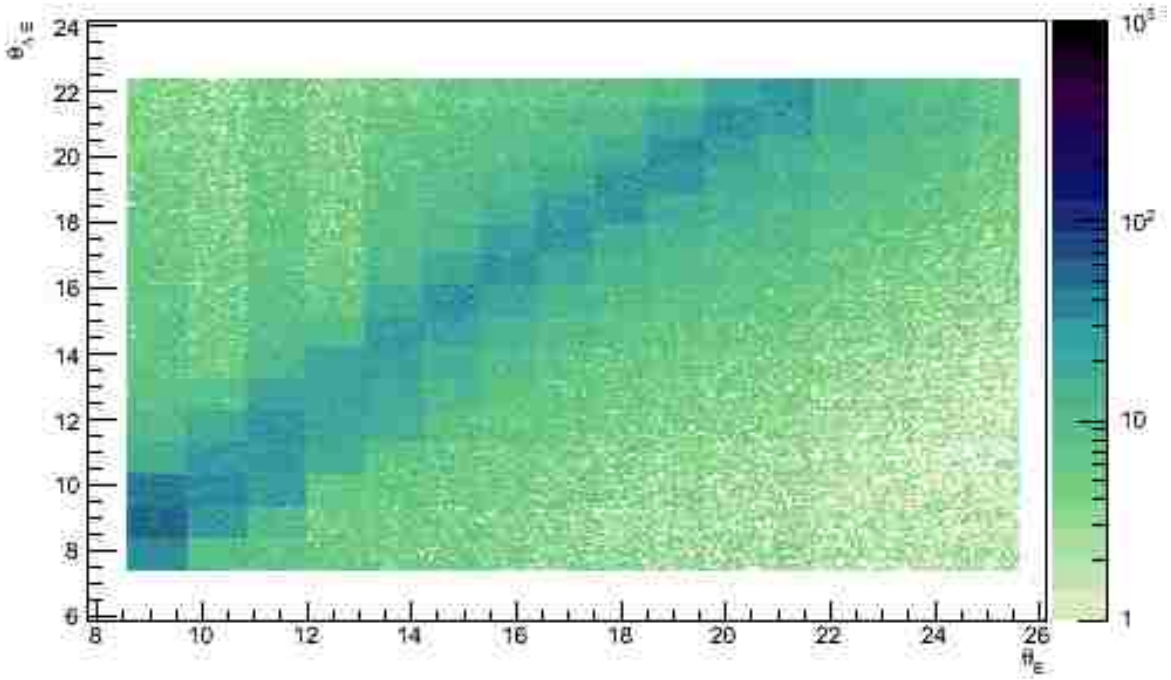

Figure 7.2. The laboratory angle, θ_1, in the ΔE silicon detector vs. the laboratory angle, θ_2, in the E silicon for all events. Angles are given in degrees.

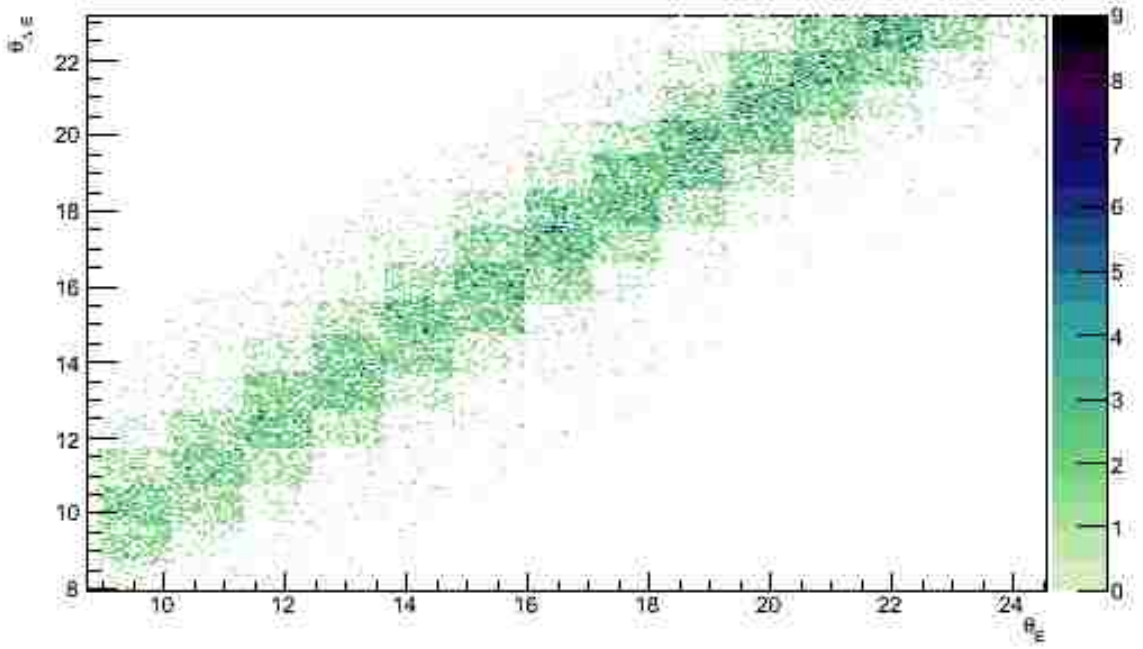

Figure 7.3. Plot of θ_1 vs. θ_2 in the Si detectors with the requirement that there is only a single event in each layer, and that the difference in laboratory angles is less than 5°.

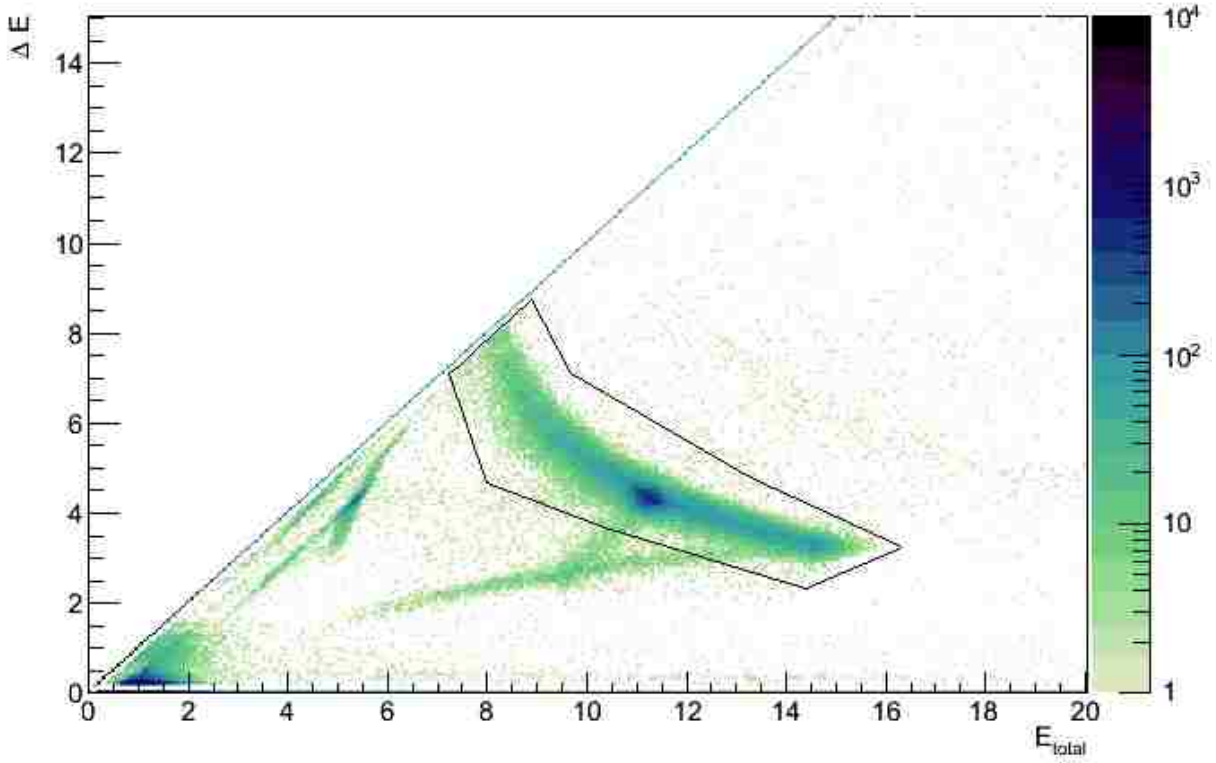

Figure 7.4. Silicon particle identification plot *(ΔE-E)* in MeV for events with no more than 1 hit in each detector that are correlated in angle with 5°.

of protons in the Si array could be corrected for this when cases when charge sharing is between adjacent strips is seen. In our case, the percent of such events is small, and we select events where energy above threshold is recorded in only one segment in each of the S2 detectors. A bigger problem is likely noise in channels in the silicon strip detector, given the relatively low threshold set, that causes good proton events to be rejected as double hits.

We examined deuterium scattering events to test the level to which our cuts to reject double hits in any detector and require angular correlation that might suppress good scattering events. Deuterons are best suited to such a test since they are weakly produced in fusion evaporation reactions. Protons are also problematic since there is a relatively high flux of protons present in the beam. This is the intense group in the proton band at an energy of about 11.5 MeV.

In Figure 7.5 we plot the energy spectrum of events identified as deuterons (blue curve) by their characteristic position in the particle identification plot (Figure 7.1).

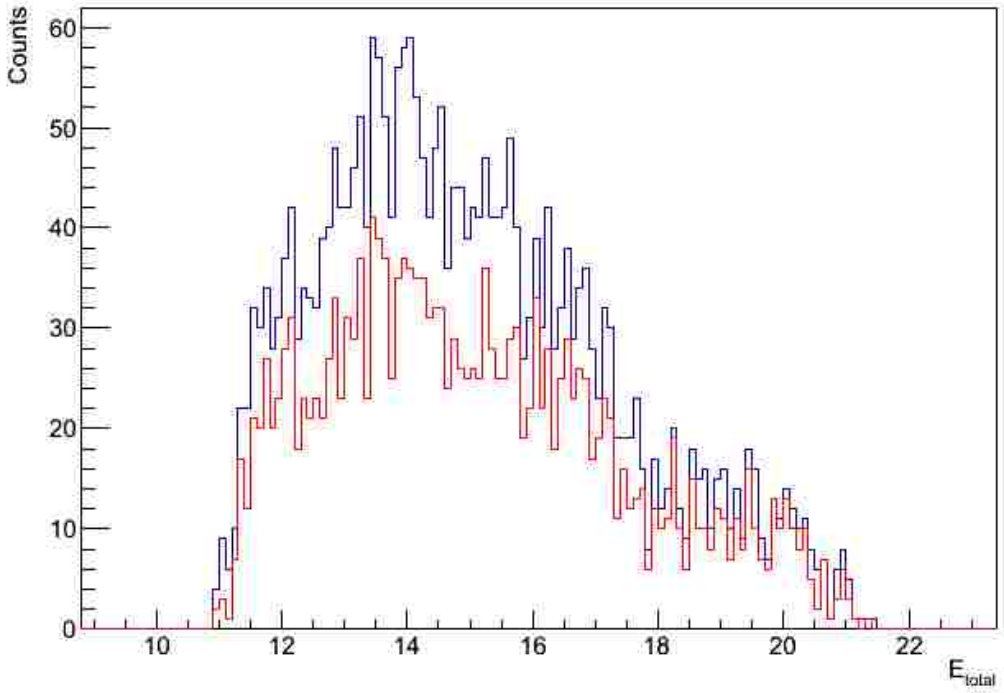

Figure 7.5. Raw spectrum of events identified as scattered deuterons (blue) compared to the spectrum when double hits are eliminated and a correlation between the angle in ΔE and E is required.

We also plot the number of events that survive cuts that eliminate double hits and require angular correlations (red curve). Overall, 70% of the deuteron events pass these cuts. It could be that some of the reduction is due to suppression of fusion evaporation and background, but 30% is a reasonable upper limit on the reduction in efficiency by accepting only angle-correlated single protons events.

While it is clear that the selection of signals in the silicon detectors alone has cleanly identified events with a single proton in the silicon detectors, most of these events still arise from ^{24}Mg scattering off protons in the target, from fusion-evaporation reactions, and from protons not

originating from the target but produced or scattered from upstream of the target. Therefore, we developed a number of cuts to cleanly select events arising due to ^{25}Al+p scattering from other events. While most cuts are not exceptionally clean individually in identifying the events of interest, a number of cuts when simultaneously applied can very cleanly select ^{25}Al+p scattering events with high efficiency.

Selection of the ^{25}Al+p scattering events was done in part by triggering on Si events and establishing coincidences between the protons in the Si array and Al ions identified in the ionization chamber. As the first step, we select only valid proton events that fall within the proton gate shown in Figure 7.4. Protons with an energy of greater than about 8 MeV punch through the first 500-μm-thick ΔE silicon layer, and are easily identified by their relative energy loss. Note that all protons from ^{25}Al+p elastic scattering should have a laboratory energy greater than 9 MeV and punch through the ΔE detector.

Most of the ^{25}Al and ^{24}Mg that enter the target don't react. If beam particles scatter from the hydrogen in the target or are unreacted, they emerge from the target with a very small laboratory angle, less than 2.5°. These particles also pass through the opening in the middle of the Si detectors and proceed further to deposit their energy in the gas ionization detector. Triggering on the ion chamber separately from the Si detectors allowed us to monitor the properties of the incident beam since most of the beam particles do not interact in the target except by their energy loss with atomic electrons. A downscaling by a factor of 10^3 was applied to the ion chamber to reduce the high trigger counting rate, which was typically on the order of 10^4 ions/s during this experiment. Collecting all the events in the ion chamber was not necessary; instead, a sample of all the IC events was sufficient for beam diagnostics.

The recoiling heavy ions that have reacted also pass through the center hole in the S2 detectors and impinge onto the ionization chamber. One very selective cut for separating ^{25}Al+p scattering from ^{24}Mg+p scattering and other reactions is the relative energy loss of the heavy ion in the ΔE and E sections of the gas ionization detector. The quantity of ionization of the gas in the chamber that occurs due to energy losses of heavy recoils is proportional to Z^2; thus, the ^{25}Al ions have a higher energy loss in the ΔE layer for a given incident energy, and bands of events resulting from Mg and Al are distinguished as shown in the raw ionization chamber particle identification spectrum, Figure 7.6, where we plot the energy loss, ΔE, in the section of the first 2 anode planes in the ion chamber that are placed after the position-sensitive grids versus the sum of energy loss, E_{total}, from all anode grids taken together excluding the position-sensitive grids. The data shown in Figure 7.6 include all events the ionization chamber registers, including those triggered by the downscaled ionization chamber trigger and the silicon detector array. No cuts are included on the data shown in Figure 7.6.

The IC efficiency should be more than 85%. To get a theoretical number, we divide the width of the wire by the distance between the wires, i.e. 25 μm/2mm, raised to the power of the number of planes the ion goes through. If an ion hits a wire, it stops. The ions that stop on some of the wire planes can be seen in Figure 7.6 as groups that have the same ΔE, but with a total energy that is less because they hit a wire before depositing their full energy in the gas. For one plane the transmission if 98.75%. Our ^{25}Al ions travel in gas through 13 planes on average, and the theoretically calculated efficiency should be about 85% for recording the full energy of the ions in the gas.

We can test the efficiency of the gas ionization detector by gating on protons in the Si array, and then looking for events in coincidence in the IC. Every elastically scattered proton

should have a corresponding heavy ion. However, there are also protons that arise from fusion evaporation reactions, and the recoiling heavy ions from these reactions are lower in energy and have a higher atomic number, so they may stop in the IC window or shortly after. The contribution of these fusion evaporation reactions is evident in Figure 7.4 by the relatively large

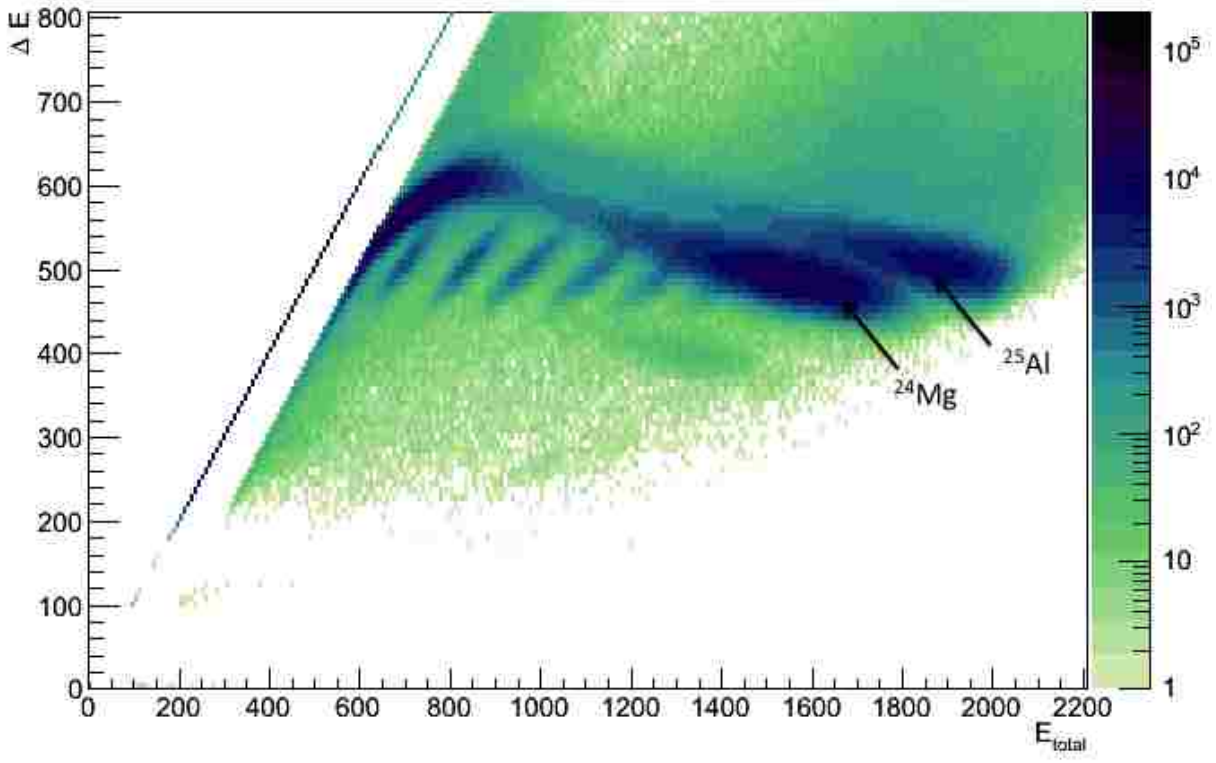

Figure 7.6. Energy recorded in the *ΔE* section of the gas ionization detector versus the total energy deposited, E_{total}. Axes show channel numbers.

number of high energy protons that punch through both silicon layers, seen as a folding of the proton group to lower *ΔE* and E_{total} for protons above 15 MeV, the maximum proton energy from elastic scattering. The higher energy protons from fusion evaporation reactions have a smaller *ΔE* than the protons of interest, but a total energy measured in silicon is lowered than their actual incident energy because they do not deposit all their kinetic energy into the silicon.

In addition there are protons from scattering of the beam upstream that enter into the silicon detectors at forward angles, but are not in coincidence with a heavy ion. These protons have about 11.4 MeV of energy. In Figure 7.7 we plot the energy spectrum of protons as identified in the gate in Figure 7.4 (blue curve). The ionization chamber *ΔE-E* plot is shown in Figure 7.8 for events that are in coincidence with these protons. The majority of heavy ion coincidences are ^{24}Mg and ^{25}Al that scattered off protons in the target, which have a lower energy than the unscattered particles.

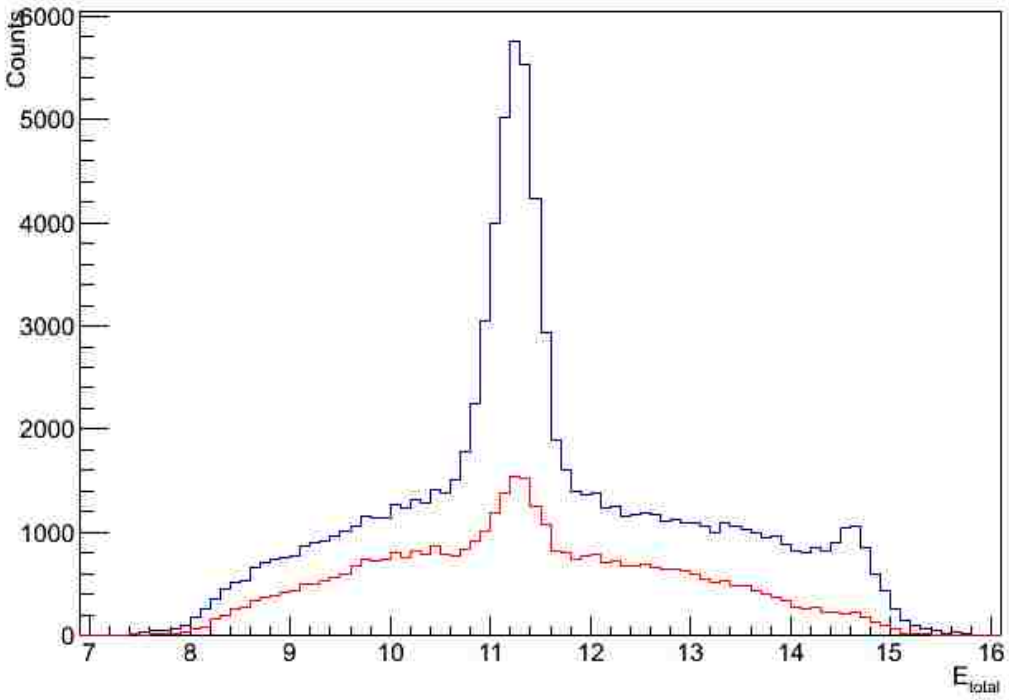

Figure 7.7. The total energy deposited in silicon for the events identified as protons (blue) and the same spectrum for events that have a recoiling heavy ion in coincidence in the gas ionization chamber (red).

However, there is also an intense group of particles with low energy (less than 400) in Figure 7.8 that likely correspond to very heavy ions in coincidence with fusion evaporation

protons that either stop in the *ΔE* or deposit very little energy in to the *E* section of the gas ionization detector.

In Figure 7.7 we also plot the spectrum of the same proton events that have a heavy ion in coincidence in the gas ionization detector (red curve). Besides the large spike near 11.4 MeV, the efficiency for heavy ion detection is relatively smooth. We plot the ratio between these two curves in Figure 7.9. The efficiency peaks at around 60%. This is less than the theoretical 85% expected efficiency due to the presence of fusion evaporation protons. For the high energy protons, the heavy ion coincidence efficiency is only 20% and the fusion evaporation protons

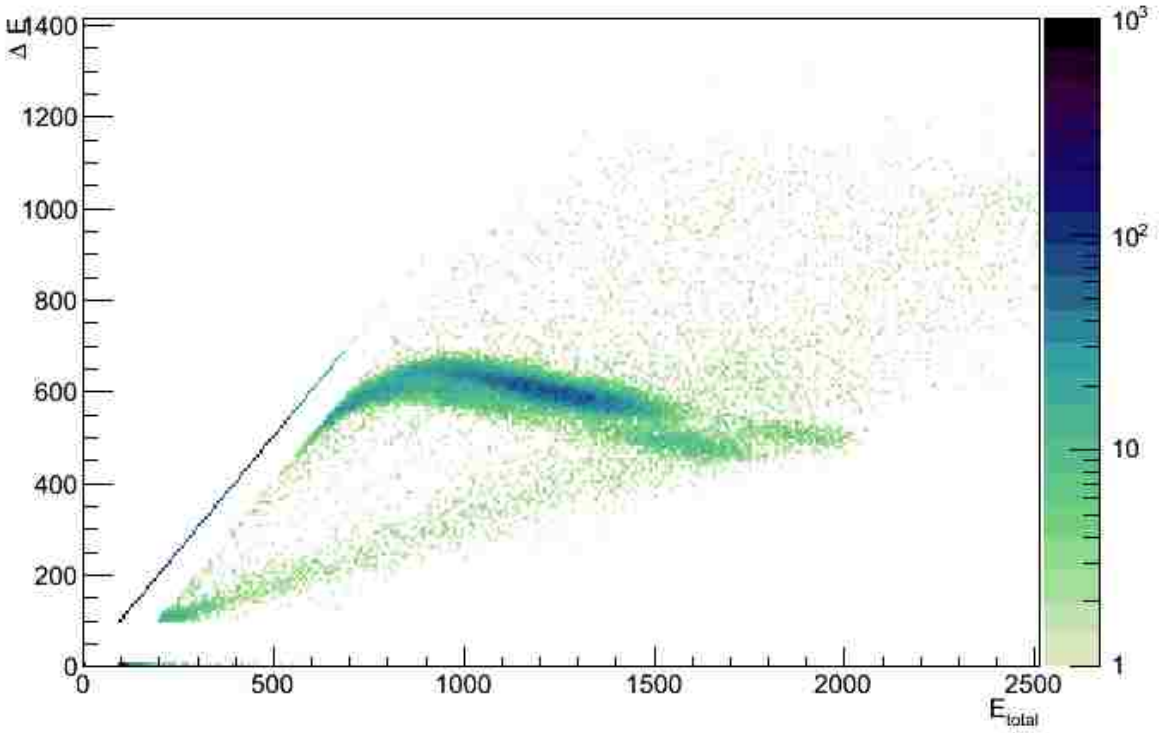

Figure 7.8. Ionization chamber particle identification plot *(ΔE-E)* for ions in coincidence with protons in the gate.

seem to comprise about 30% of the total protons. When this is taken into account, the efficiency for the gas ionization detector seems to be very close to the expected efficiency.

With the proton gate in the silicon array, the ionization chamber already allows quite clean identification of the ^{25}Al+p and ^{24}Mg+p scattering events, which are at lower energy than the unscattered beam particles since the scattering events have transferred some of the incident energy of the heavy ion to the proton. The intense spots on the far right side in the in Figure 7.6 and 7.8 are the unreacted ^{25}Al and ^{24}Mg beam in the ion chamber in random coincidence with events in the silicon.

Identification of the events of interest can be made even more definitive using the precise time structure of the beam. A linear accelerator operates in bursts, and is tuned to produce quite narrow time structure of the beam bursts hitting the target. A Time-to-Digital converter (TDC) was started using the logical "OR" from the silicon detectors and stopped with the RF timing

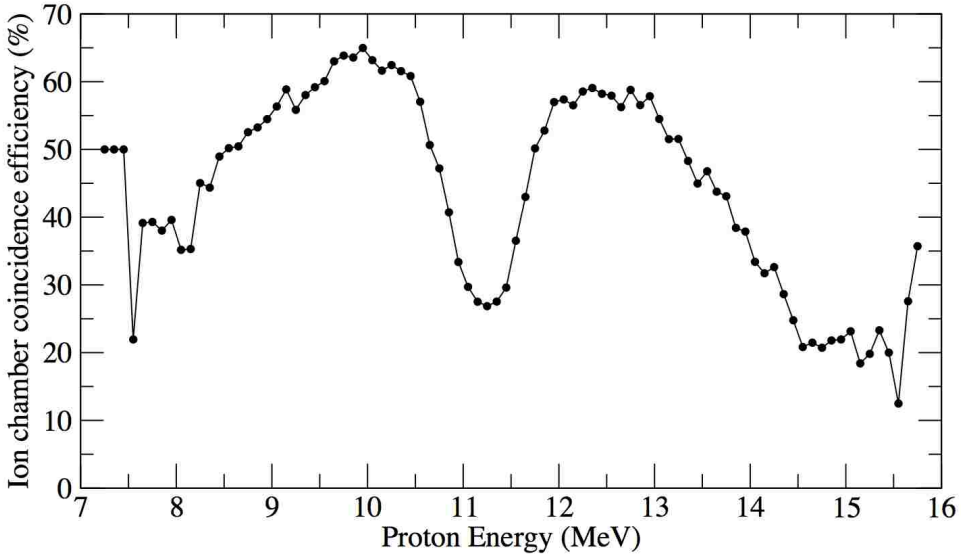

Figure 7.9. The ratio of the number of detected protons in silicon to the number that also have a heavy ion in coincidence in the gas ionization chamber.

signal from the accelerator. The raw timing spectra for all silicon events is shown in Figure 7.10 along with timing spectra for events that have a single proton in coincidence with a particle in

the aluminum band in the gas ionization chamber. Heavy ions of different species having the same magnetic rigidity have a different velocity and therefore a different time-of-flight. Scattering events also have a different timing than beam-like particles. Therefore, the relative timing between the silicon events and the accelerator RF further distinguishes the events occurring primarily due to ^{25}Al from the events due to ^{24}Mg or other random coincidences. Note that peaks in the red spectrum in Figure 7.10 do not align with any of the peaks in blue arising from the sampled beam.

Furthermore, the RF timing is so precise that ^{25}Al+p and ^{24}Mg+p reactions can be separated by time-of-flight. The RF timing spectrum gated on the protons in the Si detectors and on the ^{25}Al+p (blue) and ^{24}Mg+p (red) events in the ionization chamber are shown in Figure 7.11. The separation between the two groups in the ionization chamber is not entirely perfect: some ^{24}Mg+p is leaking into ^{25}Al+p gate and vice versa. However, using this RF timing

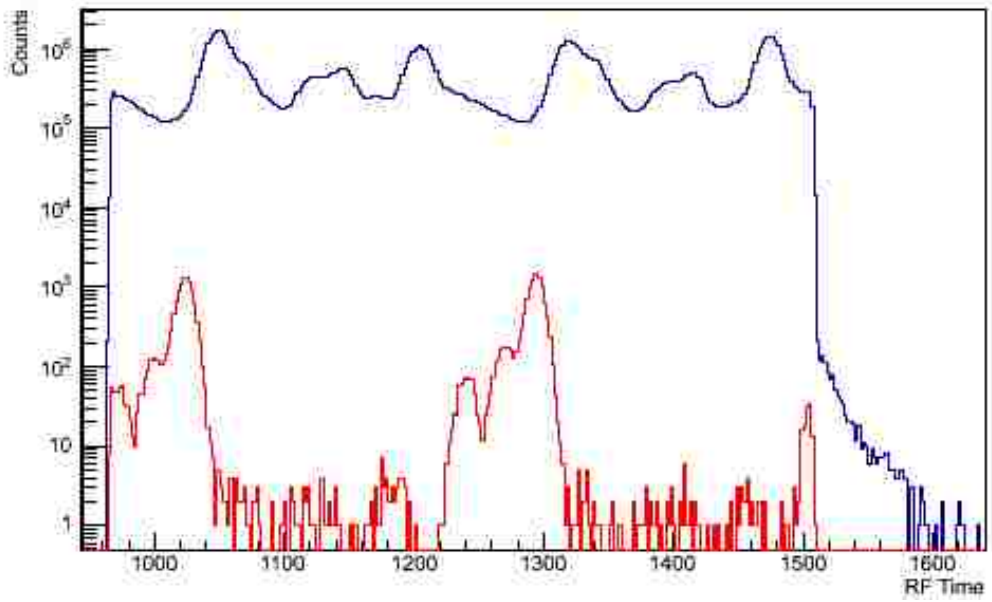

Figure 7.10. RF time raw (blue) vs. ^{25}Al+p selected events (red). RF time axis shows channel number.

spectrum, we can better discriminate ^{25}Al and ^{24}Mg events. We set a gate on the range of channels indicated in Fig 7.11 to select the ^{25}Al+p events. To illustrate the cleanliness of these cuts, it is instructive to make the RF timing cut and then look at the gas ionization chamber and silicon particle identification plots with this restriction, which are shown in Figure 7.12 and 7.13, respectively. With a particle identification gate on angle-correlated, single proton events, with RF timing selecting ^{25}Al+p scattering events, and ^{25}Al+p scattering selected in the ionization chamber particle identification plot, we achieve quite clean identification of ^{25}Al+p elastic scattering.

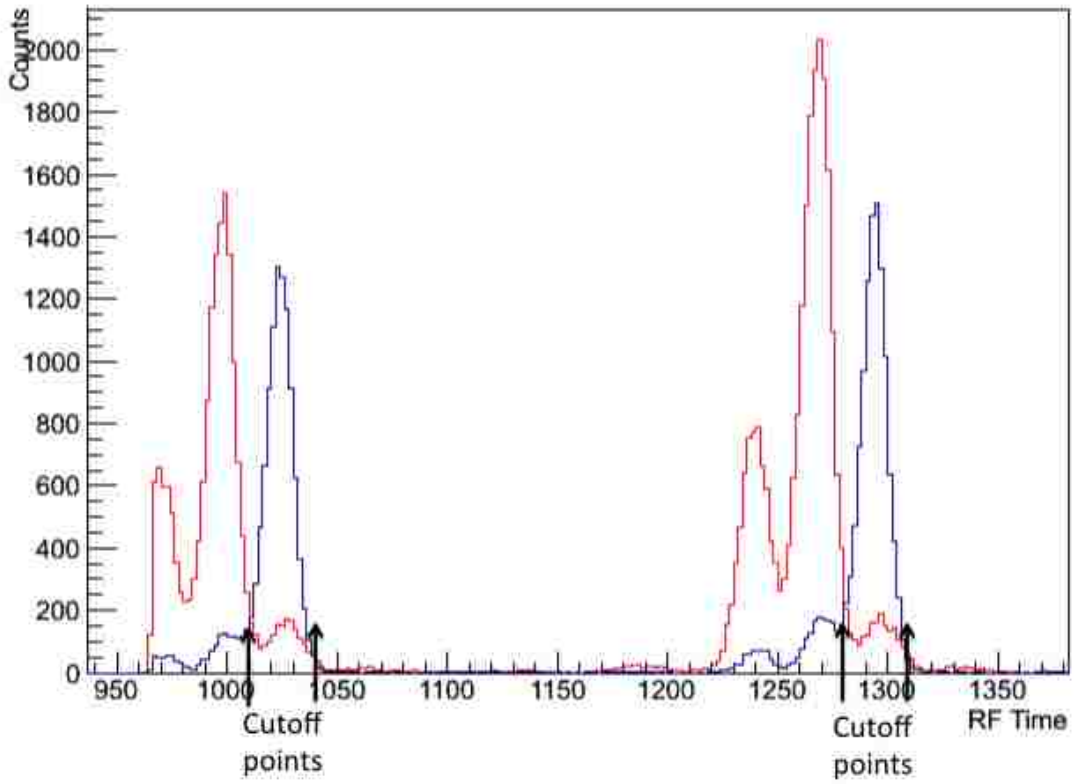

Figure 7.11. RF spectra gated on protons in the silicon and on ^{25}Al+p (blue) and ^{24}Mg+p (red) in the ion chamber particle identification plot. An RF timing gate is placed on the ^{25}Al+p peak, which rejects ^{24}Mg+p scattering that falls within the ^{25}Al+p gate in the ion chamber particle identification plot. The range of the RF (channel number) gates are shown with black arrows.

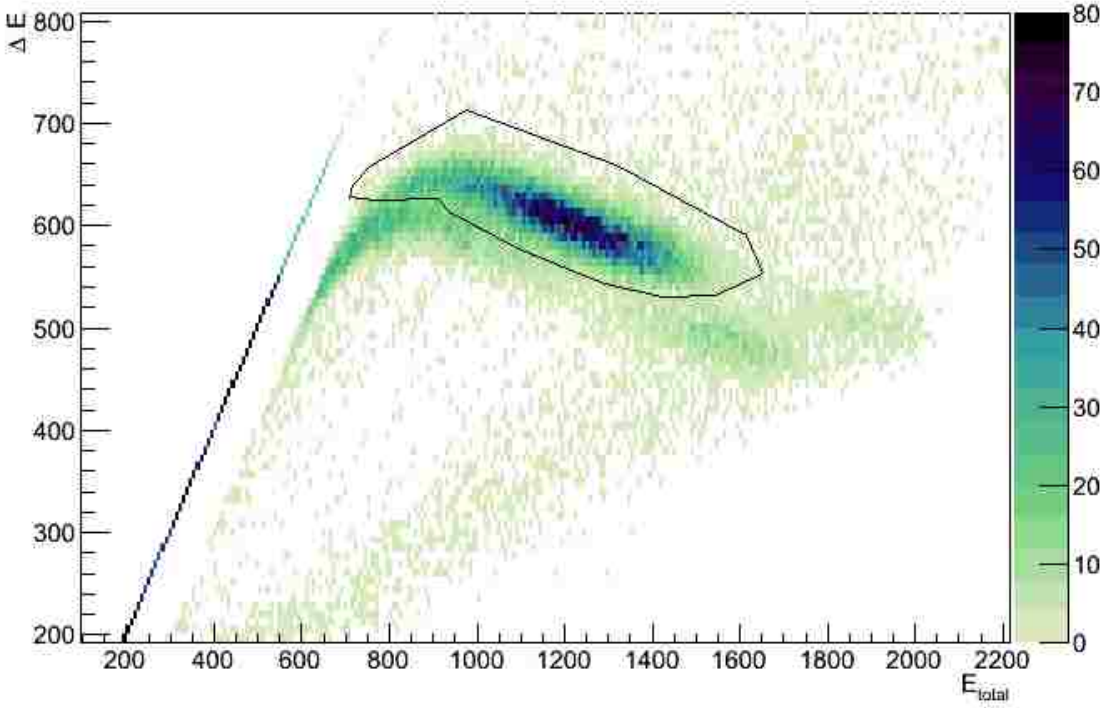

Figure 7.12. Particle identification plot from ionization chamber gated on single protons in the silicon and RF of the ^{25}Al+p scattering group.

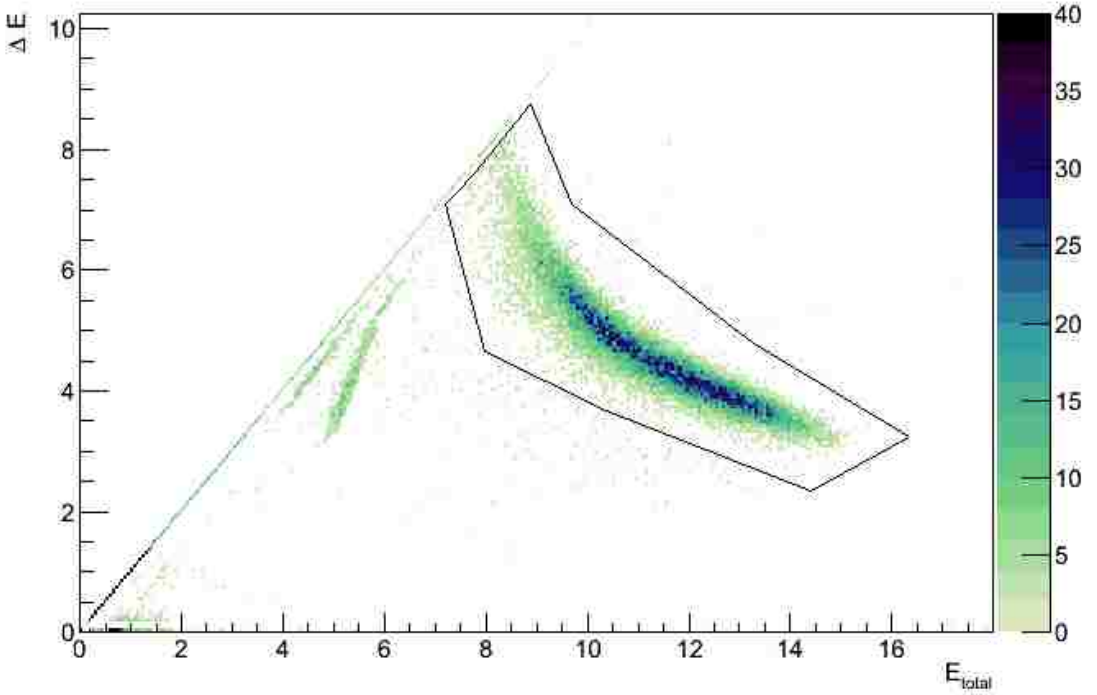

Figure 7.13. Particle identification plot from the Si detectors gated on RF of the aluminum group and on aluminum in the ion chamber.

The experiment was conducted over a long period of time (almost 2 weeks), and there were also some variations in beam quality and conditions over that time. Once the appropriate cuts were well defined to select events, we sorted the data from the experiment in blocks of a few hours time separately. We measured the beam intensity, composition, and the number of scattered protons and ^{25}Al ions. We also looked at the measured energy of the sampled beam in the gas ionization chamber to look for abnormalities that can arise from changing beam conditions, like magnet drifts or RF resonating cavities going out of lock. We selected events that were triggered by the ionization chamber to sample the incident beam particles, and we placed gates around the ^{24}Mg and ^{25}Al ions in the ionization chamber ΔE-E plot as illustrated in Figure 7.14. We examined the positions of the groups in the ionization chamber particle identification plot to see if there was any drift in beam properties or detector conditions (e.g. gas pressure). We found that there were no significant changes in the positions of the groups in the particle identification plot, indicating that the energy of the beam particles and the gas ionization detector response was relatively consistent.

Throughout the entire experiment, beam purity should stay the same. The ratio of ^{25}Al to ^{25}Al+^{24}Mg was also calculated for the groups of runs mentioned above taking the number of events of each species in the corresponding IC gates. The calculations show that the beam purity is on average 29% but somewhat varies from run to run, as summarized in Table 7.1 and Figure 7.15. The ratio of the number of the scattered protons in the ^{25}Al+p reaction to the number of the corresponding ^{25}Al ions detected in the ion chamber should be constant throughout the experiment. In order to check if this is the case, we also calculate the ratio of Al to p for groups of runs. These are also summarized in Table 7.1 and are plotted as a function of run in Figure 7.16. It turns out that for some of these runs this number is not entirely consistent. Changes in the

beam may be due to the variable operation of LINAC resonators. These outliers were taken out of the subsequent data analysis.

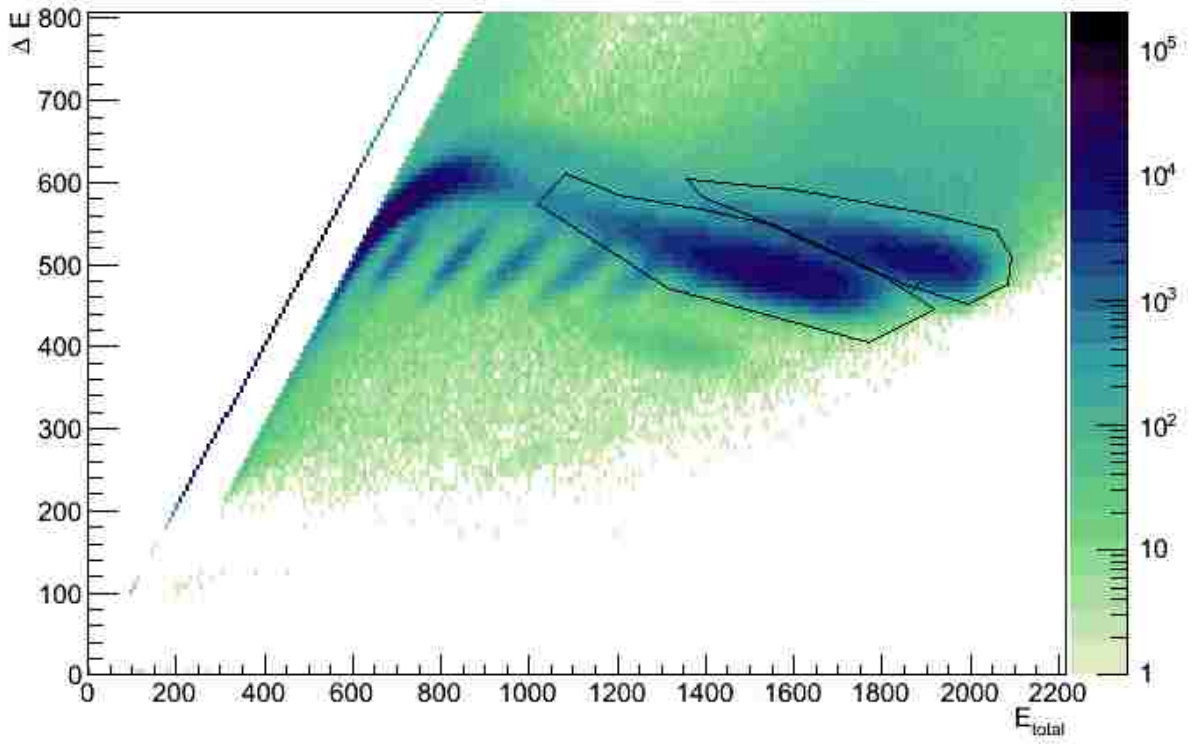

Figure 7.14. An example of the ionization chamber particle identification spectrum for events triggered by the ionization detector showing gates that were placed on the ^{25}Al and ^{24}Mg beam groups to monitor the energy, intensity and purity of the beam.

Table 7.1. Beam purity and ^{25}Al/p ratio for the runs. Consistency of the beam purity and the Al/p ratio was checked throughout the experiment. Seven individual runs were excluded from the analysis because the Al/p ratio was less than 50 and statistically inconsistent with the other runs. These outliers are highlighted in red.

Run number	Al/p	Beam purity, %
3367-73	63.6	32
3374	67.3	32
3375-81	65.9	31.2
3382-87	64.4	28.6
3388-96	61.9	31.5
3397-99	65.2	30.3
3400-05	63.5	29.3
3406-08	63	27.4
3409-14	64.9	28.2
3415	**24.2**	**29.5**
3420-28	64.2	26.8
3430-34	65.8	30.2
3436-40	64.8	28.6
3441	65	29
3442	62.1	24.7
3443	61.9	28.1
3444	**30.6**	**29.5**
3445	**49.8**	**30**
3446-49	66.6	27.6
3452-57	62.8	26.1
3459	**21**	**27.5**
3460	**47.9**	**31.2**
3461	**15.78**	**27.4**
3462	**25.1**	**27**
3464-67	60.7	23.8
3475-78	59.8	28.8
3479-80	70.6	32.8
3481-85	66.3	30.1
3488-91	69	32.6
3498-3502	64.7	27.7
3503-3514	63.9	31.6

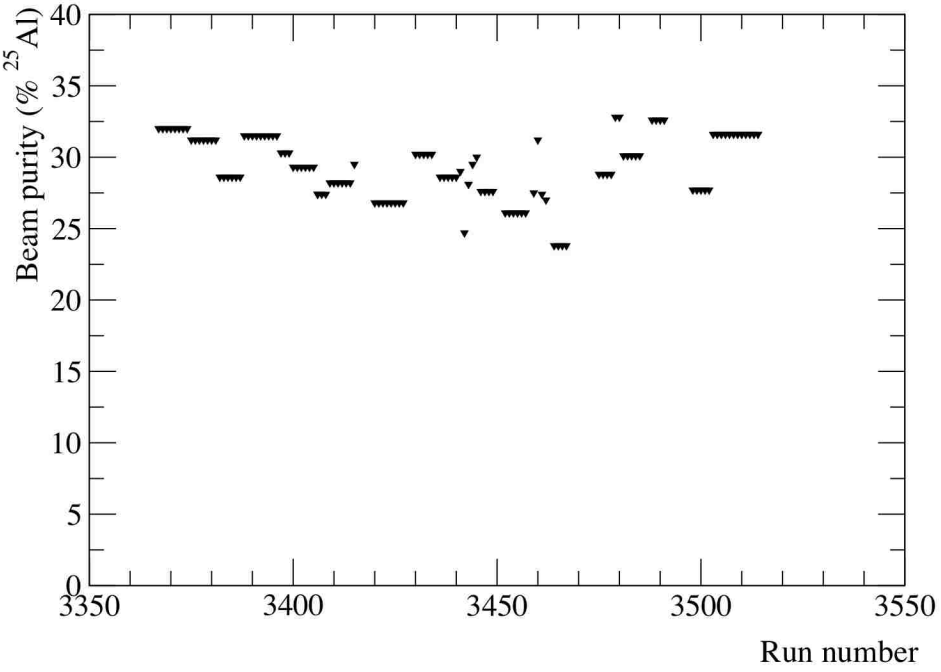

Figure 7.15. Beam purity calculated throughout the experiment for different sets of runs.

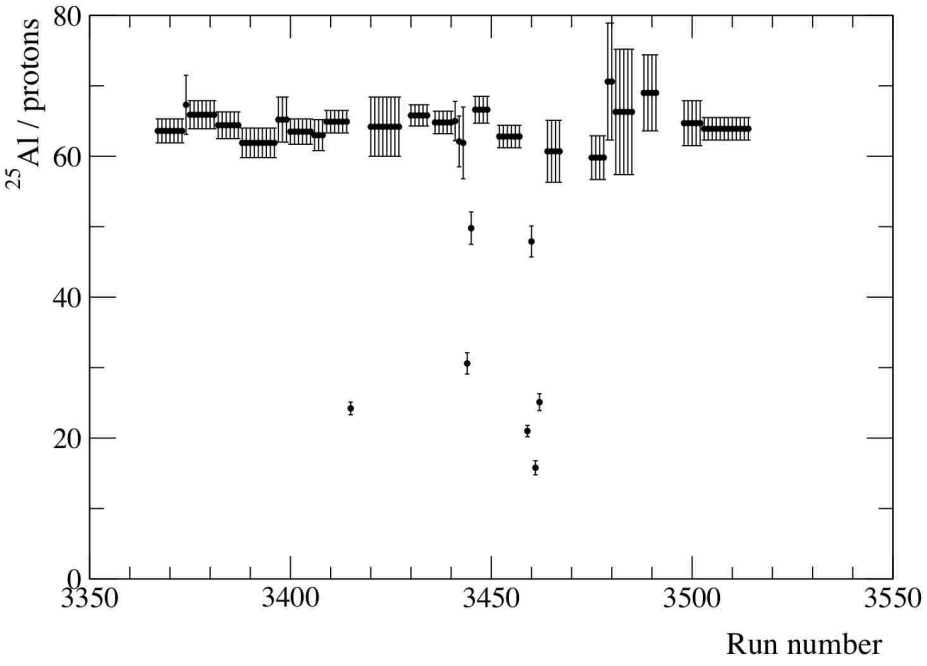

Figure 7.16. Ratio of ^{25}Al to protons checked throughout the experiment. Runs were grouped, and the respective data points represent groups of runs. The outliers were excluded out of the subsequent data analysis.

CHAPTER 8. THE ^{25}AL+P EXCITATION FUNCTION

With a clean selection of ^{25}Al+p scattering events, we can reconstruct the energy dependence of the differential cross section using the measured proton energy and angle. The energy calibration was an important aspect of this experiment since the measured proton energy in the silicon detector is used to reconstruct the center-of-mass energy on an event-by-event basis, and our goals are to accurately determine excitation energies and widths for observed resonances. We determine the energy detected by the silicon strip detectors using the segments on the back of the silicon strip detectors. The calibration of the Si detector array was done with a calibrated pulser (to determine zero offset) and with a ^{228}Th α source. The ^{228}Th source's 5.685, 6.288, 6.778, and 8.785 MeV decay lines were used to calibrate the energy spectrum for the segments of each silicon detector. A sample energy spectrum from the calibration is shown in Figure 8.1.

To extract the centroid channel, we performed a Gaussian fit to each of the peaks corresponding to alpha-decay lines used in the calibration. A linear fit of the known

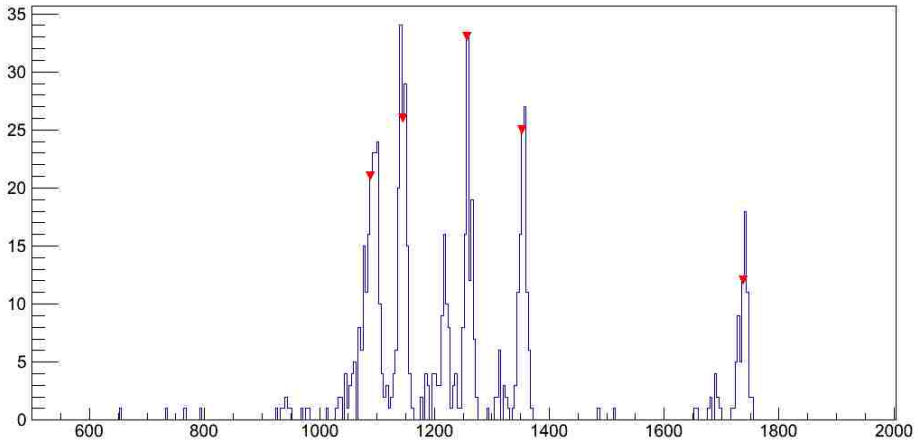

Figure 8.1. Sample energy spectrum taken with the ^{228}Th calibration alpha source.

energy to centroid channel was then performed to extract linear calibration coefficients for each signal of the detector. A small correction was also applied for the energy loss of the alphas in the dead layer of the silicon detectors. In our case the dead layer of the S2 detectors is about 0.5 μm thick. Previous measurements have shown the energy loss in the dead layer on similar detectors to be about 70 keV for 5 MeV alphas. We include a dead layer of this thickness, and the energy dependence of the energy loss in the dead layer improved the fit to the measured centroids as a function of energy For the protons of interest for this experiment that require on the order of 1 mm of silicon to stop, this small dead layer makes a negligible change to the energy of the protons. Its effect on the alpha particles does alter the energy calibration for the detected protons by less than 100 keV.

Since the laboratory angle is well determined from the position in the silicon, with perhaps only a very small correction for the misalignment of the beam (discussed later), the center-of-mass energy of each event can be reliably reconstructed. The measured energy of the protons does have to be corrected for energy loss in the target, but this is a small correction given the small stopping power for protons. This correction is applied by first calculating ^{25}Al beam energy that would produce protons of the measured energy. The energy of the ^{25}Al is then used to determine the depth in the target at which the scattering took place, and the remaining target thickness is then used to calculate a correction for the energy loss of the protons in exiting the target. The measured proton energy is then corrected for the energy loss in the target, and the corrected energy is used, with the measured laboratory angle, to then calculate the final center of mass energy at which each scattering event occurred. The maximum correction for the energy loss of

protons scattered from the entrance to the target is 82 keV (0.6% of the proton energy). At the middle of the target the correction drops to less than 0.4% of the proton's energy.

After correcting for the energy loss in the target, the proton energy in the lab frame is converted into the center-of-mass frame using energy and momentum conservation. Knowing the energy of the scattered proton in the lab frame and its angle with respect to the beam direction, we can calculate the proton energy in the center of mass in inverse kinematics as:

$$E_{cm} = \frac{M + m}{4M \cos^2 \theta_{lab}} E_{lab}$$

where M is the mass of ^{25}Al and m is the mass of the scattered proton. θ_{lab} is the scattering angle between the proton's scattering direction and the beam direction. As argued, only the measured energy and the laboratory scattering angle are needed to extract the center-of-mass energy resolution. This is done on an event-by-event basis to the selected ^{25}Al+p scattering events, and we plot in Figure 8.2 the number of counts observed vs. the center-of-mass energy at which the scattering took place. In Figure 8.3 we show these same events, but with the center-of-mass energy plotted versus the laboratory angle.

From the measured number of counts as a function of the center-of-mass energy, we can construct the differential cross section as a function of energy (and angle). The differential cross section dσ/dΩ for each energy bin E_i is determined by:

$$\frac{d\sigma(i)}{d\Omega} = \frac{Counts(i)}{I * \Delta\Omega * [atoms/cm^2(i)]}$$

Here, I is the total number of incident ^{25}Al ions determined by the number of ^{25}Al beam events in those events triggered by the gas ionization detector multiplied by the factor of

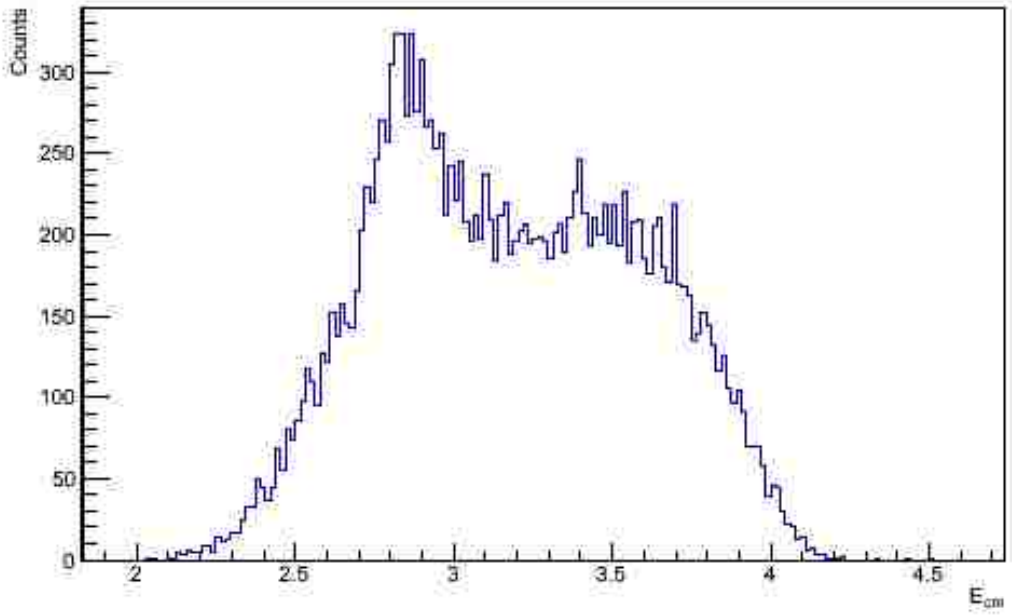

Figure 8.2. The number of events selected as ^{25}Al+p scattering as a function of the reconstructed center-of-mass energy.

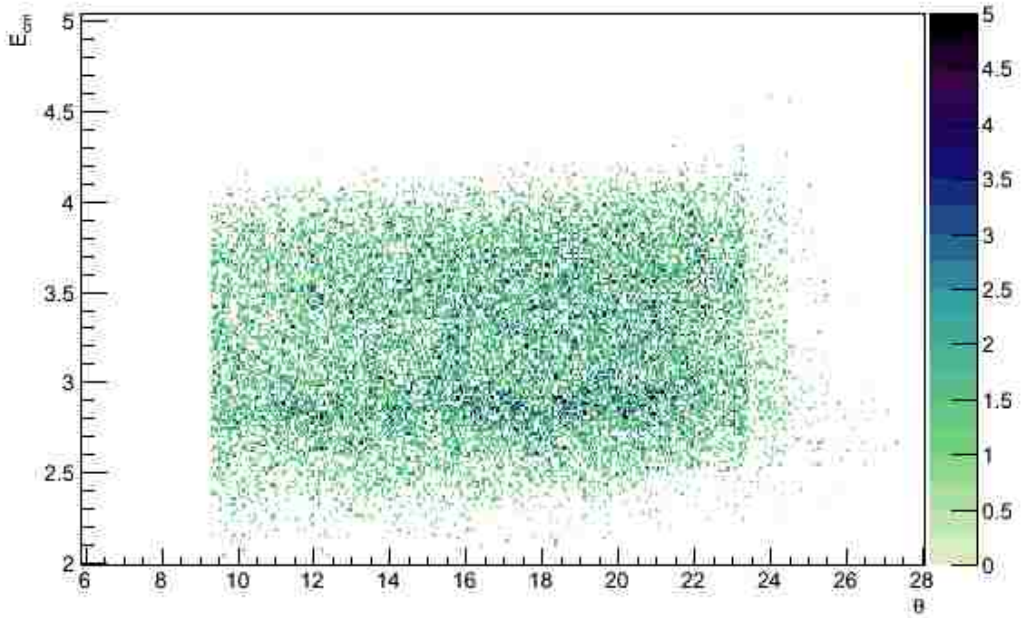

Figure 8.3. E_{cm} vs. theta angle in Si detectors.

1000 downscaling of events. The solid angle, DW, is determined by the well-defined geometry of the silicon strip detectors. The number of atoms/cm^2 is then determined by:

$$\frac{atoms}{cm^2} = \frac{\delta E}{stopping\ power} * \frac{26.0078}{1.0078}$$

where *dE* is the energy width of each bin the center-of mass, and the laboratory stopping power for ^{25}Al was calculated using LISE++, 26.0078 and 1.0078 are masses of the ^{25}Al ion and the proton, respectively.

The calculated differential cross section (in the center-of-mass frame) is plotted versus center-of-mass energy in Figure 8.4. The overall normalization of the cross section we measure is about a factor of 2 lower than expected. In Figure 8.4 we also show the calculated cross section with no resonances, in this case multiplied by 0.6. The reason for this discrepancy is not yet understood. However, most important is the energy dependence of the cross section that is sensitive to the properties of resonances corresponding to states in ^{26}Si. In fact, the measured excitation function shows some statistically significant structure, especially one strong resonance near E_{cm}=2.8 MeV that is close in energy to a previously reported resonance in ^{25}Al+p elastic scattering [Che12].

At higher center of mass energies, the resonances become broad and overlapping. A broad resonance is a resonance where $\frac{\Gamma}{E_R} \geq 10\%$. For such resonances, energy cannot be treated as a constant, and the reaction rate $< \sigma v >$ takes into account the fact that the cross-section is dependent on the energy. From the Breit-Wigner formula it can be seen that if a nuclear reaction A(a,b)B takes place, $\sigma_n \sim \Gamma_a \Gamma_b$ thus an elastic scattering reaction A(a,a)A also can take place, with $\sigma_e \sim \Gamma_a \Gamma_a$.

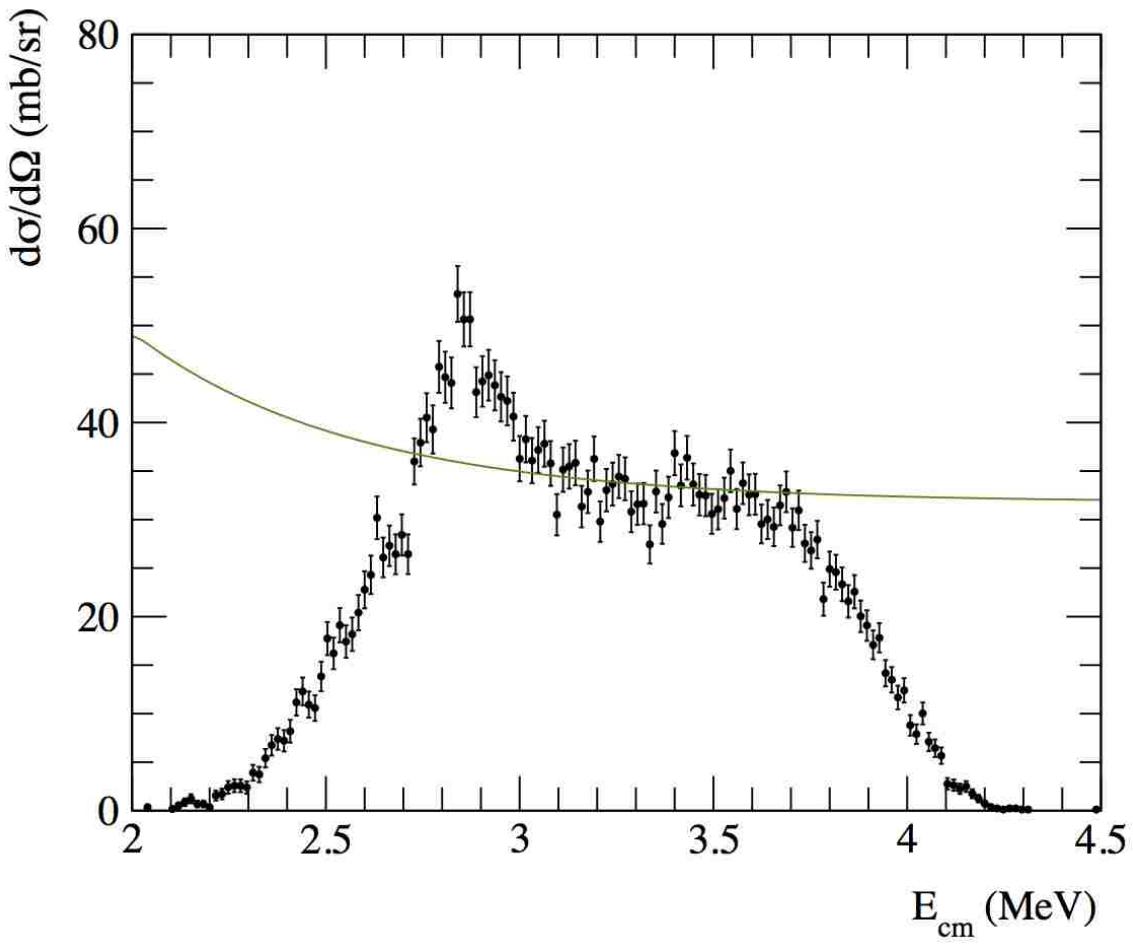

Figure 8.4. Measured differential cross section in the center-of-mass frame as a function of center-of-mass energy (data points) compared to calculated nonresonant cross section multiplied by 0.6 (solid green curve).

The ratio of cross-section between the two reactions can be given by $\frac{\sigma_n}{\sigma_e}$. Usually it's the case that $\sigma_e \gg \sigma_n$. In such cases, the single-level Breit-Wigner approximation applied in the ^{32}Cl case can be used.

Phenomenological R-matrix theory is a nuclear interaction model that describes nucleon-nucleus interactions and predicts experimental cross-sections. While many nuclear models describe properties of the interacting nuclei using nuclear forces (nuclear potential), the R-matrix theory treats a nucleus participating in a collision as a black box since the nucleus is a complex

structure and the exact details of nuclear forces within the nucleus are not known. In other words, the behavior of the wave function inside the nucleus cannot be calculated directly from the Schrödinger equation. This theory takes characteristics of the nucleus as parameters in the R-matrix that can be determined by analyzing the interaction cross-section, measured in an experiment.

In the R-matrix analysis the inner nucleus wave function of the angular momentum l is expanded in a linear combination of the eigenfunctions of the energy levels in the compound nucleus.

R-matrix is defined as:

$$R_{cc'} = \sum_{\lambda} \frac{\gamma_{\lambda c}\gamma_{\lambda c'}}{E_{\lambda} - E}$$

where $\gamma_{\lambda c}$ is the reduced width amplitude for a level and the corresponding entrance channel c and the exit channel c':

$$\gamma_{\lambda c} = \sqrt{\frac{\hbar^2}{2m_c a_c}\phi_c\left(E_{\lambda}, a_c\right)}$$

Both $\gamma_{\lambda c}$ and E_{λ} are unknown parameters. Then, knowing the R-matrix parameters we can compute the cross-section for the elastic scattering as:

$$\sigma_r = \pi\lambda^2 \sum_{l}\left(2l+1\right)|1-U_l|^2$$

where U is a collision matrix. To analyze the influence of resonances on the differential cross section, we calculate theoretical cross sections using the R-matrix code MULTI that has been widely used to describe proton elastic scattering data [Ne185].

We plot our measured cross sections in comparison to a R-matrix calculation where we adopt the resonance energies and widths from [Che12] in Figure 8.5 (blue curve). The theoretical cross section has been multiplied by a factor 0.5. The energy of the resonance we observe at $E_{cm} = 2.8$ MeV agrees reasonably well with that previously observed in [Che12]. The calculated cross section also gives a fair description of the energy dependence of the cross section at higher

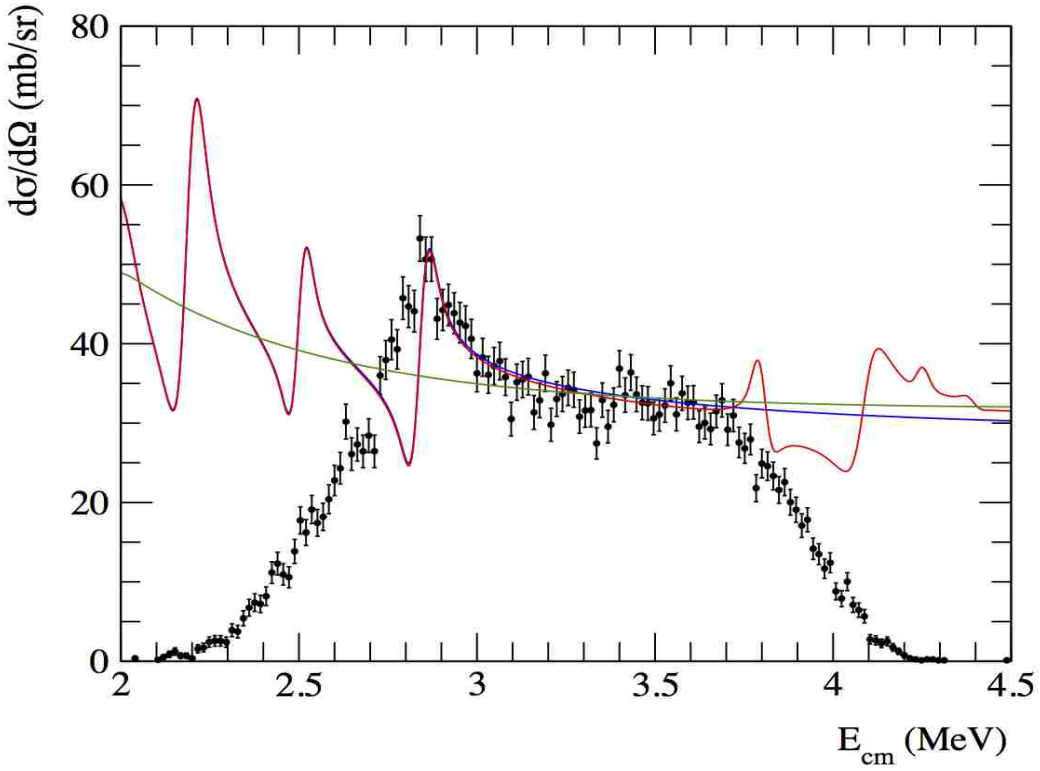

Figure 8.5. Measured differential cross section is compared to R-matrix calculated cross sections using no resonances (green curve), using the measured resonance parameters from [Che12] (blue curve) and using both the resonances from [Che12] and [Mat11a] (red curve). The theoretical blue and red curves have been normalized by a factor of 0.5.

energies when no resonances are included. This provides evidence that there are no strong s-wave resonances in the energy range from 2.9 to 3.7 MeV.

One of the goals in this measurement was to extend the elastic scattering cross section to energies above the alpha threshold and to cover the resonance energies reported in the ^{28}Si(p,t)^{26}Si reaction [Mat11a]. We also plot in Figure 8.5 the calculated cross section where we include the 4 resonances reported by [Mat11a] (red curve). In addition to the resonances at lower energies of [Che12]. The properties of these resonances are summarized in Table 8.1. Proton partial widths for the states above 9 MeV are unknown. For this calculation, we set the protons spectroscopic factor for these levels to 0.06, which is the average of the value reported for resonances observed in [Che12]. This is likely an over estimate since the levels observed in

Table 8.1. Properties of the states used in the R-matrix calculated cross-sections. For states with Ex < 8.4 MeV, resonance energies and widths are adopted from [Che12]. For states with Ex > 9 MeV, we include resonance states reported in [Mat11], and we assign partials widths using a spectroscopic factor of 0.06, the average value from the observed resonances of [Che12].

E_x (MeV)	J^p	E_{cm} (MeV)	ℓ -value	P_ℓ	q_{sp}[a]	G_{sp} (keV)	G_p (keV)
7.162	2^+	1.648	s	0.094	0.55	180	7
7.402	2^+	1.888	s	0.14	0.55	280	6
7.484	2^+	1.970	s	0.16	0.55	320	46
7.704	3^+	2.190	s	0.20	0.55	400	41
8.015	3^+	2.501	s	0.27	0.55	530	15
8.356	3^+	2.842	s	0.33	0.55	650	27
9.316	4^+	3.802	d	0.105	0.36	140	8
9.605	2^+	4.091	s / d	0.51 / 0.13	0.55 / 0.36	1000 / 170	60 / 10
9.762	5^-	4.248	f	0.35	0.35	33	2
9.903	0^+	4.389	d	0.36	0.36	190	11

[a]From C. Iliadis, Nucl. Phys. A 618, 166 (1997).

[Che12] are only the strongest s-wave resonances and are not representative of the full distribution of states in the energy region.

The energy dependence of our measured cross section in the region of the 2.8 MeV resonance does not agree with calculations using the previously reported resonance parameters [Che12]. The structure that we observe is broader than described by the calculated cross section that includes Gaussian smearing of the calculated cross section with FHWM of 40 keV, see Figure 8.6, which was found to provide good agreement to the energy resolution in a similar

elastic scattering measurement using the same experimental setup [Pra14]. However, the measured cross section also decreases rather slowly with energy at the upstream and downstream ends of the target, which is unexpected and limits our ability to search for resonances up to the full incident energy corresponding to $E_{cm} = 4$ MeV. If this effect arises from poor incident beam energy resolution, it would have little effect on the width of resonance structures observed since the proton energy loss in the target is so small and the location of resonances in the target have

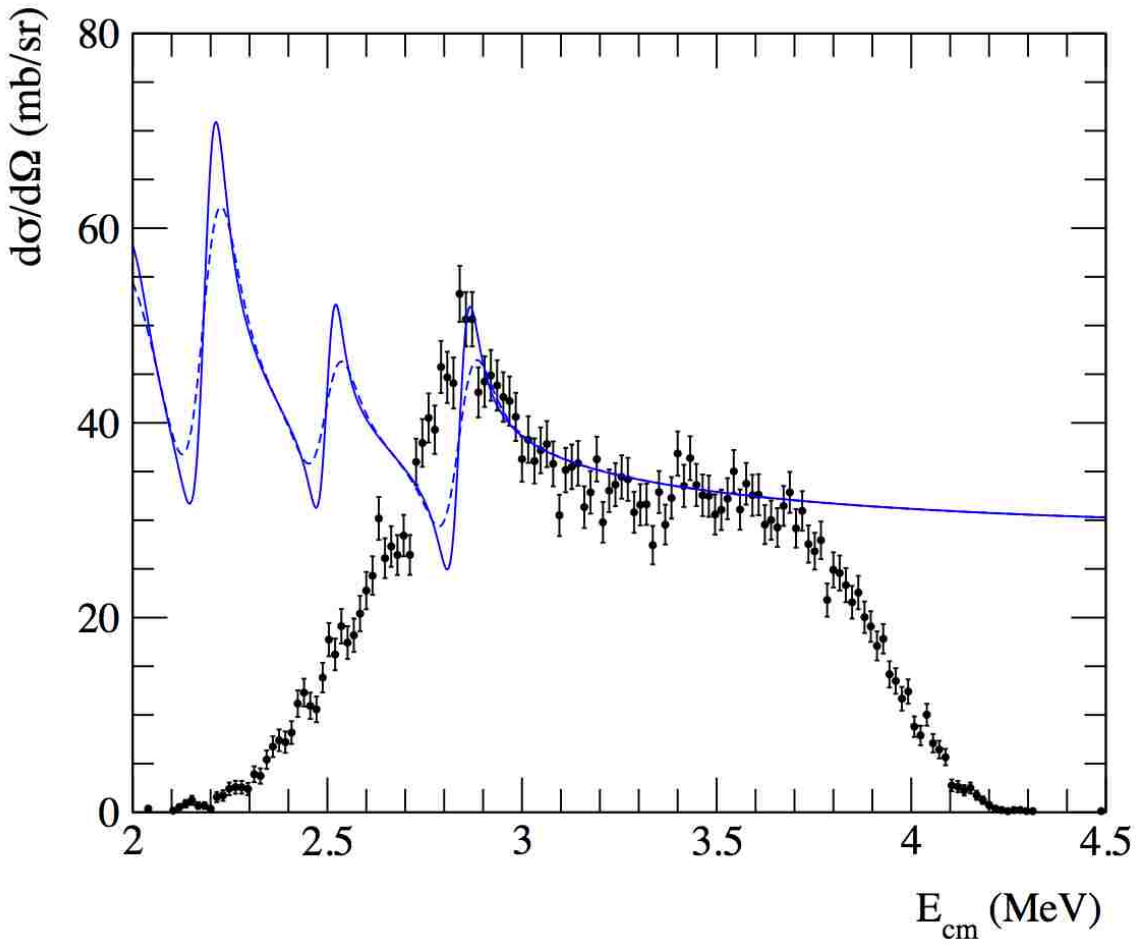

Figure 8.6. Measured differential cross section is compared to R-matrix calculated cross sections using the measured resonance parameters from [Che12] with 40 keV and (solid blue curve) and 80 keV (dashed blue curve). Gaussian smearing of the calculated cross section.

little effect on the reconstructed center-of-mass energy. However, angular resolution or energy straggling could make the energy resolution worse than previously observed, see Figure 8.7.

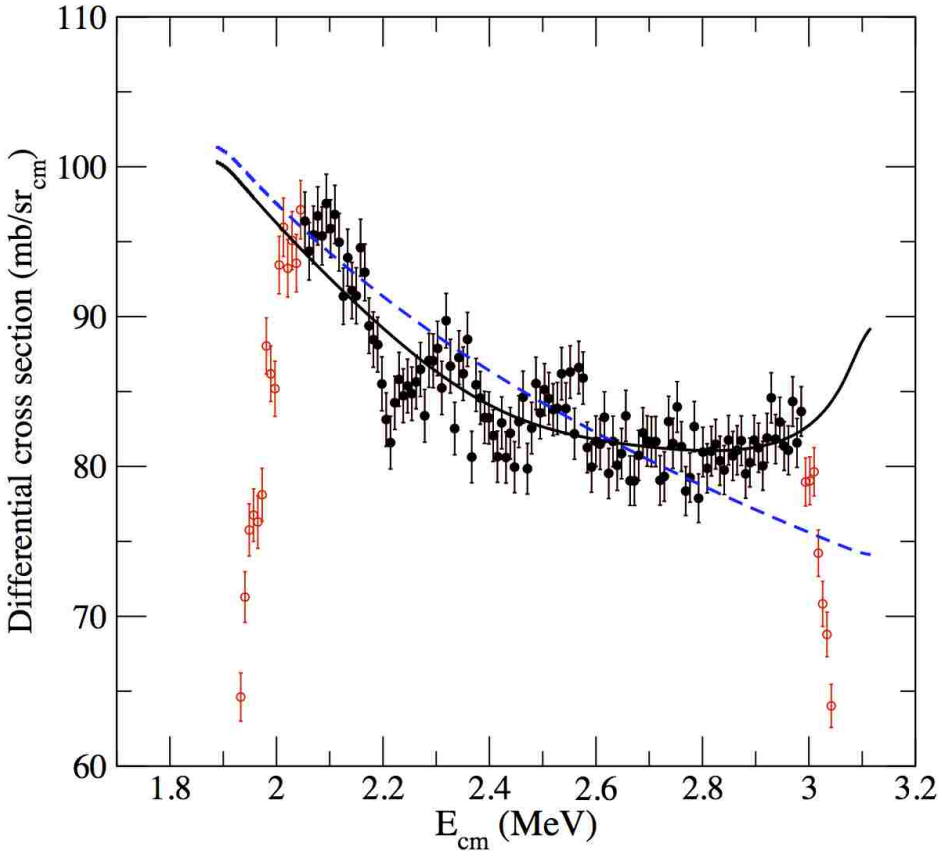

Figure 8.7. Cross-section vs. E_{cm} in ^{17}F+p elastic scattering experiment taken from [Pra14]. The shape of the cross-section is different from what we observe in our experiment.

We attempted to reproduce the width of the 2.8 MeV resonance by introducing increased smearing of the calculated cross section. In Figure 8.6, we compare the measured cross section to calculations using 40 keV and 80 keV Gaussian smearing of the cross section. Increasing the smearing of the cross section, while making the resonance structure wider, simultaneously decreases the amplitude of the resonance structure. To achieve a reasonable fit to the resonance would require a much greater proton partial width in addition while the smearing is increased

significantly in order to describe the energy dependence of the observed cross section, such a large proton width is not consistent with the results of [Che12] and seems unreasonable.

There are indications that we may observe other narrower resonance structures in the data in the energy range between 3.2 and 3.7 MeV. There are at least 3 states that have been previously observed in the mirror nucleus in this energy range that have been assigned spin-parity of 2^+. In Figure 8.8 we show a calculation for the cross section where we have included two 2^+ resonances at 3.39 and 3.53 MeV that have *s*-wave partial widths of 8 and 3 keV respectively, which gives an improvement in the fit to the data and may be evidence for narrow resonances in this energy region. However, a detailed fit to extract possible weak resonance

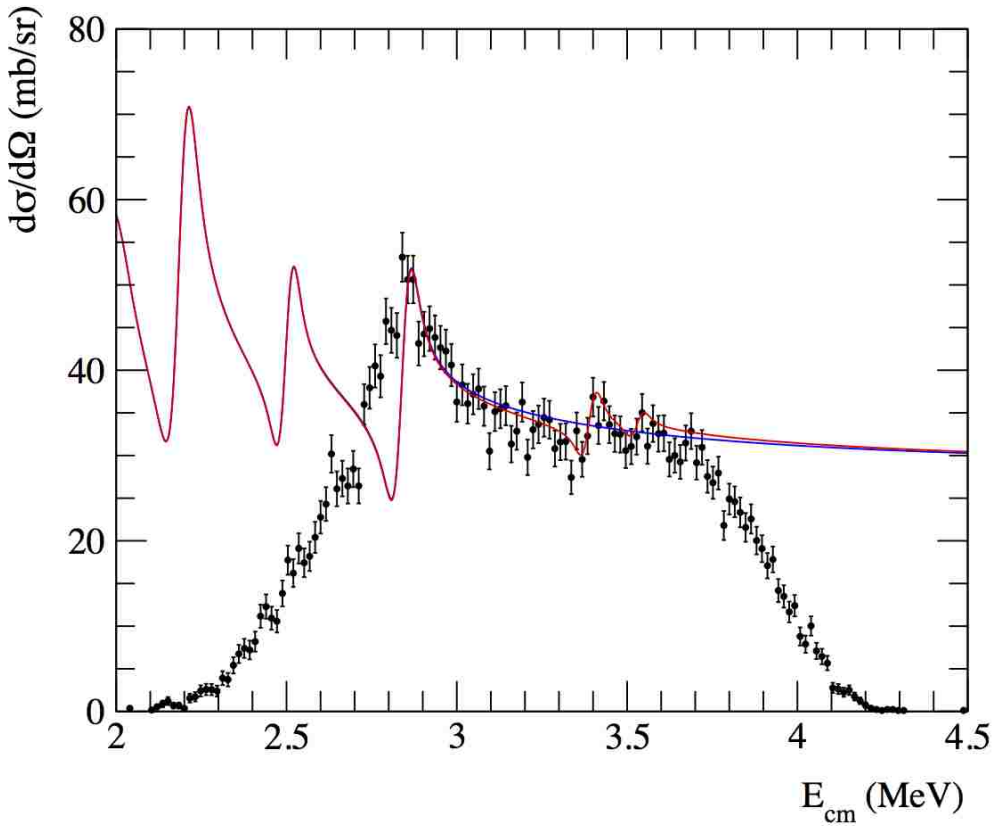

Figure 8.8. Measured differential cross section is compared to R-matrix calculated cross sections using the measured resonance parameters from [Che12] (solid blue curve) and including additional 2^+ resonances at 3.39 and 3.53 MeV with *s*-wave proton partial widths of 8 and 3 keV respectively.

parameters cannot be done until we arrive at a better understanding of the energy dependence in the region of the strong 2.8 MeV resonance, and the apparent poor resolution at the highest and lowest energies.

One other piece of information that could provide some information on the structure observed around E_{cm}=2.8 MeV is the angular distribution. In Figure 8.9 we plot the angular distribution of the differential cross section for a ΔE_{cm}=160 keV wide bin of energies around the peak of the resonance. In this plot we also compare the measured angular distribution to the calculated distribution using the resonance parameters from [Che12]. The calculated cross section has been multiplied by a factor of 0.42 to be normalized to the data.

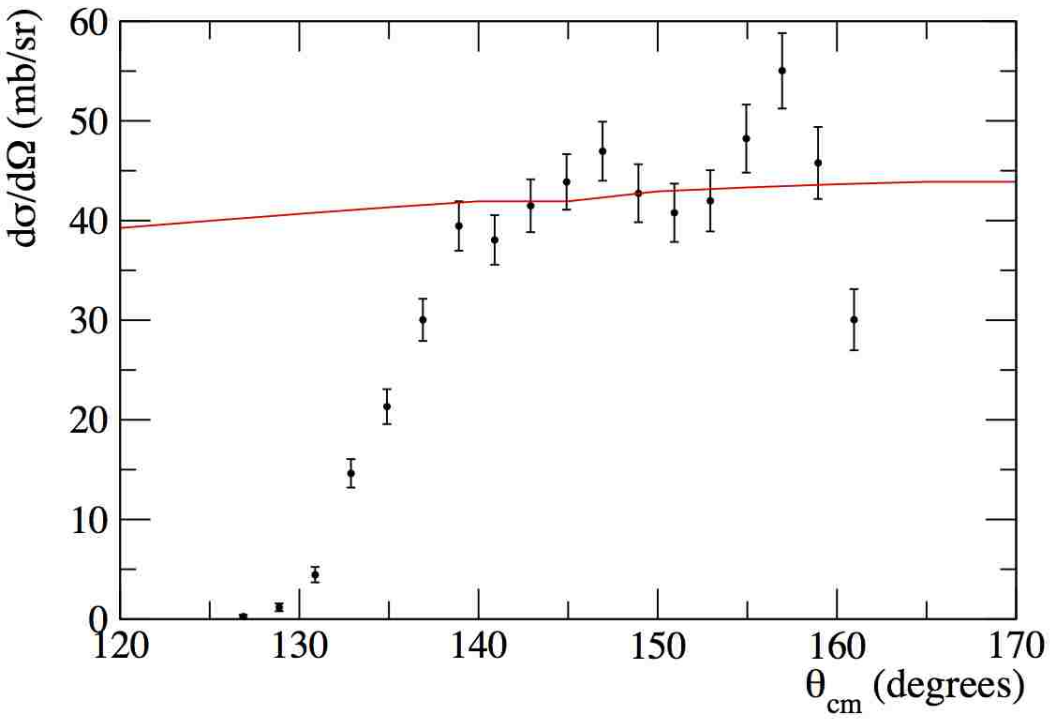

Figure 8.9. Angular distribution of the differential cross section near the peak of the 2.8 MeV resonance compared to R-matrix calculated cross sections using the measured resonance parameters from [Che12] (solid blue curve). The R-matrix calculation has been normalized by a factor of 0.42.

The beam energy resolution is defined by slits at the RESOLUT focal plane that define the acceptance, which can be from 0.5% to 1% of the incident energy of the beam. For this experiment a larger slit setting was used that is expected to result in 1% resolution for the incident energy. The energy spread of the incident beam would only affect the lowest and highest E_{cm} covered since the proton energy loss in the target is so small, but the energy dispersion observed is much larger than the expected 1%. The energy resolution of the beam also has very little affect on the energy dependence of the cross section near the 2.8 MeV resonance, which is near the downstream side of the target. However, the emittance of the beam, angular straggling, and simple misalignment of the beam could possibly explain the energy dependence of the cross section near the 2.8 MeV resonance as well as the poor resolution at the lowest and highest center-of-mass energies.

In a previous measurement of ^{17}F+p elastic scattering at RESOLUT using a similar setup, it was found that the beam axis was not well aligned to the detector axis, which caused some degradation in resolution [Pra14]. Misalignment of the beam on the axis of the silicon detectors can be tested by looking at the measured energy of particles as a function of the azimuthal (φ) angle, which in this case is proportional to the segment number on a given silicon detector. If the beam is positioned at the axes of the Si detectors, there should be no energy dependence on the azimuthal angle. If there is the φ dependence, it may mean that the beam was misaligned. In Figure 8.10 we plot reconstructed E_{cm} for ^{25}Al+p events versus the azimuthal φ angle. Some slight waviness in the data, i.e. a dependence of E_{cm} on φ is observed. We introduced a correction for this by introducing an x_0 and y_0 offset parameters in the data analysis code that adjusts the mean position of beam at the target position relative to the silicon array. We adjusted the x_0 and y_0 offset parameters and calculated polar (θ) and azimuthal (φ) angles knowing the

segment and ring number for each event. Introducing a slight offset to the beam may have slightly improved the azimuthal dependence, but it is difficult to optimize by the energy dependence on the azimuthal (φ) angle, and it seems clear that an adjustment of the mean position will not contribute to the resolution at the level observed in the data.

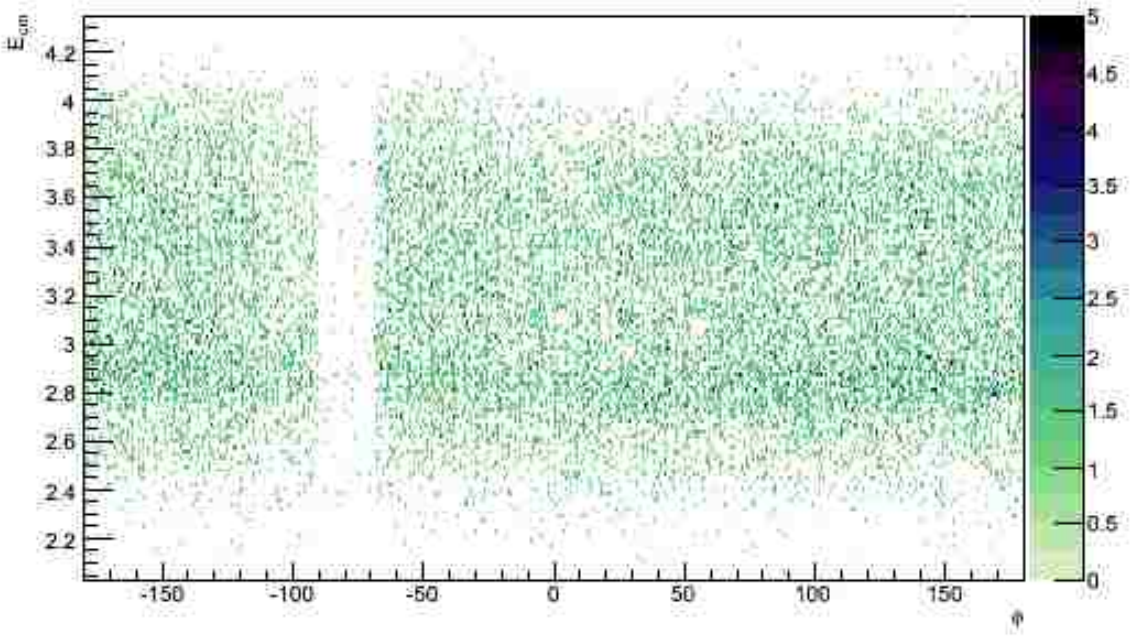

Figure 8.10. The reconstructed E_{cm} for ^{25}Al+p events is plotted versus the azimuthal angle of the detected proton. One can see the waviness in the spectrum.

It is most likely that the angular emittance of the beam compounded by straggling in the target is giving rise to the significant degradation in our reconstruction of E_{cm}. There is hope to correct this effect by using the new position dependent capability of the gas ionization detector that was introduced for this experiment. The x and y positions of each heavy ion are measured upon entering the counter with a resolution of better than 3mm. In Figure 8.11 we plot the position (y vs. x) of ^{25}Al ions that were measured in coincidence with protons. The scale of the

plot is by wire number, with the separation between wires being 3mm. The large spread in positions in the ionization chamber is much larger than there would be if the beam had perfect emittance. By using the x and y position of each heavy ion entering the gas ionization detector, we should be able to correct the scattering angle for each reaction and improve the center-of-mass energy reconstruction. This is a topic for future work.

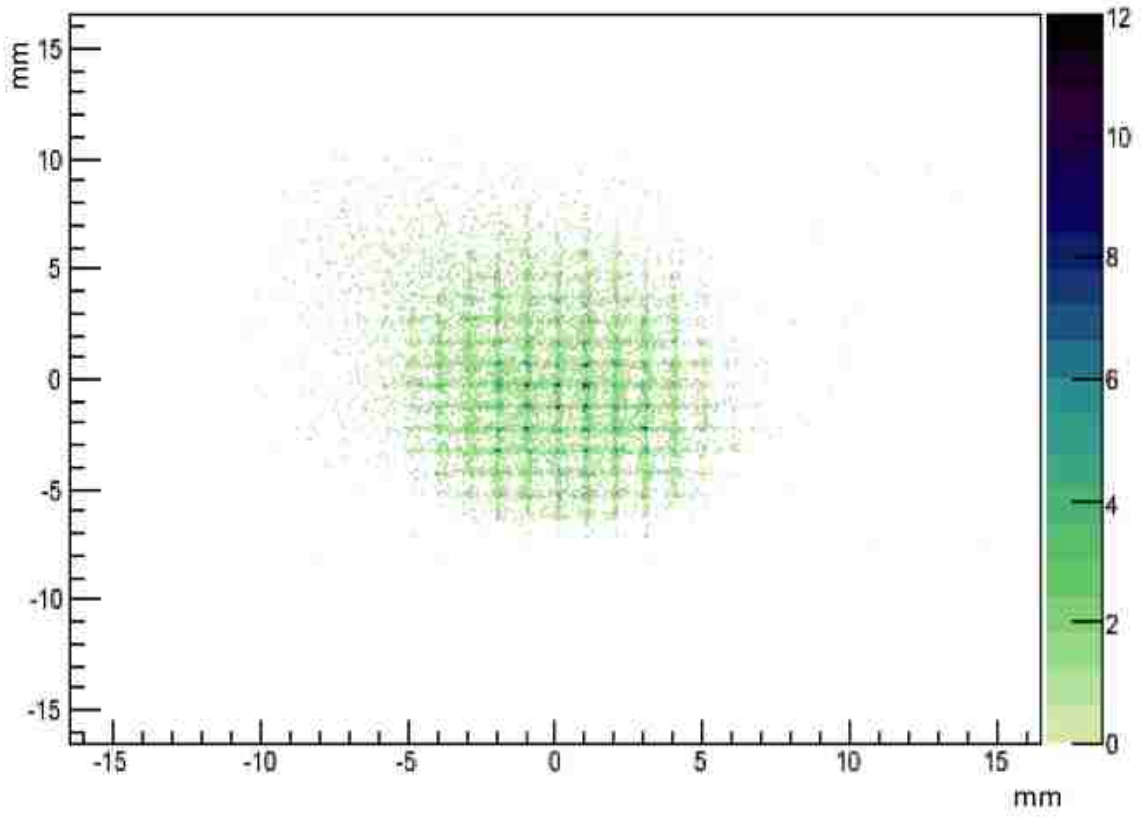

Figure 8.11. The position (y vs. x) of ^{25}Al ions in coincidence with protons. The scale is by wire number which are separated by 3mm.

CHAPTER 9. SUMMARY & FUTURE WORK

The structure of certain short-lived radioactive nuclei is important for understanding thermonuclear stellar explosions like novae and Type I X-ray bursts, influencing light curves and the synthesis of new isotopes. We studied nuclear structure of two important isotopes for thermonuclear stellar explosions, ^{26}Si and ^{32}Cl. States in ^{32}Cl determine the ^{31}S(p,γ)^{32}Cl reaction rate that provides the dominant break-out path from the SiP cycle in novae and is important for understanding enrichments of sulfur observed in some ejecta. The structure of ^{26}Si determines the ^{22}Mg(α,p)^{26}Si reaction rate that influences energy generation and nucleosynthesis in Type I X-ray bursts.

We precisely determined the excitation energies for a number of resonances in ^{32}Cl, including the two most important ones influencing the ^{31}S(p,γ)^{32}Cl reaction rate at nova temperatures. States were populated via the ^{10}B(^{24}Mg,2n)^{32}Cl reaction with a 75 MeV beam of ^{24}Mg bombarding a 200 μg/cm^2 ^{10}B target using the Argonne Tandem-Linac Accelerator System (ATLAS). Heavy ions were separated by the Argonne Fragment Mass Analyzer (FMA), and ^{32}Cl ions were identified by position in a Parallel-Grid Avalanche Counter and by relative energy loss in a gas ionization detector located at the FMA focal plane.

Gamma rays emitted from excited ^{32}Cl ions were detected using Gammasphere. We built the level scheme for ^{32}Cl using gamma-gamma coincidences with the 89.65 keV transition from the first-excited state to the ground state, and precisely determined energies for 6 states including levels at E_x = 1738.1 (6) and 2130.5(10) keV that correspond to the most important resonances in the ^{31}S(p,γ)^{32}Cl reaction at E_{cm} =156.3(7) and 549.9(8) keV. With these resonance energies established, the single uncertainty dominating the ^{31}S(p,γ)^{32}Cl reaction rate is the strength of the 549.9 keV resonance.

The relative size of the gamma and proton decay widths for the 549.9 keV resonance determne its strength. Previous gamma branching ratio measurements indicate $\Gamma_p \approx \Gamma_\gamma$ but with large uncertainties (Γ_p/Γ = 50(30)%) [Lef97]. However, the mirror to this state is weakly populated in the (d,p) reaction, with a single particle spectroscopic factor of about 0.002 [Eck89], indicating an expected proton partial width of $\Gamma_p \approx$ 0.9 meV, about 9 times smaller than the expected γ width. The proton branching ratio was directly measured by [Mat11b] to be Γ_p/Γ = (7 ± 4)%, in agreement with expectations from the mirror nucleus. A determination of the gamma and proton decay widths for the 549.9 keV resonance should be the target of further studies. We have developed a proposal to determine these branching ratios by studying the $^{32}S(^3He,t)^{32}Cl$ charge-exchange reaction using Gammasphere coupled with double-sided silicon strip detectors in the target chamber as have been successfully applied with GODDESS.

We studied the structure of ^{26}Si that is important for understanding the $^{22}Mg(\alpha,p)^{26}Si$ reaction rate through ^{25}Al+p elastic scattering. A secondary ^{25}Al radioactive ion beam at 102.5 MeV was produced by the inflight method at the John D. Fox Superconducting Accelerator Laboratory at Florida State University using the $^{24}Mg(d,n)^{25}Al$ reaction and the RESOLUT facility. The ^{25}Al beam bombarded a 2.05 mg/cm^2 polypropylene target. Scattered protons were detected and identified using a telescope of silicon strip detectors with a 0.5-mm-thick (ΔE) and 1.0-mm-thick E layer arrange to subtend laboratory angles of 9 to 22 degrees. Protons from scattering by ^{25}Al were cleanly distinguished from fusion evaporation and reactions induced by ^{24}Mg contaminating the beam by detecting heavy ions in coincidence in a position-sensitive gas ionization detector located downstream of the silicon array.

The center-of-mass energy for each event was reconstructed from the measured proton energy and angle, and the differential cross section for ^{25}Al+p scattering was determined from

center of mass energies of 2.7-4.0 MeV. We observe one strong s-wave resonance at an energy of about 2.8 MeV, below the alpha particle threshold in ^{26}Si. The energy of this resonance agrees well with a previously observed state in ^{25}Al+p elastic scattering, though the width and strength of the observed resonance is too large to be consistent to be the previous measurement. The lowest and highest energy protons we observe also show a broad distribution in energy, possibly indicating that the energy resolution in the measurement is compromised by as yet unresolved effects.

No strong resonances are conclusively observed $E_{cm} > 3$ MeV, though a relatively high density of resonances is anticipated, and some structures that are present may indicate the presence of resonances with proton spectroscopic factors less than 10^{-2}. We should at least be able to set an upper limit on proton spectroscopic factors for possible states at $E_x = 8.5$-9.3 MeV. Once the origin of the potential resolution issues in the data are resolved, a future measurement at higher bombarding energies would be compelling to cover the full range of energies that are important for the ^{22}Mg(α,p)^{25}Al reaction.

REFERENCES

[Bha08] M. Bhattacharya *et al.,* Phys. Rev. C **77**, 065503 (2008).

[Bea96] C. W. Beausang and J. Simpson, J. Phys. G: Nucl. Part. Phys. **22** (1996).

[Bla11] R. D. Blandford *et al*., "2020 VISION, An Overview of New Worlds, New Horizons in Astronomy and Astrophysics," The National Academies Press (2011).

[Blu08] Y. Blumenfeld *et al.,* Nucl.Instr.and Meth. B266 (2008), pp. 4074–4079.

[Che12] J. Chen *et al.*, Phys. Rev. C, 01/2012; 85(1):015805, DOI: 10.1103/PhysRevC.85.015805, accessed in January, 2016.

[Dav92] C. N. Davids *et al.*, Nucl.Instr.and Meth. B70 (1992).

[Dav01] B. Davin *et al.,* Nucl.Instr.and Meth. A473 (2001) 302-318.

[Dav05] C. N. Davids *et al.*, The Argonne Fragment Mass Analyzer, Recoil Mass Spectrometers in Heavy Ion Interactions Around the Coulomb Barrier, Volume 317 of the series Lecture Notes in Physics pp 313-319, 24 May 2005.

[Eck89] F. Eckle *et al.*, Nuclear Physics A 501, 413 (1989).

[Fab83] D. Fabris *et al.,* Nucl.Instr.and Meth. 216 (1983).

[Fae09] T. Faestermann *et al.,* Eur. Phys. J. A **42**, 339 (2009).

[FSU15] http://fsunuc.physics.fsu.edu/, accessed in January, 2016.

[Gas73] J. V. Gasteren *et al.*, Nuclear Physics A 210, 29 (1973).

[Geh98] R. Gehrz *et al.*, Nucleosynthesis in Classical Novae and Its Contribution to the Interstellar Medium , Publications of the Astronomical Society of the Pacific, Vol. 110, No. 743, January 1998, DOI: 10.1086/316107.

[Iyu10] A. Iyudin *et al.*, ISSN 1063-7729, Astronomy Reports, 2010, Vol. 54, No. 7, pp. 611–619. Pleiades Publishing, Ltd., 2010. DOI: 10.1134/S106377291007005X.

[Ili97] C. Iliadis *et al.,* Nucl. Phys. A 05 1997; 618(1-2):166-175. DOI: 10.1016/S0375-9474(97)00065-1.

[Ili10] C. Iliadis, R. Longland, A. Champagne, A. Coc, and R. Fitzgerald, Nuclear Physics A 841, 31 (2010), the 2010 Evaluation of Monte Carlo based Thermonuclear Reaction Rates.

[Jea89] C. Jeanperrin *et al.*, Nucl. Phys. A503, 77 (1989).

[Jos77] P. C. Joss, 1977, Nature, 270, 310.

[Jos05] J. Jose *et al.*, Nucl. Phys. A 04 2005; 752(1):540-549, DOI: 10.1016/j.nuclphysa.2005.02.058.

[Jos06] J. Jose *et al.*, Eur. Phys. J. A 27, s01, 107–115 (2006) DOI: 10.1140/epja/i2006-08-015-8.

[Kim05] K. Kimura *et al.*, Nucl. Inst. Meth. 538, 608 (2005).

[Lam78] D. Q. Lamb and F. K. Lamb, 1978, Ap. J., 220, 291.

[Lef97] A. Lefebvre *et al.*, Nucl. Phys. A **621**, 199 (1997).

[Lot 08] G. Lotay, P *et al.*, Phys. Rev. C 77, 042802 (2008).

[Mar77] L. Maraschi and A. Cavaliere, 1977, Highlights Astron., 4, 127.

[Mat93] T. Matheson *et al.*, Astrophys. J. 418, L29 (1993).

[Mat11a] A. Matic *et al.*, Phys. Rev. C, C **84**, 025801 (2011) DOI: 10.1103.

[Mat11b] M. Matos *et al.*, Phys. Rev. C 84, 055806 (2011).

[Mic14] Micron Semiconductor ltd, *Micron Catalogue Product Information for S2 DC Radial Detector*. March 1, 2014; http://www.micronsemiconductor.co.uk/pdf/s.pdf, accessed in January 2016.

[Nel85] R.O. Nelson, E. G. Bilpuch, and G. E. Mitchell, Nucl. Instrum. Methods Phys. Res., Sect. A **236** (1985) 128.

[Par08] A. Parikh *et al.*, The Astrophys. J. Suppl. Ser. 02 2008; 178(1). DOI: 10.1086/589879.

[Par14] A. Parikh et *et al.*, AIP Advances 4, 041002 (2014); http://dx.doi.org/10.1063/1.4863946, accessed in January 2016.

[Pep09] P.N. Peplowski *et al.*, Phys. Rev. C**79** (2009) 032801.

[Pra14] L. Pratt, Study of ^{18}Ne Using the Array for Nuclear Astrophysics and Structure with Exotic Nuclei, Ph.D. thesis, 2014.

[RAD96] http://radware.phy.ornl.gov/, accessed in January, 2016.

[Rae64] H. Raether, Electron avalanches and breakdown in gases, Butterworths, London, 1964.

[Rau00] T. Rauscher and F.-K. Thielemann, At. Data Nucl. Data Tables, **75**, 1 (2000).

[Rau01] T. Rauscher and F.-K. Thielemann, At. Data Nucl. Data Tables, **79**, 47 (2001).

[Roj11] A. Rojas, Experimental Study of the Proton Capture on ^{25}Al using ^{25}Al(d,n)^{26}Si reaction in inverse kinematics, Ph.D. thesis, 2011.

[Rui05] C. Ruiz *et al.,* Phys. Rev. C 71 025802 (2005), DOI: 10.1103/PhysRevC.71.025802.

[Sch99] H. Schatz *et al.*, ApJ 524, 1014 (1999).

[Sch01] H. Schatz *et al.*, NPA 688, 150 (2001).

[Sew07] D. Seweryniak *et al.,* Phys. Rev. C 75, 062801 (2007).

[Sew15] D. Seweryniak, private communication (2015).

[Smi90] A.E. Smith *et al.,* Nucl. Instr. and Meth. in Phys. Res. A289 (1990) 231-235.

[Ste81] J. Stelzer, Nucl.Phys.A354 (1981) 433.

[Vou94] S. Vouzoukas *et al.*, Phys. Rev. C **50**, 1185 (1994).

[War95] B. Warner, in Cataclysmic Variable Stars, Cambridge University Press, Cambridge, 1995.

[Wil94] R. E. Williams *et al.*, Astrophys. J. Suppl. Ser. 90, 297 (1994).

[Wir00] H.-F. Wirth *et al.,* Annual Report, Maier-Leibnitz- Laboratorium, 2000.

[Won98] S.S.M Wong, Nuclear Physics, Second Edition, Wiley & Sons, Toronto, Canada, 1998; p.162-163.

[Woo76] S. E. Woosley and R. E. Taam, 1976, Nature, 263, 101.

[Woo04] Woosley *et al.,* ApJS 151, 75 (2004).

[Wre10] C. Wrede *et al.,* Phys. Rev. C 82, 035805 (2010).

[Wre12] C. Wrede *et al.,* Phys. Rev. C 86, 047305 (2012).

[Wre14] C. Wrede *et al.*, AIP Advances 4, 041004 (2014), http://dx.doi.org/10.1063/1.4864193, accessed in January, 2016.

VITA

Liudmyla Afanasieva, a native of Ukraine, got her Bachelor of Science degree from Kharkiv National University in 2009. Afterwards she made the decision to enter graduate school in the Department of Physics and Astronomy at Louisiana State University. She received her Master's degree in May 2014 from Louisiana State University.